June 2017

High Performance Digitally Manufactured Microwave and Millimeter-Wave Circuits and Antennas

Eduardo A. Rojas
University of South Florida, eduardor@mail.usf.edu

High Performance Digitally Manufactured Microwave and Millimeter-Wave Circuits and Antennas

by

Eduardo A. Rojas-Nastrucci

A dissertation submitted in partial fulfillment
of the requirements for the degree of
Doctor of Philosophy in Electrical Engineering
Department of Electrical Engineering
College of Engineering
University of South Florida

Major Professor: Thomas M. Weller, Ph.D.
Kenneth Church, Ph.D.
Nathan Crane, Ph.D.
Gokhan Mumcu, Ph.D.
Arthur David Snider, Ph.D.
Jing Wang, Ph.D.

Date of Approval:
March 14, 2017

Keywords: Additive manufacturing, picosecond laser machining, mesh, modeling, 3D-printing

DEDICATION

To my wife, Melissa, and my two daughters, Sofia and Isabella.

To my parents, Esther and Ernesto, and my sister Valeria.

To my grandparents, Antonio and Maria.

ACKNOWLEDGMENTS

I feel fortunate to have had Prof. Thomas M. Weller as my Ph.D. advisor. I thank him for his guidance, patience, and kindness. I am always amazed by his level of expertise in the area of microwave circuits and antennas, his humbleness, work commitment and integrity. He is and will continue to be a role model for me. I would like to express my gratitude to Professors Larry Dunleavy, Gokhan Mumcu, and Jing Wang, for providing what I believe is a world-class education in my field of study. I also thank Dr. Kenneth Church, for his guidance and generous support. I had the privilege to work with Dr. A. David Snider, whom I thank for his valuable contributions.

This work is possible thanks to the immeasurable support of my wife, Melissa, who paused her dental practice to start our journey at USF. She is not only a wonderful and amazing wife but also a great dedicated mother. I also feel fortunate to have two wonderful daughters, Sofia and Isabella, who bring happiness to my life every day. I deeply acknowledge my parents, Esther and Ernesto, for raising and educating me and always working hard to provide a great home for me and my sister, Valeria, even under tough circumstances. I express my gratitude to my mentor, Prof. Wilfrido Moreno, and his family for their support and for treating us like family during our extended stay in Tampa. Special thanks to Carlos and Esther Callegari, for their kind and extensive support during my studies.

The Ph.D. voyage was enjoyable thanks in part to the great friends and colleagues in 412 and USF in general: M. Erazo, R. Ramirez, J. Castro, I. Nassar, A. Menon, D. Hawatmeh, R. Elzein, M. Grady, T. Palomo, A. Dey, S. Gupta, M. Abdin, E. Gonzalez, D. Lugo, A. Ross, A. Qaroot, D. Lan, A. Gheethan and J. Obrien. I would like to thank Dr. Paul Deffenbaugh for sharing his extensive knowledge in additive manufacturing; and Justin Nussbaum, for his countless hours of support for the manufacturing of BJ

metallic parts. At the Nanotechnology Research and Education Center, I am grateful to R. Tufts, J. Bieber, S. Louis-Jeune, and R. Everly, for their training, advice, and assistance.

I would like to give special thanks to two professors that initiated me in the area of electromagnetics and helped me with their excellent teaching and mentoring to succeed in my work: Prof. Paulino Delpino and Prof. Alfonso Zozaya. I also feel fortunate to have had great educators during my undergraduate studies, at the Universidad de Carabobo, among which are: D. Labarca, R. Albornoz, W. Sanz, D. Rey, T. Rybak, G. Arocha, C. Seijas, C. Villanueva, G. Morales, D. Nesbit, and A. Millan.

I will always be grateful to the University of South Florida and the Universidad de Carabobo for my professional education; the National Science Foundation for funding my research, and the Institute of Electrical and Electronics Engineers for being an excellent professional community. Sciperio, Modelithics, and nScrypt are three companies to which I also thank for their support.

TABLE OF CONTENTS

LIST OF TABLES

LIST OF FIGURES

ABSTRACT

The potential of Additive Manufacturing (AM) for microwave and mm-wave applications is increasingly being revealed thanks to recent advancements in research. AM empowers engineers with new capabilities to manufacture complex conformal geometries quicker and at lower costs. It allows, for instance, the embedding of RF front ends into functional structures. In this dissertation, two aspects of AM are explored: (a) The development and characterization of techniques that improve the performance of AM microwave circuits and antennas, and (b) study of complex geometries, such as meshed structures, as an alternative to reduce material usage, cost, and weight of the components.

Micro-dispensing of silver paste (CB028) is extensively used in this work as a viable approach for manufacturing microwave planar transmission lines. However, the performance and upper-frequency range of these lines are limited by the cross-sectional shape and electrical conductivity of the printed paste, as well as the achievable minimum feature size which is typically around 100 μm. In this work a picosecond Nd:YAG laser is used to machine slots in a 20-25 μm-thick layer of silver paste (Dupont CB028) that is micro-dispensed on a Rogers RT5870 substrate, producing coplanar waveguide transmission lines with 16-20 μm-wide slots. It is shown that the laser solidifies 2 μm wide region along the edges of the slots, thus significantly increasing the effective conductivity of the film and improving the attenuation constant of the lines. The extracted attenuation constant at 20 GHz for laser machined CB028 is 0.74 dB/cm. CPW resonators and filters show that the effective conductivity is in the range from 10 MS/m to 30 MS/m, which represents a 100x improvement when compared to the values obtained with the exclusive use of micro-dispensing.

Another main aspect of this dissertation is the study of meshed structures in coplanar waveguides. For most AM processes the materials utilized for the conductive layer are the most

expensive ones; hence, there is value in minimizing the conductor surface area used in a circuit. In this work, the approach of meshed ground coplanar waveguide (MGCPW) is analyzed by simulating, fabricating and measuring a broad set of meshed ground geometry sizes. Furthermore, a physical-mathematical model is presented, which predicts the characteristic impedance and the capacitance per unit length of MGCPW with less than 5.4% error compared to simulated data. A set of filters is designed and fabricated in order to demonstrate the approach. The main parameter affected by meshing the ground plane is the attenuation constant of the waveguide. It is shown that 50% mesh density in the ground plane of a MGCPW line can be used with less than 25% increase in the loss. In contrast, the loss of finite ground coplanar waveguide (FGCPW) can increase by as much as 108% when the ground size is reduced by the same factor (50%). Both 3D printing (micro-dispensing) and traditional printed circuit board manufacturing are used in this work, and most of the propagation characterization is performed at 4 GHz.

A meshing technique is also applied to rectangular waveguides, and its effects are studied. It is presented as an option for high power, low loss, but also reduced weight applications. A set of meshed Ku-band waveguides was fabricated using binder jetting 3D printing technology showing that the weight can be reduced by 22% with an increase in loss of only 5%, from 0.019 dB/cm for the solid part to 0.020 dB/cm average across the band with the meshed design. Further weight reduction is possible if higher loss is allowed. To demonstrate the concept, a comparison is made between non-meshed and meshed waveguide 4 pole Chebyshev filters.

Finally, the BJ technology is characterized for Ku-Band rectangular waveguide and reflector antenna applications. This technology is characterized using electron beam microscopy (SEM) and energy dispersive spectroscopy (EDS). The RF performance of the 3D printed circuits is benchmarked with Ka-band cavity resonators, waveguide sections, and a filter. An unloaded resonator Q of 616 is achieved, and the average attenuation of the WR-28 waveguide section is 4.3 dB/m. The BJ technology is tested with a

meshed parabolic reflector antenna, where the illuminating horn, waveguide feed, and a filter are printed in a single piece. The antenna shows a peak gain of 24.56 dBi at 35 GHz.

CHAPTER 1: INTRODUCTION

1.1. Motivation

Two of the most well-known design paradigms in traditional manufacturing are: a) Complex designs generally lead to higher fabrication costs. b) The cost of production decreases with increasing number of units fabricated. These two facts are the main reasons why, in the design stage, engineers are typically constrained to simpler designs approaches with the purpose of achieving lower costs. Moreover, during the prototyping stages, the fabrication costs (per unit) are considerably higher when compared to the ones of a large volume of products; hence, the least number of design iterations is encouraged. Figure 1-1 illustrate the common trends of manufacturing cost per unit as a function of the complexity of a device, and as a function of the number of units fabricated [1, 2]. Contrastingly, the costs of parts made using Additive Manufacturing (AM) are usually independent of design complexity and of the production volume (as depicted in Figure 1-1). Therefore, AM makes economically feasible the fabrication of complex geometries that offer an advantage in performance or another aspect such as weight. It also allows the designer to fabricate more prototypes in a quick manner, ultimately leading to a better final product.

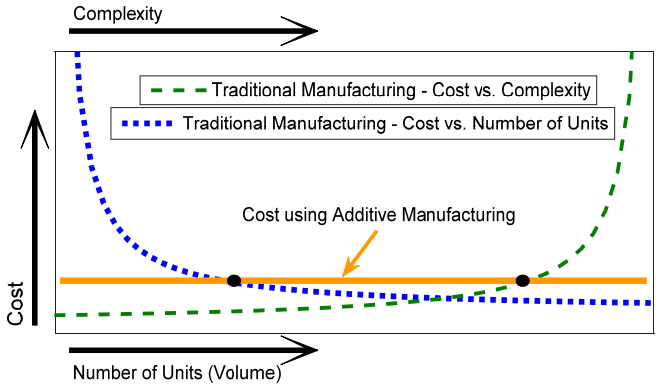

Figure 1-1: Manufacturing cost as function of design complexity and number of units. Partially adopted from [3] and [1].

Additive manufacturing (AM) is continuously gaining terrain over traditional manufacturing techniques, as its cost keeps being reduced and the design advantages are understood. For instance, one of the first mass-produced additively manufactured parts, a fuel nozzle, will be soon used in the next generation of GE jet engines [4]. According to [5] the compound annual growth rate of the 3D printing industry was 66% from 2013 to 2014, and similar growth rate is expected for several years. Furthermore, AM is supposed to become, on average, 50% less expensive, and 400% faster from 2013 to 2018 [6]. One key advantage of AM is the possibility of realizing complex geometries with a manufacturing process that generates low material waste. Specifically, for microwave circuits, a fabrication process that traditionally may require more than six steps (film deposition, exposure, etching, and so forth) is reduced to two basic steps in 3D printing: print and cure.

One of the major barriers to the implementation of AM in the area of microwave and mm-wave circuits and antennas is the typical poor performance of the components, resulting from dissipative losses. This problem represents an excellent opportunity to improve the capabilities of the different 3D printing technologies. For instance, in recent years, engineered 3D printable composites have been developed [7-12], achieving loss tangents that are better than the ones obtained from traditionally manufactured state of the art substrates. Based on the facts that the overall cost of AM technologies is decreasing, that the performance of the components is improving, and that AM enables the fabrication of complex geometries without an increase in cost, it is expected that 3D printing will continue displacing conventional subtractive manufacturing methods such as photolithography and milling in the future.

1.2. Contributions

The contributions of the present work are summarized in the following points:

a) Development and characterization of a picosecond laser machining technique for thick-film conductive paste, for the manufacturing of coplanar waveguide (CPW) circuits up to 40 GHz. This technology achieves losses on CPW lines of 0.74 dB/cm at 20 GHz, which is comparable

to the ones obtained from state of the art traditionally manufactured transmission lines. This loss improvement translates to an improvement of around 100x in the effective high-frequency electrical conductivity of the metallization layer when compared to state of the art micro-dispensed technologies found in the literature.

b) Development of a closed form analytical method for computation of loss in laterally non-uniform metallization layers. This method predicts with high accuracy the resultant loss obtained from the laser machined CPW described in point (a), using conformal mapping.

c) Study of meshed ground CPW (MGCPW), with the aim of reducing the conductor usage in the fabrication of the transmission lines.

d) Development of a physical-mathematical model to predict the transmission line parameters such as capacitance per unit length and characteristic impedance, in MGCPW. This method predicts the parameters of the MGCPW lines presented in this work with less than 5.4% error, and it is based on the conformal mapping method.

e) Study of the microstructure of the layers of the CB028 conductive paste using image processing of SEM micrographs. This study provided a deeper understanding of the inhomogeneity of the silver paste layer and helped to understand the loss mechanisms of the micro-dispensed RF circuits. This image processing method is also useful to quantify the effects of the laser machining method described in point (a).

f) Study of meshed rectangular waveguides as a technique to reduce weight in high-power applications. The study is performed at the Ku-Band, and the waveguides were manufactured using binder jetting (BJ) metal printing. This characterization provides an understanding of the effects that meshing the walls of a rectangular waveguide has on the propagation characteristics.

g) Characterization of the binder jetting (BJ) metal 3D printing technology for Ka-band rectangular waveguide applications and antennas. The study presented in this work provides the designer with an understanding of the loss of the structures, dimensional accuracies, and the fabrication process. A demonstration of a monolithic approach for integrating a filter within the feed waveguide structure is also presented.

1.3. Dissertation Outline

This dissertation is comprised of seven chapters, including the current chapter which is focused on the introduction of the work. The content of the rest of the chapters are as follows:

a) Chapter 2 includes a literature review where the main AM technologies used for microwave and mm-wave circuits and antennas are discussed. Fabrication of multilayer planar RF circuits and solid metal 3D printed devices are among the covered topics. The chapter offers an overview of the state of the art of the technologies that pertain to this dissertation.

b) Chapter 3 described the development and characterization of the technique of picosecond laser machining of 3D printed conductive traces. A mathematical closed-form model that predicts the loss of the laser machined structure is included in the same chapter.

c) Chapter 4 describes the study of meshed ground coplanar waveguides (MGCPW) with the aim of reduction of printing cost and time. A detailed analysis of the effect of meshing the grounds on the propagations characteristics is performed. Also, a physical-mathematical model to predict the capacitance per unit length and the characteristic impedance is included.

d) Chapter 5 describes the characterization of binder jetting (BJ) metal 3D printing for Ka-band circuits and antennas. The study is performed using cavity resonators, rectangular waveguides, filters, and a parabolic dish reflector antenna.

e) Chapter 6 is focused on the study of the meshed rectangular waveguide geometry as an alternative to realize high-power and low-loss circuits with reduced weight. The characterization is performed in the Ku-band, using waveguide sections and filters.

f) Chapter 7 summarizes the dissertation and includes the recommendations for future work.

CHAPTER 2: BACKGROUND AND LITERATURE REVIEW

2.1. Introduction

Since its initial development in the decade of 1980s, many different AM technologies that leverage various physical mechanisms have arisen. In the particular field of microwave circuits and antennas, AM has gained increasing attention in the last ten years mainly due to its capability of realizing complex geometries. Lack of good performance has been one of the major roadblocks for the implementation of AM in commercial products; but today, thanks to research advancements in the different techniques, the performance of 3D printed devices is reaching levels comparable to the ones obtained with traditional manufacturing in some cases. In this chapter, the most of the known 3D printing techniques used for high-frequency circuits and antennas are discussed, presenting examples of AM devices that are found in the literature. Also, works where meshed structures are employed in waveguides are presented.

2.2. Planar RF and Millimeter-Wave Circuits and Antennas

The technologies utilized for the fabrication of multilayer microwave filters found in the literature are: inkjet printing [13-15, 16], aerosol jet printing (AJP) [17-19], ultrasonic wire embedding [20, 21], fused deposition modeling (FDM) combined with direct print additive manufacturing (DPAM) [22-33], and polymer multichip module process (MCM-P) [34]. These technologies offer significant capability with complementary advantages. The inkjet printing and AJP technologies tend to yield relatively thin, but highly conductive traces with fine feature sizes; which are the order of tens of micrometers [15, 17]. Figure 2-1(a) shows a picture of a 1.5 turns multilayer spiral inductor fabricated with inkjet printing, where and inductance of 7 nH and a Q factor of 11 are achieved at around 2 GHz [15]. In that work, the

drop spacing is set to 20 μm, and the layer thickness is about 4-5 μm. On the other hand, Figure 2-2 shows a multilayer stripline structure fabricated using AJP. This stripline offers low loss, of 0.6 dB/mm at 40 GHz, with manufacturing resolution of 10 μm, and a minimal stack accuracy of 0.7 μm/layer [17].

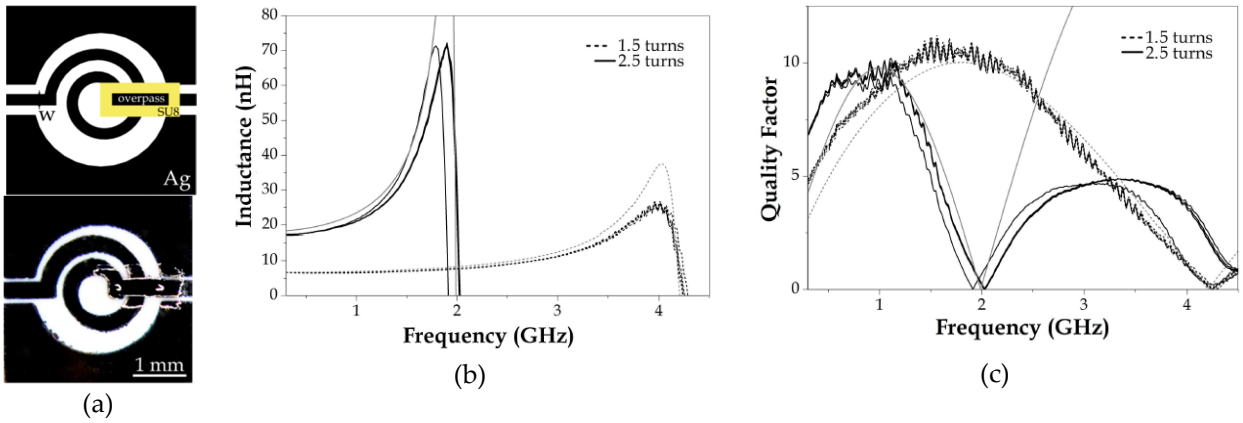

(a) (b) (c)

Figure 2-1: (a) Picture, (b) measured inductance vs. frequency, and (c) extracted Q factor of a spiral inductor fabricated with AJP [15].

In contrast, DPAM (also known as micro-dispending) is useful for a much wider range of material viscosities, yields thicker conductors and can be used with lower temperature materials. However, there are critical challenges that limit the ultimate performance and feature size of micro-dispensed conductors when using commercially available pastes, such as the Dupont CB028 silver flake thick-film paste utilized in this work. The DC conductivity of CB028 is only ~2 MS/m, and the effective RF conductivity can be more than ten times lower due to a combination of uneven silver flake distribution [27] and the tapered nature of the as-printed edges where current densities are high. Another limitation of micro-dispensing that restricts the upper-frequency range of printed thick-film circuits is the minimum achievable slot size, which is typically greater than 100 μm when using non-polished surfaces such as commercial microwave laminates and 3D-printed substrates [35]. A picture of a suspended microstrip line fabricated with DPAM and stereolithography (SLA) is presented in Figure 2-3(a) [28, 36]. The attenuation constant of this suspended transmission line is around 0.026 dB/mm at 8 GHz [36]; which is close to the loss of the stripline structure fabricated using also DPAM (at 8 GHz), shown in Figure 2-3(b).

The multilayer capability of the DPAM technology was used to fabricate a 2.45 GHz phased array antenna unit presented in Figure 2-3(c) [27].

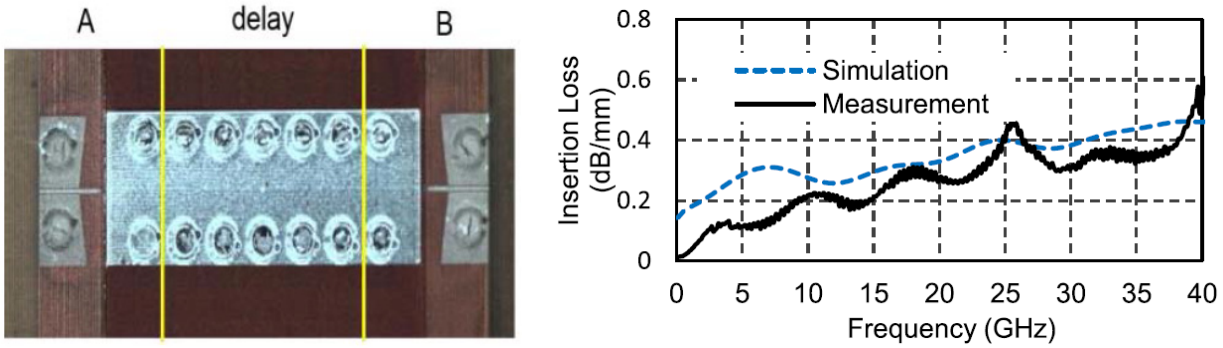

(a) (b)

Figure 2-2: Stripline fabricated with AJP. (a) Picture. (b) Extracted insertion loss [17] © 2016 IEEE.

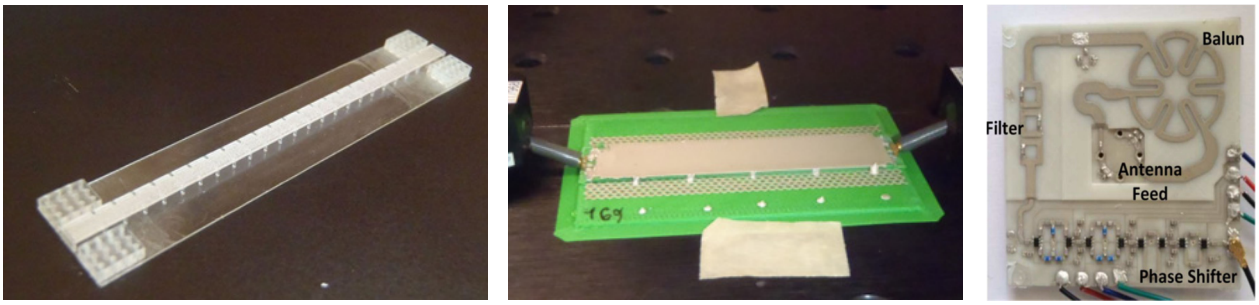

(a) (b) (c)

Figure 2-3: (a) Suspended microstrip line using SLA and micro-dispensing [28] © 2015 IEEE. (b) Multilayer stripline [36] and (b) phased array antenna unit using DPAM system [27] © 2015 IEEE.

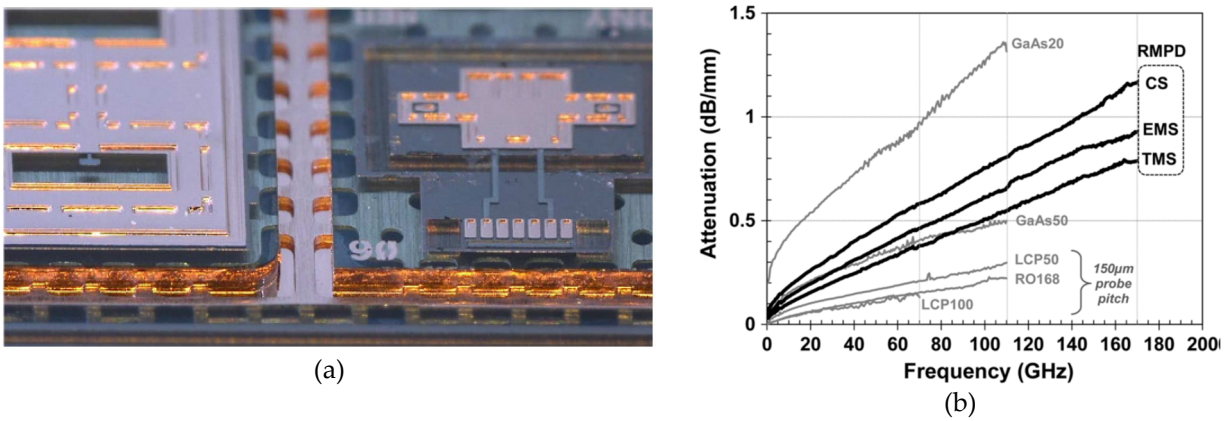

(a) (b)

Figure 2-4: MCM-P: (a)Picture of AM module. (b) Attenuation of AM transmission lines (CS, EMS, and TMS) compared to other technologies [34] © 2015 IEEE.

The MCM-P technology also offers multi-layer capability. The achieved resolution of these parts are 8 μm and 15 μm, for gaps and linewidths, respectively, over a 2-3 μm metallization layer [34]. Figure 2-4(a) shows an MCM-P structure, and Figure 2-4(b) includes the comparison of the losses obtained with this technology, and they are compared to the ones achieved with state of the art traditional manufacturing methods, such as using GaAs, LCP, and RO168 substrates.

2.3. Meshed Conductors in Planar Waveguides

While meshed structures have primarily been utilized as flexible and lightweight reflecting surfaces [37, 38], their use in transmission line structures has also been studied. Meshed ground planes for microstrip circuits are examined in [39, 40]. The concept of meshed ground CPW (MGCPW) is introduced in [31] as an option for 3D printed circuits. Moreover, MGCPW has been demonstrated to improve the power handling on high-current CMOS circuits, up to 50 GHz [41]. In AM, the utility of the meshed ground planes is not only related to a reduction in material usage and printing time, but also it offers advantages in structural integrity. The openings in the conductor will improve the adhesion of substrate/superstrate layers in multi-layer circuits; this specific issue of layer adhesion proves to be critical in both High and Low-Temperature Co-fired Ceramics circuits (HTCC and LTCC), and the coupling between meshed ground microstrip lines has been studied [42].

2.4. 3D Printing for Medium to High Power Waveguides and Antennas

In the area of medium to high power waveguides, such as air-filled rectangular waveguides, different AM technologies are available. Among those technologies are copper plated plastics [43-50], selective laser melting (SLM) of metal powders [51-57], binder jetting [58], electron beam melting (EMB) [59], and 3D copper additive manufacturing (3D-CAM) [60, 61].

The realization of low weight medium power devices such as the filter shown in Figure 2-5(a) is possible thanks to the versatility of AM; it is an X-band filter fabricated using copper plating of SLA. Its center frequency is 10 GHz with 3% fractional bandwidth and 0.25 dB average insertion loss [62], and it is

85% lighter than its counterpart made out of solid copper. For higher power applications, SLM of metals offers a solution with similar loss levels to the plated plastic parts, but with better thermal conductivity. The filter shown in Figure 2-5(b) (SLM) has an insertion loss of 0.1 dB in the band of 12.5-15 GHz [52]. Note that SLA parts show better dimensional accuracy than the SLM technology, achieving frequency offsets lower than 0.01% (SLA) versus the 2% achievable with SLM [62]. Another AM technology that offers exceptional low losses at mm-wave frequencies is 3D copper additive manufacturing (3D-CAM). Figure 2-5(c) shows a picture of a 16-way combiner of dimensions 12 mm x 13 mm x 23 mm that operates in the frequency range of 220-240 GHz [61]. Note that in the 3D-CAM technology, the geometry is constructed by stacking additively manufactured slices of copper.

Naturally, the technologies previously described can also be used to fabricate antennas. A picture of a Ka-Band pyramidal horn antenna fabricated with BJ is shown in Figure 2-6(a). This antenna shows 20 dB return loss over the entire band (26-40 GHz) and 8.43 dBi gain at 26.5 GHz. [58]. A non-conventional design, a volcano smoke antenna, is presented in [63]. It has a 10 dB return loss in the frequency range of 3.2-12.6 GHz and a gain -0.5 dBi at 6.85 GHz. Moreover, SLM printed antennas show excellent performance at mm-wave frequencies. As an example, the conical antennas in Figure 2-6(b) show gains greater than 21.5 dBi for the E-(60–90 GHz), D- (110–170 GHz), and H-band (220–325 GHz) [55]. Alternatively, fabrication of ceramic antennas is also possible using AM. For instance, it has been shown that Ceramic SLA (C-SLA) can be used to fabricate a Luneberg lens, with 85% radiation efficiency, 10 dB return loss in the frequency range of 28-38 GHz, and 24 dBi gain at 28 GHz (Figure 2-6(d)) [64]. It is important to mention that most of the geometries shown in Figure 2-5 and Figure 2-6 are either impossible to manufacture in one piece or it cost would make them impractical when fabricated using traditional methods such as machining.

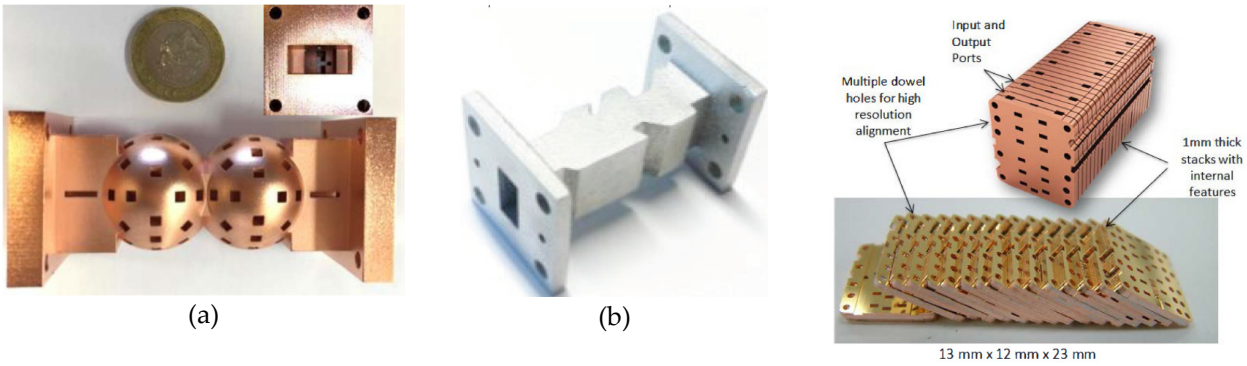

(a) (b) (c)

Figure 2-5: AM filters and waveguides: (a) X-Band filter using copper plating of an SLA part [62] © 2016 IEEE. (b) Ku-Band filter fabricated using SLM [52] © 2016 IEEE. (c) WR4 220-240 GHz 16-way combiner using 3D-CAM [61] © 2015 IEEE.

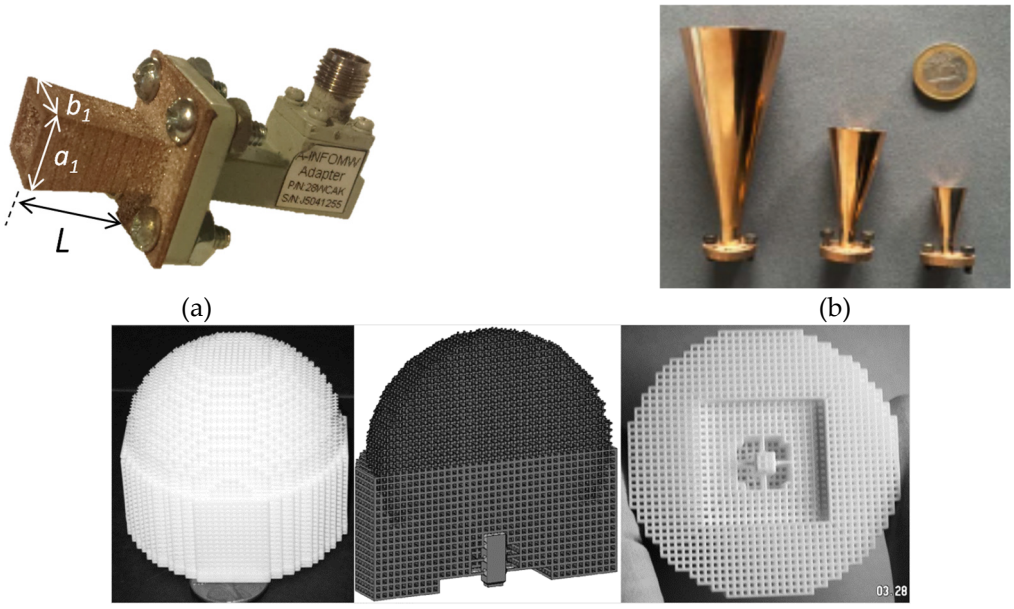

(a) (b)

(c)

Figure 2-6: AM antennas: (a) Ka-Band pyramidal horn using BJ [58] © 2016 IEEE. (b) mm-wave SLM conical horn antennas [55] © 2016 IEEE. (c) C-SLA Ka-Band Luneberg lens [64] © 2007 IEEE.

CHAPTER 3: LOW LOSS COPLANAR WAVEGUIDE CIRCUITS USING PICOSECOND LASER MACHINING OF MICRO-DISPENSED CONDUCTOR

3.1. Introduction

Two of the most common limitations of additively manufactured waveguides are: (a) the dissipative losses, which tend to be higher than the ones obtained from devices fabricated with traditional methods, and (b) the minimum feature sizes, which ultimately defines the upper operational frequency limit. For example, the minimum achievable slot size using micro-dispensing is typically around 100 μm, limiting the operation frequency of coplanar waveguides (CPW) to below 10 GHz. This chapter is focused on the development of a technique that addresses these problems.

In this work, the minimum feature size issue is addressed by using a Nd:YAG laser (Lumera Laser's SUPER RAPID-HE Picosecond laser) integrated with an nScrypt 3D printer to machine narrow slots into a layer of micro-dispensed CB028. Due to the emission of very short pulses, the conductor is exposed to sudden high energy irradiation in the infrared wavelength range (1064 nm), producing a cold ablation. This process completely decomposes thin layers of material at a controllable removal rate. Laser machining has previously been used for rapid prototyping of microwave components made with low temperature co-fired ceramic (LTCC) technologies, achieving 50 μm and 65 μm wide slots in [65] and [66], respectively. Furthermore, due to the excellent finishing and small features that the Nd:YAG laser can provide, it has been used to build a 24 GHz radar front-end [67]. In [68] an Ag-coated Cu paste (DuPont

---

The content of this chapter has been published in [27] and [83], and it is included in this dissertation with permission from the IEEE. A copy of the permission is included in the Appendix A.

CB230) is deposited on top of fiberglass dome and then machined with a Nd:YVO4 laser to fabricate a GPS antenna.

The fabrication, mm-wave characterization and analysis of micro-dispensed and laser-machined CPW lines on Rogers RT5870 substrates are presented in this chapter. This is considered a low-temperature process as the printing bed is held to a maximum of 90ºC. The K-band performance of the laser machined CPW lines with slots size down to 16 μm is further characterized by the use of resonators and a filter, showing extracted effective electrical conductivities in the range of 10-30 MS/m. These conductivity values represent an improvement on the order of ~100x when compared to the ones obtained with the exclusive use of micro-dispensing. SEM micrographs show that solidification of the silver flakes occurs near the edges of the slots, which contributes to the conductor loss reduction. Image processing of these micrographs is used to quantify the width of the solidification. The loss of the structure is modeled using a conformal mapping method that accounts for non-uniform conductivity in the conductors, showing good agreement with simulated data, and explaining the performance improvement due to the silver solidification. It is demonstrated that a hybrid approach of additive manufacturing and laser machining enables the fabrication of higher frequency circuits (up to 40 GHz) with improved performance, with conductive ink that is selectively printed where it is needed on the substrate as opposed to etching vast areas of a totally metallized substrate. It also enables faster fabrication times in a single-machine process. Experimental data suggests that loss reduction due to the laser machining processing is greater for smaller slot sizes and higher frequency, a finding that is also predicted by the analytical calculations using conformal mapping.

3.2. Properties of Micro-Dispensed Silver Paste

To study the structure of the CB028 conductive layer, squared samples of these paste, with different thicknesses, are printed on glass substrates and then cured. These samples are then mounted in epoxy resin and sliced to expose the cross section of the silver layer. A Scanning Electron Microscope

(Hitachi SU-70) is utilized to obtain micrographs of these cross-sectional views. These SEM images are processed to extract the characteristics of the structure. The first step in this image processing is to adjust the contrast of the pictures based on their intensity histogram, making sure that the information covered the entire pixel range. Figure 3-1(a) shows the image with the adjusted contrast of 25.19 μm thick sample. The second step is to identify the pixel intensity range corresponding to silver ink flakes. Finally, the SEM micrographs are converted to a binary matrix (as shown in Figure 3-1(b). With this matrix, it is possible to compute the silver flake density across the conductive sample. In this case, the density is calculated for each successive layers of two micrometers each, calculating the area occupied by silver flakes. The results, shown in Figure 3-2, indicate that the conductive layer is not homogeneous. Furthermore, this data is showing particle settling, where the density decreases as a function of height. Also, thicker samples (40 μm – 50 μm) show lower density for the top layer, when compared with thinner samples (20 μm – 40 μm).

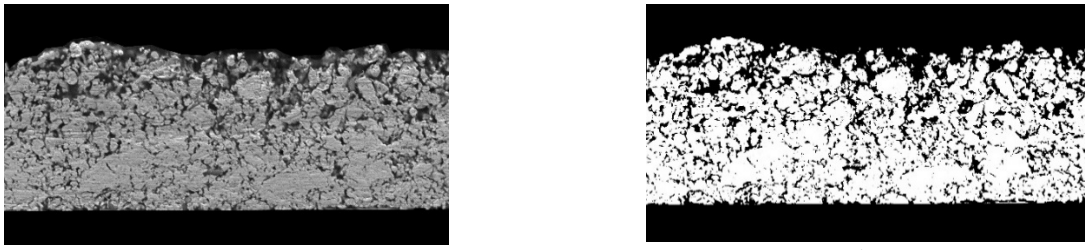

(a) (b)

Figure 3-1: (a) SEM micrographs of micro-dispensed CB028. (b) Binary image used to compute the silver flake density.

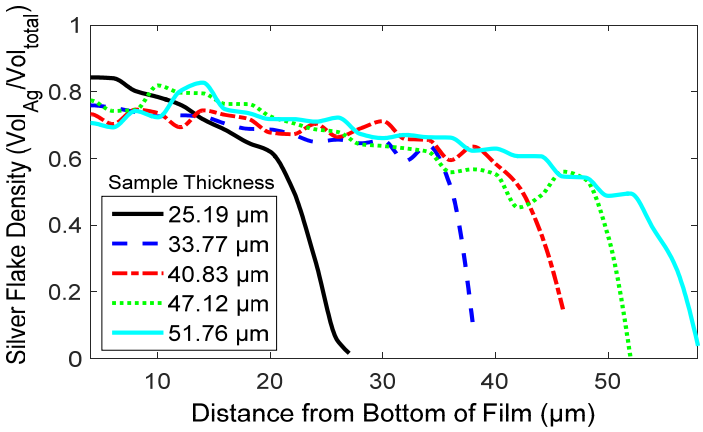

Figure 3-2: Computed silver flake density on micro-dispensed CB028.

3.3. Fabrication and Characterization

3.3.1. Fabrication

The fabrication process begins by microdispensing a layer of Dupont CB028 silver paste onto a 0.38 mm-thick (h) Rogers RT5870 substrate using an nScrypt 3Dn tabletop printer. The following printer settings are used: 125 μm dispensing tip inner diameter, 14 psi air pressure, 20 mm/s head speed, and 0.11 mm valve opening. The printing mechanism is described in [69]. After printing, the ink is dried for 1 h at 90°C. The measured roughness (R_a) of the silver paste layer is 1.2 μm. The Lumera SUPER RAPID-HE Picosecond laser is used to machine a slot in the CB028 layer. A 5x lens produces a spot size of 16 μm. To achieve wider slots (e.g. the 50 μm wide slots in this work), a sweep of the 16 μm diameter laser beam is performed, where consecutive cuts are shifted by 10 μm until the desired cut is achieved. The wavelength of the laser is 1064 nm. The optimal removal rate for a complete cut of the layer is found with the following settings: peak power of 4 MW at a repetition rate 100 kHz, and six repeated passes over the same area. Since the duration of the pulse is only 5 ps to 15 ps, a clean and accurate ablation is achieved, as the material undergoes a transition from the solid to the vapor phase without an appreciable melting phase. Nevertheless, a small amount of residual heat spreads over the periphery of the material that can melt and then solidify the edges [70]. The laser pulses will create a plasma at the point of ablation, and the light will disappear rapidly, but the residual heat will take more time to thermally dissipate and this leaves a thin melt zone. This melt zone is located on the edges of the ablation pattern.

3.3.2. Propagation Characteristic

To directly compare the performance of the laser machined slots with the slots obtained directly from micro-dispensing, a set of transmission lines are fabricated with both methods and similar dimensions. Due to the limits of the micro-dispensing technology, the slot size (s) is chosen to be 53 μm in this case. The general dimensions (as defined in Figure 3-3) are set to w = 1.2 mm, and g = 3.6 mm and the length l = 5 mm. Figure 3-4 shows SEM micrographs of the obtained slots. It is observed that the micro-

dispensing technique generates tapered edges, which show considerable edge roughness and are main contributing factors to conductor loss. In contrast, the laser machined slot shows well-defined edges with greatly improved edge roughness.

The characterization in this work is based on S-parameters, which were measured using GGB 40A 650 μm pitch probes calibrated with a CS-10 Picoprobe calibration substrate (SOLT calibration), and a Keysight PNA N5227A (Figure 3-5). A Cuming Microwave C-Ram GDSS-030 absorber is placed under the substrate to prevent coupling between the transmission lines and the metallic chuck of the probe station. The propagation constant is extracted using the method described in [71], and it is denoted as $\gamma=\alpha+j\beta$, where α is the attenuation constant, and β is the phase constant.

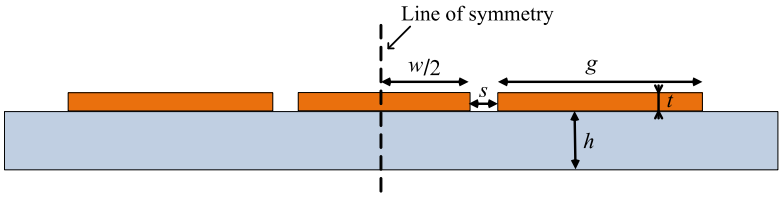

Figure 3-3: CPW geometry.

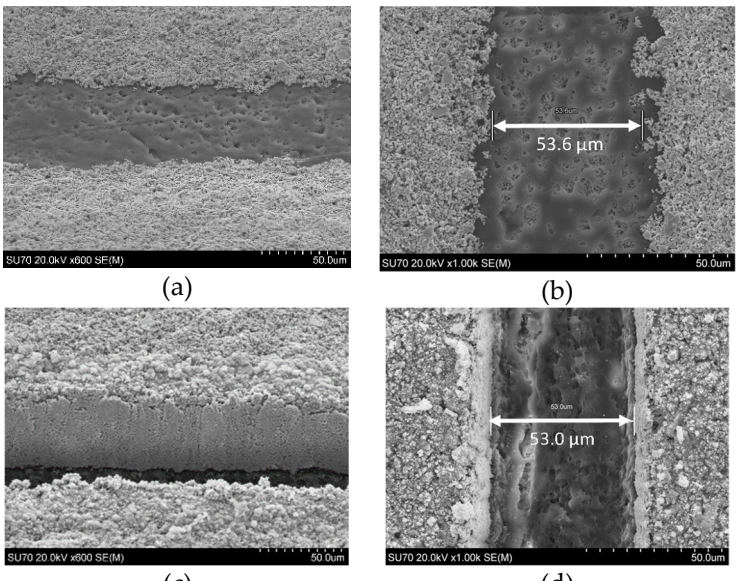

Figure 3-4: SEM micrographs of CPW slots. (a) and (b) are lateral and top view of printed slots, respectively. (c) and (d) are lateral, and top view of laser machined slots.

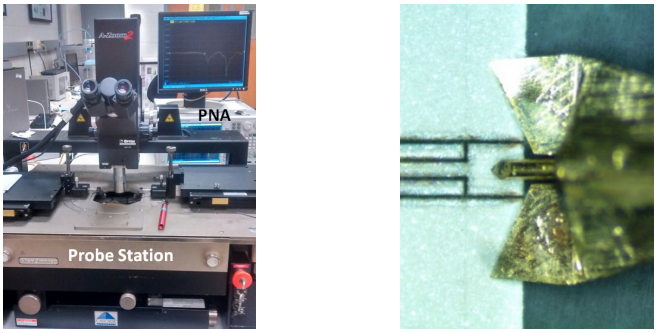

(a) (b)

Figure 3-5: Measurement setup: (a) Measurement equipment. (b) RF probe while testing one of the filters of this work.

The relatively large size of the micro-dispensed slot and the resulting total line width limit the maximum frequency of operation of the CPW lines to less than 23 GHz, which based on simulations is the frequency at which the coupled slotline mode starts to propagate. This mode shows a cutoff frequency [72, 73] that is typically lower than that of the higher order modes [74]. The measured propagation constants of the transmission lines made with both methods are shown in Figure 3-6. It is observed that on average the loss is reduced by 30% for laser machined CPW samples when compared with the 3D-printed lines. Effective conductivities are extracted by matching the measured data with simulations performed with Ansys Electronic Desktop 2016.2 software; the values are 0.1 MS/m and 0.45 MS/m, for the 3D-printed and laser machined lines, respectively. The measured line impedances are 40 Ω and 45 Ω, for the laser machined, and 3D printed lines, respectively.

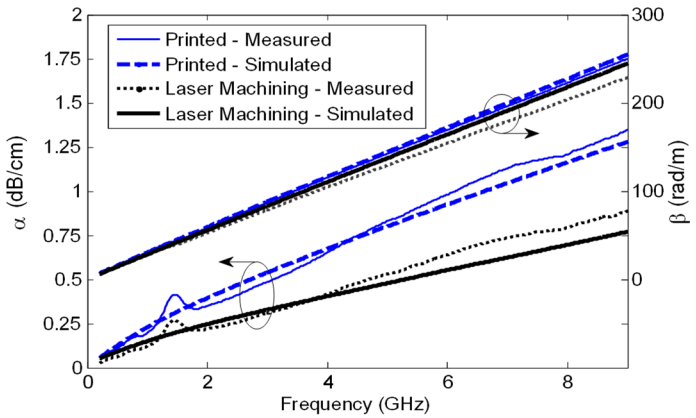

Figure 3-6: Propagation constant of CPW with s = 53 μm.

3.3.3. K-Band Performance

A second set of CPW transmission lines are fabricated in order to characterize the K-band properties of the laser machined slots. The dimensions are: w = 0.3 mm, s = 20 μm, t = 25 μm, g = 1.5 mm, d = 0.38 mm, and the length is 1.5 mm. The substrate is the same Rogers RT5870 used for the lower frequency transmission lines. A solid rectangular area of size (w+2g+2s)×1.5 mm is printed using micro-dispensing, dried, and subsequently, laser machined to create the CPW slots. The silver ink layers are in the range of 20-30 μm thick (t), achieving an aspect ratio greater than one. SEM micrographs of the cross-section of the laser machined slots are shown in Figure 3-7(a), and it is contrasted to the cross-section of a typical micro-dispensed paste edge (Figure 3-7(b)). The slot size used here approaches the smallest feature achieved to date with the described laser machining process (16 μm) and shifts the simulated onset of coupled slotline modes in 50 Ω CPW on the RT5870 substrate to around 40 GHz.

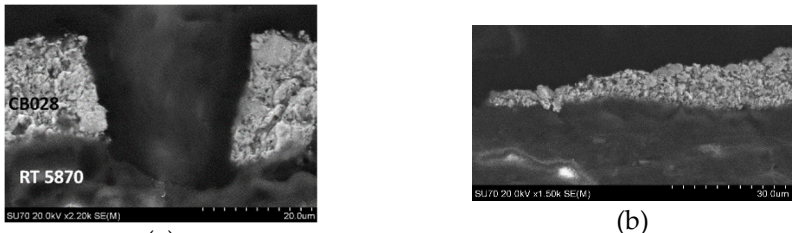

(a) (b)

Figure 3-7: SEM micrographs of cross-sectioned CPW slots. (a) 20 micron-wide laser machined slot. (b) Edge of micro-dispensed line.

The measured performance (Figure 3-8) shows an extracted effective electrical conductivity of 10 MS/m at 20 GHz. This value is around 100x larger than the values extracted for the micro-dispensed lines (with s = 53 μm) at 9 GHz. It also represents an improvement of about 10x when compared to the lower loss of 3D printed lines reported in [28] at 10 GHz, further indicating that the laser machining is changing the properties of the silver paste edges, and the conductor itself. To validate the performance improvement, a set of series stub resonators are fabricated. The dimensions are depicted in Figure 3-9(a), where s = 16 μm, w = 0.3 mm, L_r = 6.24 mm, and g = 1.65 mm. Figure 3-9(b) shows a SEM micrograph of a fabricated resonator, where the coupling gap can be appreciated, and artifacts caused by a small

overshoot of the laser path are indicated. The resonators show an average unloaded Q factor (Q_u) of 18.5, a resonance frequency of 18.35 GHz, and a transmission scattering parameter (S_{21}) of -21.8 dB. The behavior of Q_u is simulated and plotted in Figure 3-10, showing an extracted effective conductivity (σ) of 32.27 MS/m.

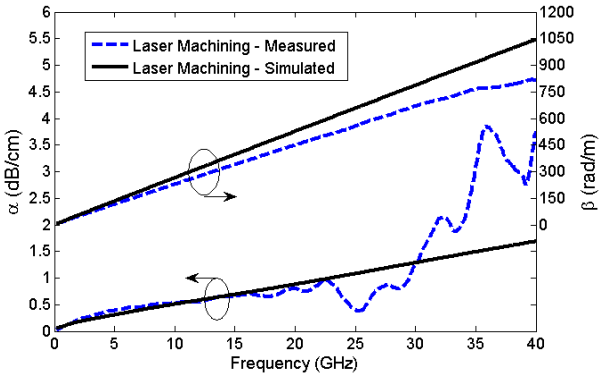

Figure 3-8: Propagation constant of laser machined slot with s = 20 μm.

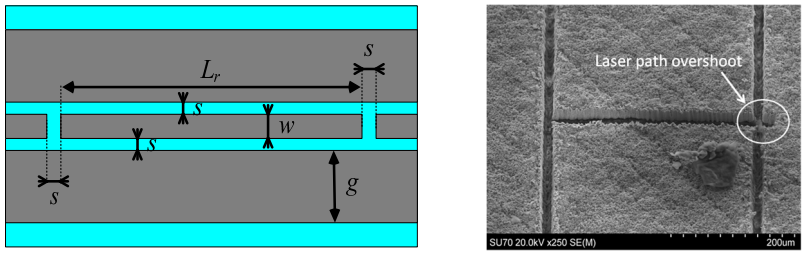

(a) (b)

Figure 3-9: (a) Illustration of series resonator. (b) Micrographs of resonator coupling slot.

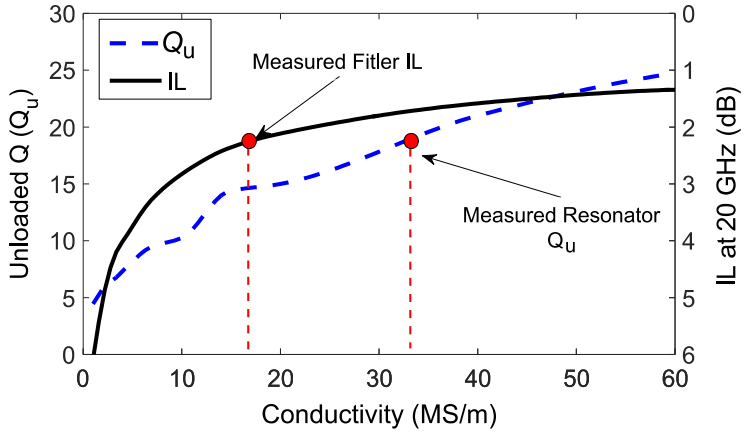

Figure 3-10: Behavior of simulated resonator unloaded Q (Q_u) at 18.35 GHz and filter insertion loss (IL) at 20 GHz, versus conductor conductivity.

A set of three identical filters is also fabricated and measured. Each filter consists of three quarter-wavelength open-ended stubs in series, similar to the ones used in [35]. The dimensions of a single stub are shown in Figure 3-11(a), and their values are $s = s_2 = s_3 = s_4 = 16.5$ μm, $w = 0.3$ mm, $w_2 = 77$ μm, $L_s = 2.87$ mm, and $L_2 = 0.15$ mm. A SEM micrograph of the interconnection of two stubs is provided in Figure 3-11(b), and the measured and simulated performance in Figure 3-11(c). The effective electrical conductivity is extracted by comparing the measured and simulated insertion loss (IL) for a matched input impedance, also known as maximum available gain (MAG), at 20 GHz, which is the center frequency. For a measured IL of 2.24 dB, the effective conductivity value is 17.5 MS/m (Figure 3-10).

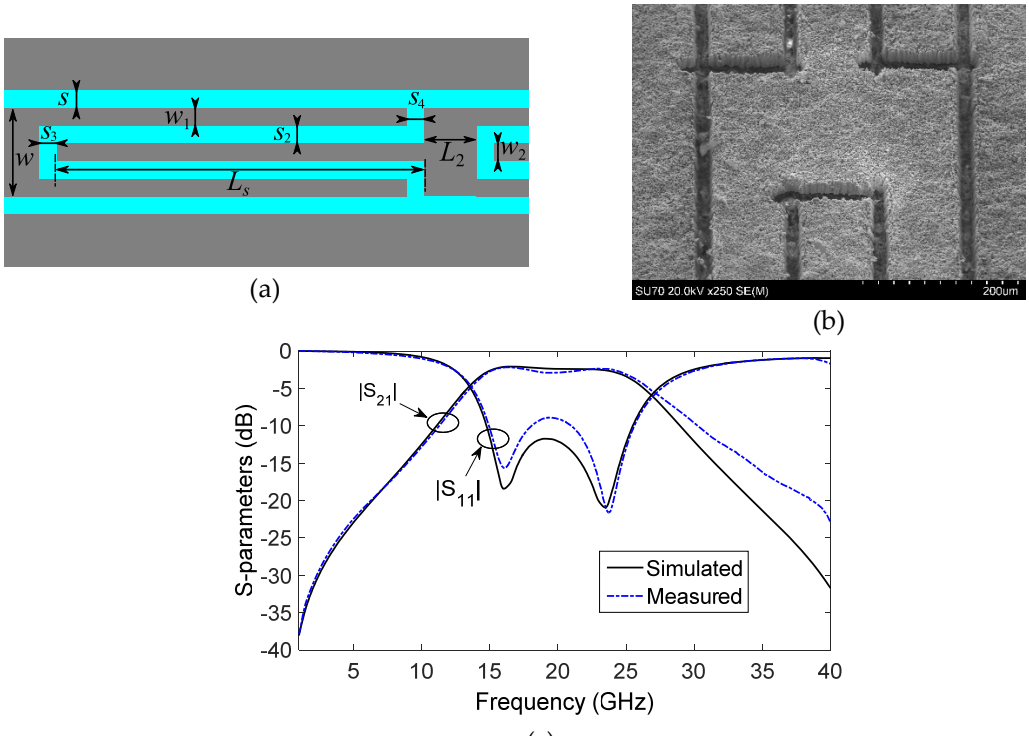

Figure 3-11: (a) Illustration of a single stub, (b) SEM micrograph of filter (rotated 90° relative to 9(b)), and (c) S-parameters.

3.3.4. Image Processing of Laser Machined Slots

It is possible to observe that the laser processing generates a solidification of the silver paste in the walls of the slots (Figure 3-7(a) and 3-12(a)). To quantify the silver solidification, image processing is used to compute the variation in volumetric density of silver ink along the x-axis, where this axis is

perpendicular to the slot wall (Figure 3-12(a)). The method is described in [27], where the SEM micrograph of the cross-sectioned slots is used to identify the solid silver regions, which are then converted into a binary matrix that is integrated to obtain the volumetric density. The results of three analyzed walls are shown in Figure 3-12(b), which indicates that the average width of the solidification (w_{Ag}) generated by the laser processing is about 2 μm.

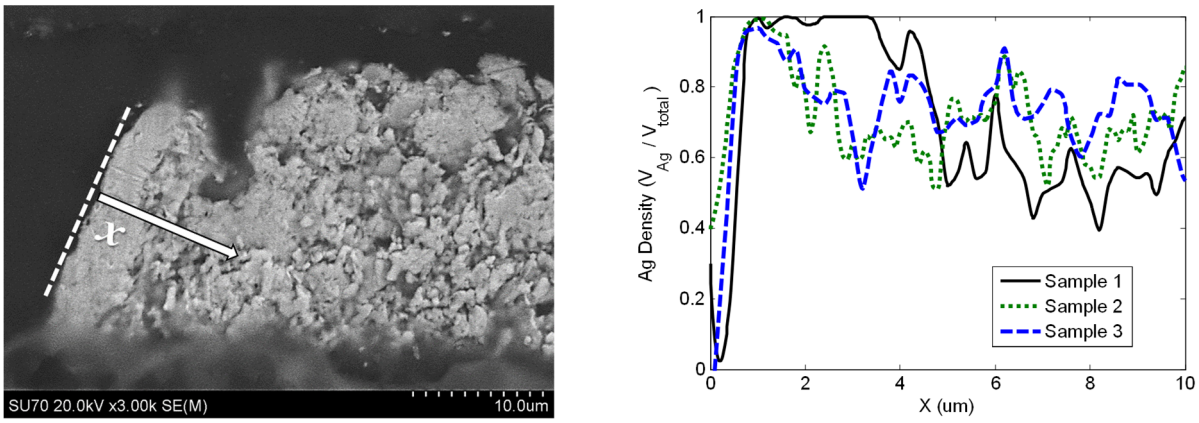

(a) (b)

Figure 3-12: (a) SEM micrograph of a laser machined slot with edge solidification (Sample 1). (b) Silver volumetric density vs. x-axis.

3.4. Modeling of Conductor Loss

The results shown in Section 3.3 suggest that the solidification of the silver ink in the edges of the laser machined slots has a significant impact on the overall loss of the circuits. To further understand and quantify the improvement in the loss due to the machining process, an analytical method presented in [75] is adapted to the scenario of non-uniform conductivities, where the computations are taken by parts to account for the different conductivity regions in the conductor. The quasi-static model is based on a conformal mapping, which is done as follows (and described in [76]).

Map the z-plane, which represents the plane of Figure 3-13(a) (where $z = x+jy$), to an intermediate t-plane, using the relationships:

$$t(x) = \frac{x}{x_3}\sqrt{(x_3^2 - x_1^2)/(x^2 - x_1^2)} \quad \text{for } |x| > |x_1| \tag{3.1}$$

and

$$t(x) = j\frac{x}{x_3}\sqrt{({x_3}^2 - {x_1}^2)/({x_1}^2 - x^2)} \quad \text{for } |x| \le |x_1| \tag{3.2}$$

where $x_1 = w/2$, $x_2 = x_1 + s$, and $x_3 = x_2 + g$. The M function shown in Figure 3-13(a) is described later in this section.

Map the t-plane to a w-plane, using the expression:

$$w(u,v) = u + jv = \int_0^t \frac{dt}{\sqrt{({t_3}^2 - t^2)({t_2}^2 - t^2)}} \tag{3.3}$$

where $t_2 = t(x_2)$ and $t_3 = t(x_3)$. This integral can be expressed as:

$$w(u,v) = t_2\sqrt{\frac{\left(1 - \frac{t^2}{{t_2}^2}\right)\left(1 - \frac{t^2}{{t_3}^2}\right)}{(t^2 - {t_2}^2)(t^2 - {t_3}^2)}}\,\text{EllipticF}\left[\text{ArcSin}\left(\frac{t}{t_2}\right), \frac{{t_2}^2}{{t_3}^2}\right] \tag{3.4}$$

where EllipticF is the elliptic integral of the first kind [77].

Figure 3-13(a) shows a single slot of the coplanar waveguide geometry, where different conductivity regions are highlighted to mimic the solidification described in Section 3.3.4; the width of the solidified silver has been exaggerated for illustration purposes. In order to carry the calculations of the series resistance of the line, the M function needs to be computed over the conductors. It represents the spatial derivative of the w-plane coordinates respect to the original z-plane coordinates. This is:

$$M(x) = \left|\frac{dw}{dz}\right| = \left|\frac{dw}{dt}\,\frac{dt}{dz}\right| \tag{3.5}$$

The final mapped geometry is shown in Figure 3-13(b) where the conductors are oriented in the vertical direction, and the darkened region corresponds to the mapped geometry of a 2 μm wide solid silver region. It is shown in [75] that the series resistance of the coplanar waveguide can be accurately modeled with the expression:

$$R(\omega) = Re\left\{\left[\int_0^{v_0} \frac{dv}{j\omega\mu_0|u_1 - u_o| + R_s\,M(u_0,v) + R_s M(u_1,v)}\right]\right\} \tag{3.6}$$

where u_0, u_1, and v_0 are the coordinates of the points depicted in Figure 3-13(b); and $R_s(\sigma, f) = (1/2)\sqrt{(\pi\, f\, \mu_0)/\sigma}$ is the surface resistance of the metal. f represents the frequency, and ω the angular frequency. Notice that the value of the R_s function will vary depending on the electrical conductivity (σ)

for a given position in the *w*-plane. The *M* function can be seen as a weighting function that is applied to R_s in (3.6). It is seen in Figure 3-13(a) that the values of *M* are considerably higher for positions that are closer to the edges of the CPW slot, therefore, the values of *Rs* in these areas have a greater contribution to (3.6).

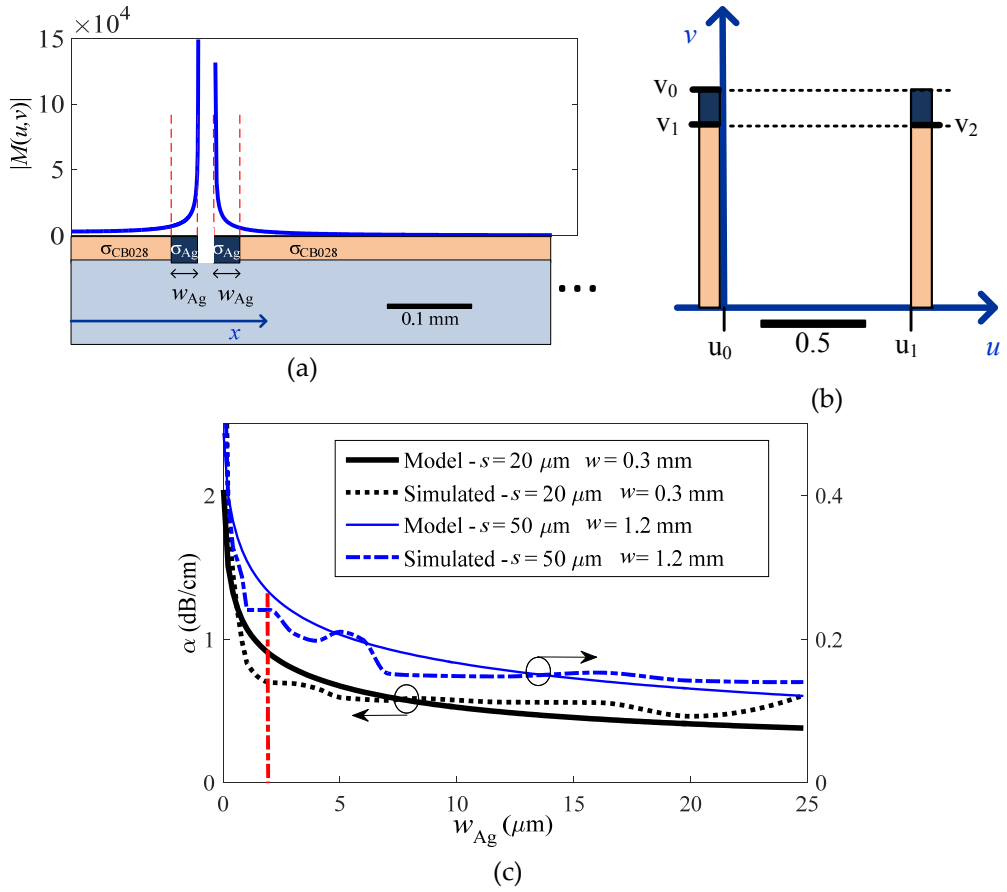

Figure 3-13: (a) |M| over the conductors (in z-plane). (b) Final mapped geometry drawn to scale (w-plane). (c) Modeled and simulated behavior of the line loss vs. solidified silver width (w_{Ag}). The frequency is 9 GHz and 20 GHz for the line with s = 50 μm and s = 20 μm, respectively.

To compute (3.6), the *M* function is sampled in the center conductor and the ground plane separately and then fitted with a 9th order polynomial (as a function of *v*), which is then analytically integrated. Since in this work we are in the presence of an inhomogeneous conductivity, where there is a 2 μm wide silver solidification around the slot, the method described above is adapted to this situation. The integral is then taken in three parts, where the first one is performed for the values of the vertical axis

v (in the w-plane) where both electrical conductivities are the one of CB028 (v = 0-v_1). The second part starts from $v = v_1$ to $v = v_2$, where the left conductor now has the conductivity of bulk silver, but the right one still has the conductivity of the silver ink (in this work v_1 can be approximated to v_2); and finally the integral for $v = v_1$-v_0, with both conductors having the conductivity of bulk silver.

Figure 3-13(c) shows the attenuation constant calculated from the conformal mapping model along with HFSS data for the transmission lines studied in this work, as a function of the width of the silver solidification region w_{Ag}. In this region, the conductivity of bulk silver is assigned, while the conductivity of bulk CB028 (1 MS/m, based on the results reported in Section 3.2) is used for the remaining conductor regions. The variable w_{Ag} is then swept using "optimetrics" in HFSS. Based on the results presented above, f is chosen to be 9 GHz and 20 GHz for the lines with 50 μm and 20 μm slot sizes, respectively. The model and HFSS data predict that the loss vs. w_{Ag} decreases abruptly for solidification widths up to around 5 μm, and has an asymptotic behavior for larger values of w_{Ag}. The loss is more sensitive to the solidification in lines with smaller center conductor width and slot sizes. The conformal mapping model is predicting 50% and 65% loss reduction for slot sizes of 50 μm and 20 μm, respectively, and a 2 μm wide solidification region. These results are consistent with the behavior observed in Section 3.3. In addition, the loss predicted by the model is very close to the measured performance shown in Figure 3-8 (refer to the red dashed line in Figure 3-13(c)), further confirming that the wall solidification is one of the main factors of performance improvement. It is noted that the model does not take into account the effects of roughness, and this simplification might impact the determination of conductivity values. Also, this approach assumes that the conductor is homogenous in the thickness direction, which does not fully represent the effects of the inhomogeneity of the CB028 layer.

3.5. Conclusions

Pulsed picosecond laser machining of micro-dispensed CB028 thick-film paste has been shown to yield well-defined features and to solidify the silver flakes in a narrow region at the edge of the machined area. As a result, there is a significant increase in the conductivity in these regions. CPW lines with laser machined slots have measured attenuation constants of 0.74 dB/cm at 20 GHz; these values are comparable to those obtained from CPW lines of similar dimensions that are fabricated using copper-clad LCP substrates. Moreover, the process described in this work enables the use of micro-dispensing for microwave structures operating up to at least 40 GHz due to the reduction of the minimum achievable slot size. The performance improvement is further confirmed with measured data on resonators and filters that show extracted effective electrical conductivities in the range 10-30 MS/m, an improvement of up to around 100x when compared with previously reported values for 3D-printed transmission lines. Table 3-1 summarizes the measured performance for the devices in this work and the extracted effective conductivities. The loss reduction is explained by adapting a conformal mapping to the non-uniform conductivity condition, which shows good agreement with simulated data, and indicates that the expected reduction of loss can be greater than 50% for the laser machined lines when compared to 3D-printed ones.

Table 3-1: Summary of the performance of the devices in this work, and extracted electrical conductivity values.

Device	Micro-dispensed slot	Laser machined slot
CPW. **s= 53 μm.**	α= 1.34 dB/cm at 9 GHz. σ_{eff}= 0.10 MS/m	α= 0.89 dB/cm at 9 GHz. σ_{eff}= 0.45 MS/m
CPW. **s= 20 μm.**	N/A (min. feature size)	α= 0.80 dB/cm at 20 GHz. σ_{eff}= 10 MS/m
Resonator. **s= 16 μm.**	N/A (< min. feature size)	Q_u= 18.5 at 18.35 GHz. σ_{eff}= 32.3 MS/m.
Filter. **s= 20 μm.**	N/A (< min. feature size)	IL= 2.24 dB at 20 GHz. σ_{eff}= 17.5 MS/m.

CHAPTER 4: MESHED GROUND COPLANAR WAVEGUIDE

4.1. Introduction

In general, for additive manufacturing (AM), the most expensive materials are the ones utilized for the conductive layer; hence, it is important to optimize the geometries with the aim of reducing conductor usage. Another immediate benefit of using a smaller amount of conductor area is reduced printing time and consequently, reduced printing cost. In this chapter, the meshed ground coplanar waveguide (MGCPW) is investigated using a comprehensive set of meshed ground sizes that are analyzed through simulation and experimental characterization. Additionally, results are compared with data on comparable finite ground CPW (FGCPW) transmission lines. Furthermore, the meshed ground concept is tested by applying it to a filter fabricated with traditional manufacturing and AM. Results show that the mesh mainly affects the insertion loss and that meshing the ground plane is a better option than simply reducing the ground width of a FGCPW line in terms of loss degradation. For example, a reduction of meshed ground CPW (MGCPW) conductor density by 50% yields an increase in loss of less than 25%, whereas the loss of FGCPW increases by >100% when the ground width is reduced in half. The microwave characterization is performed from 0.2 – 5 GHz, with detailed analysis centered at 4 GHz. In addition to the characterization of the waveguide properties, a new physical-mathematical model is presented, with which the values of capacitance per unit length and the characteristic impedance of the line are predicted with less than 5.4% error for a wide range of mesh geometries.

The content of this chapter has been published in [35] and it is included in this dissertation with permission from the IEEE. A copy of the permission is included in the Appendix A.

4.2. Performance Characteristics

4.2.1. Design and Fabrication

In order to explore the MGCPW approach, the structure in Figure 4-1 is simulated for the dimensions of w=1.44 mm, s= 200 μm, h=1.57 mm and g= 3.52 mm. The thickness of the copper cladding is 35 μm. Mesh dimensions a and b are swept from 0.1-1.625 mm and from 0.05-0.9 mm, respectively, generating 58 different combinations. The substrate selected for the simulations is Rogers RT-5870 that has a relative dielectric constant of 2.33, and a loss tangent of 0.0012. The main reason for this selection is that RT-5870 has similar properties to the ABS (acrylonitrile butadiene styrene) thermoplastic that is often used for 3D printing [78]. The software utilized for the simulations was Ansys HFSS 2014.0.7.

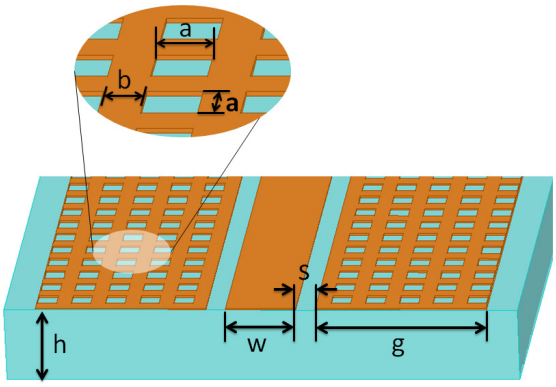

Figure 4-1: Geometry of the MGCPW.

A subset of the simulated MGCPW lines was fabricated and is shown in Figure 4-2(a), which includes for each line sample the ground conductor density D as defined in Section 4.2.2. These lines were fabricated using traditional photolithography and ferric chloride copper etching techniques. AZ 1512 photoresist and AZ 726 developer were used.

Pictures of 3D-printed lines are shown in Figure 4-2(b). The substrate of these lines is ABS, printed using a Dimension SST-768 fused deposition modeling (FDM) printer. Following the FDM process, the ABS is coated with a thin layer of Loctite epoxy to reduce surface roughness, and the metal layer is printed with an nScrypt micro-dispensing Tabletop 3Dn System using Dupont CB028 conductive

paste. The details of the fabrication process are described in [31], where a set of five 10 mm-long CPW lines with different mesh geometries is used for the characterization. Although the MGCPW approach is mainly inspired by AM, the majority of the experimental characterization in this work uses lines that were fabricated with the traditional photolithography and etching techniques. These techniques offer tighter dimensional control and yield compared to the current AM process, hence the measured data is better suited for analysis purposes.

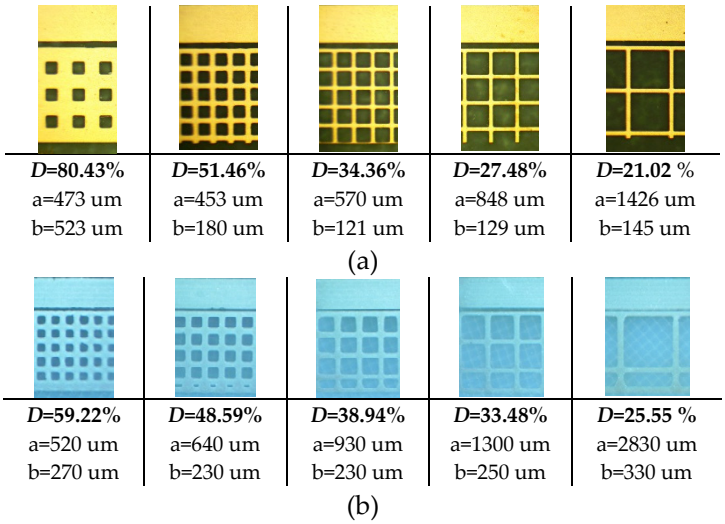

Figure 4-2: Pictures of the fabricated MGCPW lines (half of the center conductor and one ground plane) with the measured mesh dimensions. (a) Traditional fabrication. (b) 3D printed.

4.2.2. Propagation Characteristics

The fabricated set of MGCPWs on RT-5870 (Figure 4-2(a)) was characterized using a pair of 1200 micrometer pitch GSG RF probes (Picoprobe model ECP18-GSG-1200-DP), a Cascade Microtech probe station and an Agilent N5227A PNA. The PNA was calibrated with a CS-18 Picoprobe calibration substrate using the SOLT method. Figure 4-3 shows the equipment used in the measurement and a picture of the probe while measuring one of the filters in this work. The lines are placed on top of a metallic chuck for the measurements, and it was independently confirmed that potential coupling effects between the line and the chuck did not noticeably impact the measurement data. Figure 4-4 shows the measured scattering parameters of a subset of the fabricated transmission lines that are presented in

Figure 4-2. A measurement artifact observed for all lines tested in this study produced a deviation in $|S_{21}|$ of ~0.1 dB from the nominal monotonic behavior at around 1.5 GHz. However, the data in the rest of the frequency range show good agreement with the values predicted by the simulation, and no data at 1.5 GHz was utilized for the analysis presented in this work.

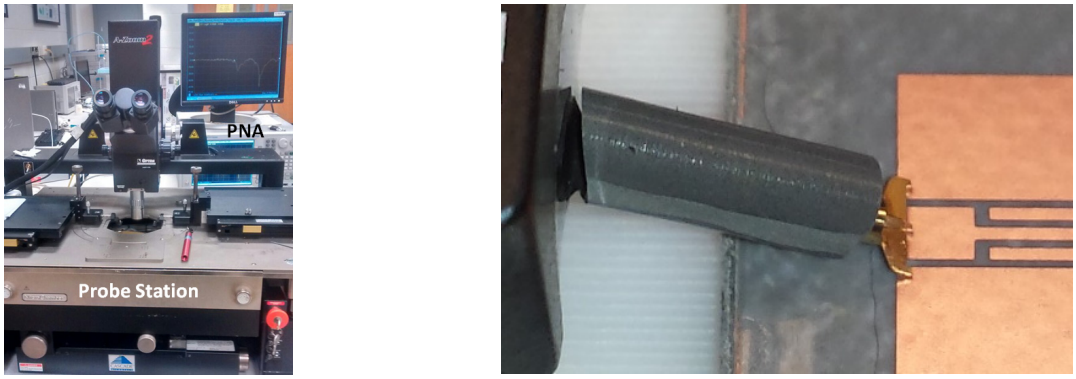

(a) (b)

Figure 4-3: Picture of the measurement set-up. (a) Probe station and PNA. (b) GSG probe while measuring one of the filters.

The properties of each transmission line (characteristic impedance, propagation constant and capacitance per unit length) are computed using the equations described in [71]. For comparison purposes a set of FGCPW lines with ground sizes (g) in the range of 0.90 – 3.46 mm was also fabricated and measured with the same setup.

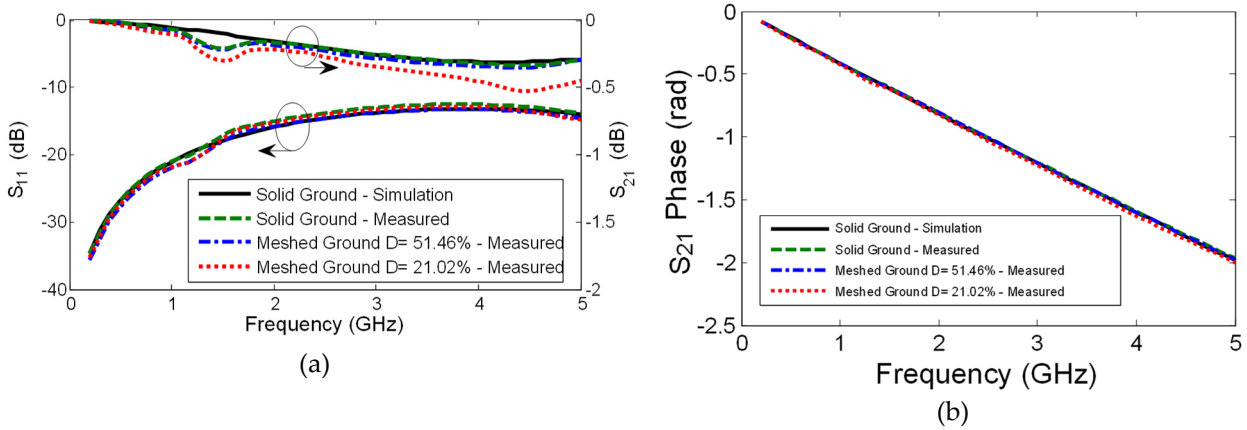

(a) (b)

Figure 4-4: Measured scattering parameters of CPW lines (meshed and solid grounds). Simulation of the solid ground version is included for reference.

The ground density (D) of the MGCPW lines is defined as the ratio of the conductor used for the meshed ground, and the conductor needed for a solid ground of the same size (g). Since the thickness of the metallization layer is assumed to be constant, D is calculated using the surface area of the ground conductor. For example, in Figure 4-2(a), the second MGCPW (left to right) has dimensions of a=453 μm, b=180 μm and g=3.45 mm, resulting in D of 51.5%; i.e., it requires approximately half of the amount of conductor for the realization of the ground, when compared to a solid ground design with the same value of g. For the FGCPW lines described in this section, D is defined as the ratio of the ground plane width to that of the line with the largest ground size (3.46 mm). I.e., D=50% for FGCPW means the ground size was reduced in half. For MGCPW, the value of D can be approximated to:

$$D = [((a+b)^2 - a^2)/((a+b)^2)] \quad (4.1)$$

To illustrate the impact of reduced ground density on the performance of the transmission lines their properties are plotted as a function of D in Figure 4-5. All data in this figure are for MGCPW or FGCPW lines on copper clad RT 5870 substrates, except for one curve in Figure 4-5(c) showing measured data for printed MGCPW CB028-on-ABS lines. Since D is a multivariate parameter that depends on both a and b it is convenient to incorporate data for the 58 combinations of line dimensions (described in Section 4.2.1) within the shaded region. The data for the specific lines shown in Figure 4-2 are plotted as the individual curves. The characteristic impedance extracted from simulated and measured data varies by <±4% for D between 20%-100%, although simulated data predicts an increase for lower densities (Figure 4-5(a)). The phase constant also remains relatively stable with changes in D, with only a nominal increase for D below ~25% (Figure 4-5(b)). Monotonic behavior of the line properties versus D is not expected due to its multivariate nature.

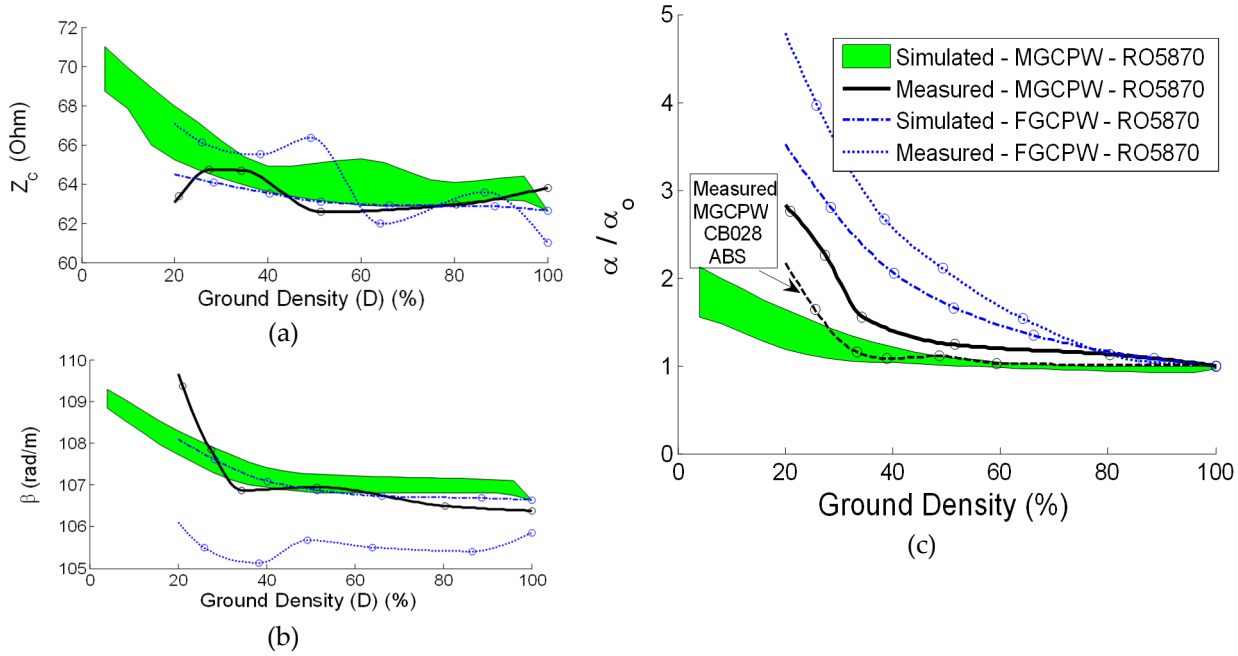

Figure 4-5: Extracted transmission line properties as a function of the ground density (at 4 GHz): (a) Characteristic Impedance, (b) Phase Constant and, (c) Normalized Attenuation Constant.

While there is minimal change in the characteristic impedance and phase constant, the attenuation constant is rather sensitive to changes in *D*. Figure 4-5(c) shows simulated and measured α values normalized to the attenuation constant at *D*=100% (α_o) for the respective line. For all simulated and measured data for the RT 5870 lines the value for α_o is ~0.7 Np/m. Due to the lower conductivity of CB028 compared to copper, and the higher surface roughness of the ABS substrate, α_o for the 3D printed MGCPW lines is ~3.3 Np/m as reported in [31]. As seen, there is a relatively flat region for MGCPW where the loss stays constant for *D* in the range of 50% - 100% and the behavior naturally holds for both methods of fabrication. In contrast, the loss for FGCPW steadily increases as the ground size reduces. The tapering of the conductor edges that results from the fabrication process, and the increasing influence of the edges as the ground density decreases, can explain the under-predictions of the simulated data compared to measured values.

4.3. Modeling of the Propagation Characteristics

4.3.1. Modeling of MGCPW

The simulated data shown in the previous section require the use of a 3D electromagnetic field solver (HFSS in this case) and hours of computational resources to generate. Here, a new physical-mathematical model is presented that provides a closed-form tool to predict the characteristics of MGCPW, specifically, the capacitance per unit length (C) and the characteristic impedance (Z_c). Since the geometry in Figure 4-1 represents a periodic structure, it is divided into cells that are conformed by a segment with a meshed ground of length a (with capacitance C_A) and one with a solid ground of length b (and capacitance C_B), as shown in Figure 4-6. The geometry of the C_B segment represents the traditional FGCPW, whose analytical expression for capacitance is well known and can be found in [74]. Its capacitance per unit length is computed using conformal mapping, having the form of:

$$C_B = 2C^a + C_2 \tag{4.2}$$

where C^a is the mapped capacitance per unit length when the half-plane is filled by air, and C_2 is the resulting capacitance when the same half plane is occupied by the dielectric.

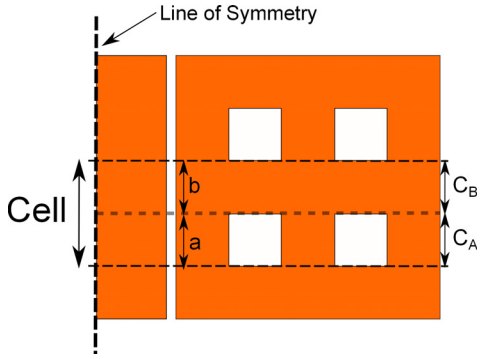

Figure 4-6: Geometry of the MGCPW cell used for modeling and the plane of symmetry.

The computation of C_A represents a greater challenge, since the ground of this segment is composed of multiple conductors. To calculate this capacitance, the metallization layer shown in Figure 4-7(a) (drawn to scale) is mapped to a rectangle (Figure 4-7(b)). The mapping is done as follows: a) map the points marked I-IV in Figure 4-7(a) to a circle using the Moebius transformation: [0 I +∞] to [-i $e^{-i\frac{\pi}{4}}$ i]

to ensure that the infinity position is properly mapped; b) map the disk to a rectangle using Schwarz–Christoffel mapping, where the points I-IV (after the Moebius transformation) are specified as the vertices of the resulting rectangular map, and the interior angles in between these points are specified as $\pi/4$ radians, resulting in the map shown in Figure 4-7(b). To perform these mapping computations, a Schwarz-Christoffel Toolbox described in [79] was utilized.

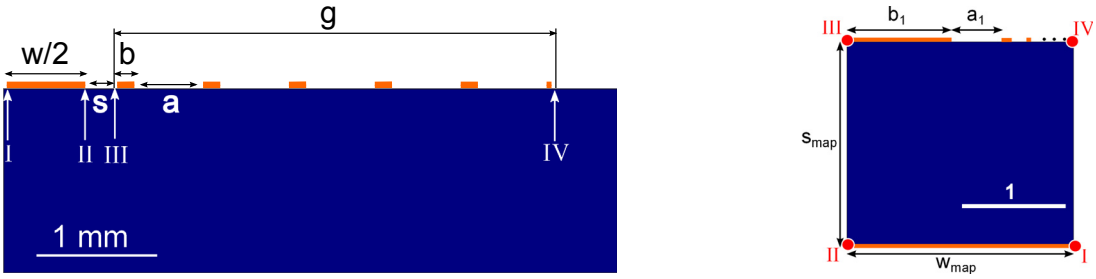

(a) (b)

Figure 4-7: Geometry mapping. (a) Cross section of the C_A segment of the cell drawn at scale. (b) Resulting mapping of C_A.

As illustrated in Figure 4-7(b), most of the contribution to the capacitance is made by the ground conductor closest to the signal line, which is expected since that is the region with greater electric field intensity. Also, it can be observed that the equivalent mapped size of the consequent ground conductors (b_i) rapidly decreases as their position moves farther from the signal line. The resulting capacitance per unit length C_A is approximated as:

$$C_A = 2C^a_{mesh} + C_{2\,mesh} \tag{4.3}$$

where C^a_{mesh} is the mapped capacitance per unit length when the half plane is filled by air, and $C_{2\,mesh}$ is the resulting capacitance when the same half plane is filled by the dielectric. Each of these capacitances is calculated using:

$$C_{mesh} = \epsilon\left[\left(W_{top} + W_{map}\right)/(2\,S_{map})\right] \tag{4.4}$$

where ϵ is the corresponding dielectric constant ($\epsilon=\epsilon_0$ in the case of air and $\epsilon=\epsilon_r\epsilon_0$ in the case of the dielectric), S_{map} is the distance resulting from the mapping of the CPW gap s, W_{map} is the mapped width of

the CPW center line, and W_{top} is the addition of mapped widths of the n conductors segments resulting from the meshed ground (of width bi each),

$$W_{top} = \sum_{i=1}^{n} b_i \tag{4.5}$$

To obtain the total capacitance per unit length, a weighted average using the values of C_A and C_B, computed with (5.2) and (5.3), is found using their corresponding cell lengths (a and b, respectively), with the equation:

$$C_{Cell} = [(a\ C_A + b\ K_B\ C_B)/(a + b)] \tag{4.6}$$

where K_B is a weighting factor. This weighting takes into account the fringing capacitance present in the boundary between the two segments of the cell. A value of K_B= 205 is the optimum value for the range of mesh parameters included in the study, making the model agree very well with the simulated data. The optimal K_B value maximizes the correlation of the simulated capacitance and the capacitance from the mode, as a function of a and b. K_B is obtained using a script that sweeps its value and computes the mentioned correlation for each point of the sweep. A high value of K_B is expected, since the fringing fields partially fill the holes in the conductor as indicated in [80], making the overall capacitance less dependent on the size of the holes (or a in this case).

Since the proposed model predicts the capacitance of the structure having air as the dielectric, as well as the capacitance with the half plane filled with a substrate in a separate manner as shown in (4.3) and (4.4), it allows the characteristic impedance of the line to be calculated. From [74], the fundamental expressions to calculate the characteristic impedance Z_c are:

$$\epsilon_{reff} = C_{Cell}/C^a_{Cell} \tag{4.7}$$

$$Z_c = \frac{1}{c\sqrt{\epsilon_{reff}}C^a_{Cell}} \tag{4.8}$$

where ϵ_{reff} is the effective dielectric constant of the MGCPW, and C^{a}_{Cell} is the total capacitance of the cell calculated with the previously described approach, but only considering the air capacitances. In (5.8), c represents the speed of light in vacuum.

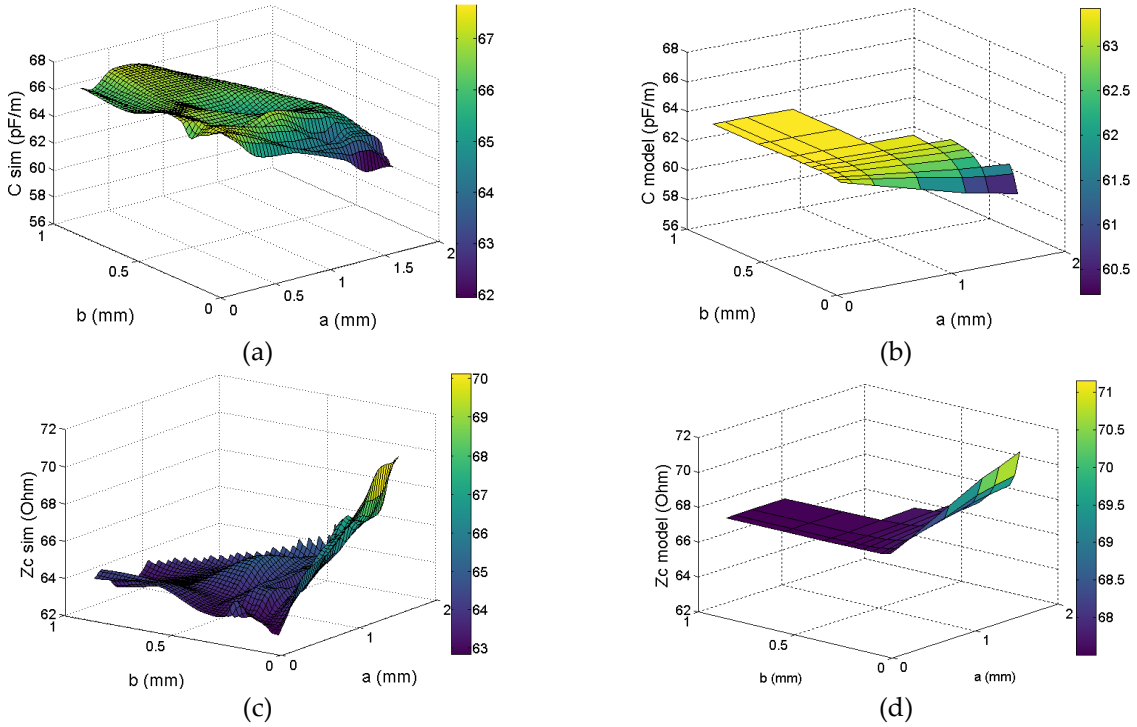

Figure 4-8: MGCPW characteristics vs. mesh size. (a) Simulated capacitance. (b) Capacitance model. (c) Simulated characteristic impedance. (d) Characteristic impedance model.

Figure 4-8 shows the capacitance per unit length and the characteristic impedance of MGCPW as obtained from full-wave simulations, as a function of the mesh size. In the same figure, the predicted values of the same properties using the model proposed in this work are shown. The Mean Absolute Error (MAE) of the capacitance model is 3.9% with a maximum error value of 5.4%, with respect to the simulated data. Also, the correlation coefficient between the simulated data and the model is 89.3%. The MAE for the characteristic impedance model is 3.48% with a maximum error of 5.8%, compared to simulations. The maximum errors occur for the lowest simulated value of b (b=50 μm). The correlation coefficient between the model and the simulated impedance value is 91.6%. The model and simulations

show that the capacitance per unit length decreases for lower *D*, where at the same time, the characteristic impedance increases.

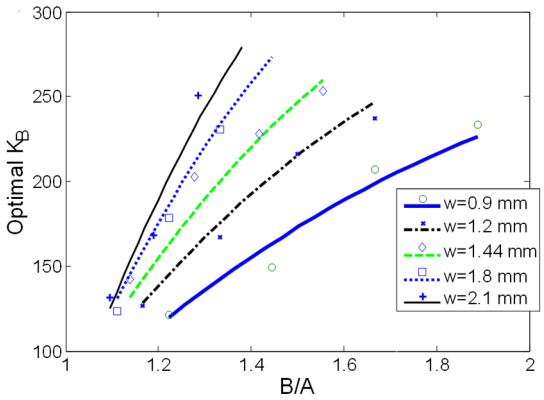

Figure 4-9: Optimal K_B for different values of s and w.

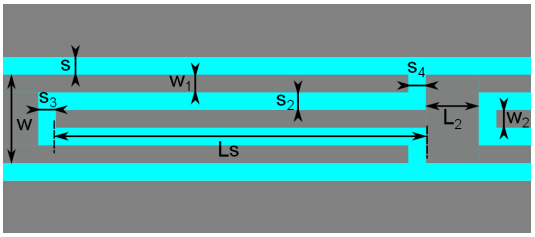

Figure 4-10: Physical dimensions of a single CPW series stub.

This model can be applied to lines with different substrates and dimensions by properly adjusting the weighting factor K_B. A wide sweep of the line dimensions with the same substrate was performed to compute the optimal K_B for values of w in the range of 0.9-2.1 mm and s in the range of 100-400 μm. For each combination, the mesh dimensions were swept in the same range defined in Section 4.2 for a and b. The optimal K_B is found by using the script previously described, for the entire mesh dimension sweep. Figure 4-9 shows the design curves as a function of the ratio of B/A, where $A=w/2$, and $B=w/2+s$, for different values of w. In this figure, the markers represent the data obtained from simulations and the lines a second-degree polynomial fit to these data is given by:

$$K_B(s,w) = 26 + 433\,s + 71.5\,w - 394\,s^2 + 132\,sw - 26.8\,w^2 \qquad (4.9)$$

for the range of $0.1 < s < 0.2$ and $0.9 < w < 2.1$, with units in mm for both variables. Using (5.9) the worst case differences observed between simulated (HFSS) properties and model-predicted properties are

<10%. Although not presented here, a similar polynomial for other substrate types can be determined as was verified in a limited number of test cases.

4.3.2. Extension Through Scaling

The interconnect dimensions, and substrate properties (ϵ_r in the range of 2-3) used in this work are compatible with 3D printing. However, when properly constrained, the meshed ground properties are applicable to different length scales and substrates. As detailed in [81], the scaling of meshed ground lines can be addressed by examining the boundary condition on the surface of the conductor and utilizing expressions for the electric field generated by screens with periodic apertures. From that analysis, the dispersion relation has the form

$$f_1\left(k_0\sqrt{\epsilon_{reff}}(a+b), k_x(a+b)\right) + \sqrt{\epsilon_{reff}}R_s f_2\left(k_x(a+b)\right) = 0 \tag{4.10}$$

whereas, the characteristic impedance of the line is expressed as:

$$Z_c = \frac{1}{\sqrt{\epsilon_{reff}}} f_3\left(k_0\sqrt{\epsilon_{reff}}(a+b), k_x(a+b)\right) \tag{4.11}$$

where f_1, f_2, and f_3 are functions of the variables shown in the equations; $(a+b)$ is the length of a single cell of the MGCPW, as pictured in Figure 4-1, k_0 is the wavenumber, k_x is the propagation constant, and R_s is the sheet resistance of the conductor. By scaling all the dimensions of the structure by the same factor the dispersion relation will remain satisfied if the factors $k_x(a+b)$, $k_0\sqrt{\epsilon_{reff}}(a+b)$, and $\sqrt{\epsilon_{reff}}R_s$ are kept constant, according to [81]. The characteristic impedance will be affected by the factor $1/\sqrt{\epsilon_{reff}}$. These constraints define the scaling of substrate permittivity, line dimensions and frequency range over which the presented MGCPW properties can be extended.

4.3.3. Frequency Limitations

It is well known that waves in periodic structures will not propagate, or at least have a minimum in the group velocity, when the separation between the cells is half of the guided wavelength. This

condition occurs at the Bragg frequency. Referring to the geometry shown in Figure 4-6, this condition occurs when

$$\beta(a+b)=\pi. \tag{4.12}$$

Given the dimensions of all lines used in this work, the minimum Bragg frequency is ~100 GHz. Additionally, the maximum frequency (f_{max}) to avoid higher order modes propagating in the CPW structure is estimated in [82] using (5.13). The lowest f_{max} value for the lines presented in this study using is ~41 GHz.

$$f_{max} \cong \frac{1}{Max\left\{h, \frac{w}{2}+s+g\right\}\sqrt{2\mu_0\epsilon_0(\epsilon_r-1)}} \tag{4.13}$$

4.4. Proof of Concept

To test the MGCPW concept, a set of filters is designed, fabricated and measured. The filter topology consists of three quarter-wavelength open-ended stubs in series. Figure 4-10 shows the geometry of a single stub. The filters were designed for a center frequency of 3 GHz, and bandwidth of 2 GHz. One set of filters was realized using conventional PCB etching techniques with a RT 5880 1 oz. copper-clad Rogers substrate with a ground density of 35% (Figure 4-11(a)). A second set of filters was fabricated using micro-dispensing of CB028 silver paste onto a bare RT 5880 substrate (Figure 4-11(b)) that has a ground density of 70%. The thickness of the CB028 layer is ~30 μm. Close-up photographs of the filters are shown in Figure 4-12 and the filter dimensions are given in Table 4-1. In Figure 4-12 it is possible to appreciate that the edges of the metallization are less defined when compared to the lines presented in Figure 4-2. This difference is mainly due to the change of substrate, as the ink behaves differently on the epoxy coated ABS, than it does on Rogers RT 5880, mostly due to difference in roughness and surface tension. The printing settings, such as the printing nozzle and speed, also affect the edge quality. The scattering parameters of the filters were obtained using the same setup described in

Section 4.2.2. Figure 4-13 shows the responses for the solid ground (SG) and the meshed ground (MG) versions of the filters.

In order to compare the filter loss performance and account for differences in the reflection coefficient, the average insertion loss was calculated in the range of 2.5-3.5 GHz (with 21 linearly spaced points) using the equation:

$$IL = [\,|S_{21}|^2/(1-|S_{11}|^2)] \qquad (4.14)$$

where the scattering parameters are in linear format. Table 4-2 shows the comparison of the computed average for the meshed and solid ground designs. For the filters with Cu conductors the meshed ground increases the insertion loss by just 22% (when compared to the filter with a solid ground) despite the fact that the meshed ground has 65% less conductor. The IL performance of the meshed ground filter with CB028 conductors is ~11% better than that of the solid ground filter. This result can be explained by the fact that the micro-dispensing approach results in some variation in the physical dimensions, as noted in Table 4-1. Also, Figure 4-13(b) shows that the S21 response of the solid ground filter has two dips that are not present in the meshed ground version, and which increase the average insertion loss of the solid ground version. However, this figure also indicates that for high ground densities (*D*= 70% in this case for the printed filter), the performance degradation is minimal. The printing time is reduced from ~215 seconds for the solid ground filter, to ~176 seconds with the meshed ground approach, and this can be further improved by optimizing the micro-dispensing algorithms.

Table 4-1: Physical dimensions of the fabricated filters. (for the printed filters, the dimensions are the average across the measured region).*

Dimensions (mm) / Filter	*W*	*s*	*g*	*a*	*b*	*Ls*	S_2	S_3	S_4	W_1	W_2	L_2
Copper – SG	1.391	0.223	3.46	-	-	17.23	0.224	0.379	0.379	0.312	0.379	1.363
Copper – MG	1.402	0.219	3.46	0.551	0.122	17.25	0.215	0.383	0.390	0.305	0.311	1.379
CB028 – SG*	1.516	0.118	3.56	-	-	17.15	0.195	0.266	0.285	0.347	0.397	1.742
CB028 – MG*	1.477	0.219	3.48	0.425	0.320	17.39	0.199	0.423	0.371	0.320	0.398	1.578

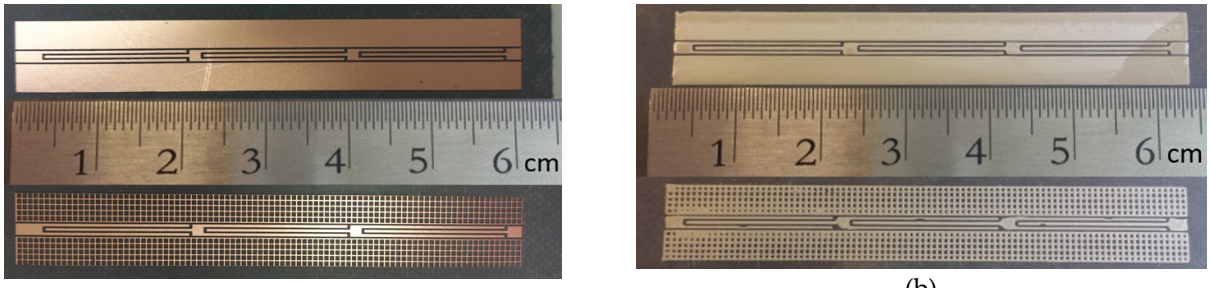

(a) (b)

Figure 4-11: Pictures of the fabricated filters (SG and MG). (a) Traditional fabrication method (D= 34.7% for MG). (b) 3D Printed (D= 70.4% for MG).

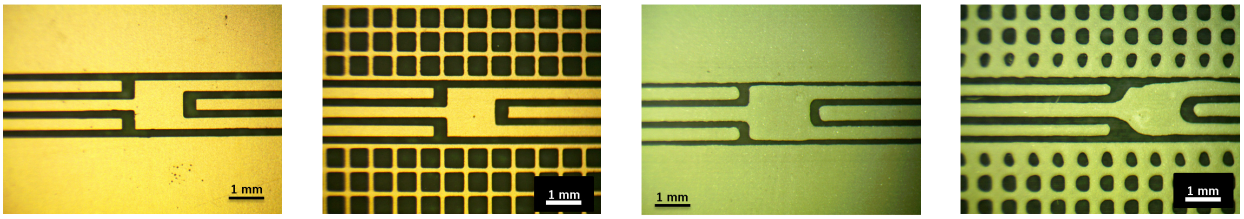

(a) (b) (c) (d)

Figure 4-12: Pictures of fabricated filters: (a) solid ground Cu on RT 5870, (b) meshed ground Cu on RT 5870, (c) solid ground CB028 on ABS, and (d) meshed ground CB028 on ABS.

4.5. Conclusions

Using a meshed ground CPW (MGCPW) interconnect is an effective way to reduce the amount of conductive material used in 3D printed microwave circuits, also reducing the cost and printing time. It has been shown that the characteristic impedance and phase constant are relatively insensitive to the use of a meshed ground, for mesh densities as low as 20-25%. The attenuation constant is more dependent on mesh density, although for densities as low as 50% there is only a nominal (<25%) increase in loss for the MGCPW approach. In contrast, reducing the amount of conductor usage by narrowing the ground plane of a FGCPW line shows a significantly greater increase in loss for all mesh densities; the use of FGCPW with half of the ground size yields an increase of 108% in the insertion loss. As a design guideline, the values of a and b that result in a density (*D*) of around 50%, using (4.1), offer a good compromise between conductor usage reduction and increase in loss. A physical-mathematical model is presented in this work that predicts the capacitance per unit length and characteristic impedance of MGCPW with less than a 5.4% error over a wide range of line dimensions. Finally, the sensitivity of the loss of MGCPW lines to

mesh density is validated by comparing the performance of meshed and solid ground band-pass filters. The performance of bandpass filters with ~60% bandwidths are shown to be minimally impacted when the ground density is reduced to 35%.

Table 4-2: Insertion loss and effective conductivity of the fabricated filters.

Filter	Insertion Loss (dB)	Efficient Conductivity (σ_{ef}) (S/m)
Solid Ground – Copper	0.3	6.4e7
Meshed Ground – Copper *D*= 35%	0.4	3.5e7
Solid Ground – CB028	1.6	7.9e5
Meshed Ground – CB028 *D*=70%	1.5	9.2e5

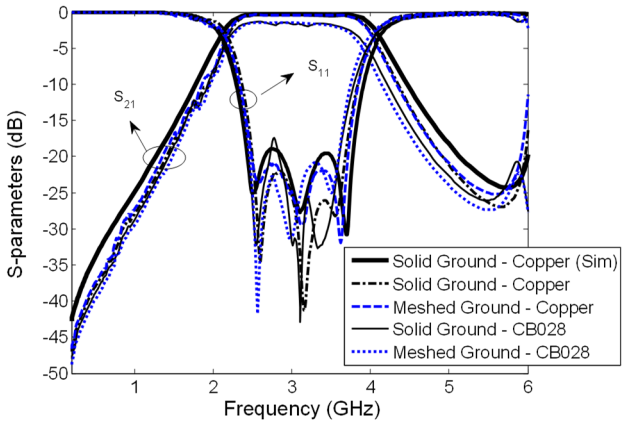

(a)

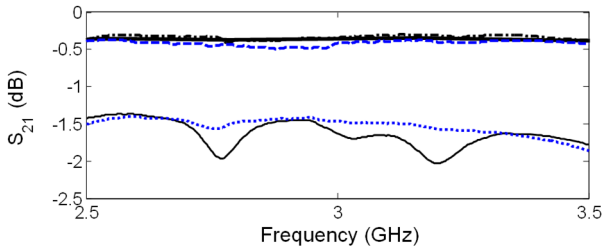

(b)

Figure 4-13: Measured scattering parameters of the fabricated filters. (a) Scattering parameters. (b) Transmission coefficient in the passband.

CHAPTER 5: BINDER JETTING FOR 3D-PRINTING OF METALLIC WAVEGUIDE CIRCUITS AND ANTENNAS

5.1. Introduction

Novel additive manufacturing (AM) technologies are enabling high frequency circuit performances that are comparable to, or in some cases better than what can be obtained from traditional manufacturing. These performance achievements parallel the overall rapid advance of AM capabilities that have in part been due to the relatively modest capital equipment costs, low cost of materials and maintenance, and fast turn-around time from design to printed component. For example, in contrast to thin-film fabrication, there is no need for a clean room or masks. Moreover, the complexity of the additively manufactured structures is not necessarily correlated to the cost of manufacturing. Hence, AM is a technology that empowers the designer with tools to create optimal circuit and antennas structures that may not be possible to realize, or not cost efficient when made by traditional means.

Progress has been reported in the area of multilayer planar RF circuits and antennas with technologies such as the ultrasonic wire embedding technique [20], inkjet printing [15], and direct print additive manufacturing (DPAM) [27, 28]. Furthermore, technologies such as aerosol jet printing (AJP) [17], polymer multichip module (PMM-P) [34], and the combination of laser machining and DPAM [83], have shown capability to fabricate low-loss circuits in the mm-wave frequency range.

In the area of medium to high power waveguides, such as air-filled rectangular waveguides, different AM technologies are available. Among those technologies are copper plated plastics [43], selective laser melting (SLM) of metals [52, 54, 55] and 3D copper additive manufacturing (3D-CAM) [61]. Binder-jetting (BJ) is an alternative technology that has been previously used to fabricate all-metal

antennas [84-86]. BJ leverages inkjet printing for high throughput and can cost significantly less than other metal AM techniques such as laser sintering and electron beam systems. BJ produces green parts that are typically infiltrated and/or sintered to achieve final properties [87-89]. 3D-printing, in general, enables the realization of complex geometries in one piece, such as microwave filters as demonstrated in [43, 56, 62, 90-93].

In this chapter, the performance of Ka-band circuits and antennas manufactured using BJ is characterized. The parts are made of 316 stainless steel (316 SS) that is infiltrated with copper or bronze. The 3D printing composites are characterized by scanning electron microscopy (SEM), energy dispersive spectroscopy (EDS), and DC conductivity which is measured using the Van der Pauw four-point probe method. Ka-band rectangular cavity resonators, straight WR-28 waveguide sections, and a 4 pole Chebyshev band-pass iris filter are used to benchmark the RF performance. The best achieved measured unloaded Q factor for the cavity resonators is 616, and the average attenuation of the WR-28 waveguide sections is 4.3 dB/m. Both results apply for the copper infiltrated stainless steel composite.

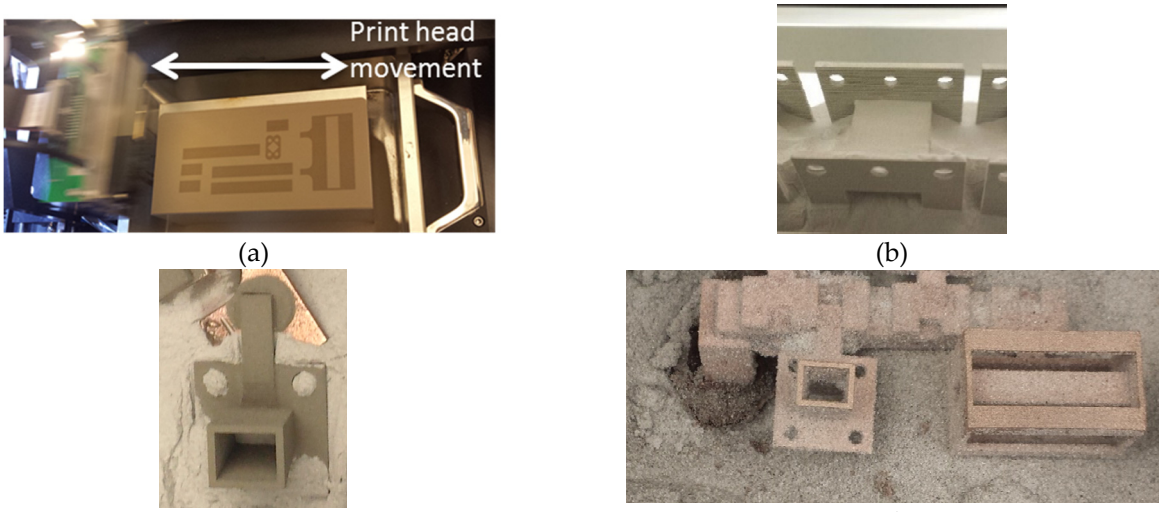

Figure 5-1: Binder jetting printing process. (a) Printed binder on a SS layer in the printing bed. (b) De-powdering process. (c) Part inside a graphite crucible, connected to a runner, and surrounded by alumina powder. (c) Parts after the infiltration process is complete.

To further demonstrate the capabilities of BJ, a compound meshed parabolic reflector antenna system is designed and fabricated. This antenna has a feed network that includes the illuminating horn,

rectangular waveguide section, and a filter, all in one piece. This monolithic approach eliminates the need for joints, which can be a source of failure, especially in satellites that are subject to vibrations during deployment. These joints are also known to generate passive intermodulation (PIM) [94]. Using a meshed surface for the reflector offers 40% reduction in weight, when compared with the solid version, while having minimal effect on the antenna gain, which is 24.56 dBi at 33.5 GHz.

5.2. Fabrication and Material Characterization

5.2.1. Fabrication

The parts in this work are fabricated with an ExOne Innovent metal binder jet printer in a process that is described in [86, 95]. First, the part is designed using Ansys HFSS 2016.2, and the 3D model is exported as a .step file. This file is optimized for BJ printing then converted to stereolithography format (.stl) with Solidworks 2014. The printing process starts by coating the printing bed with a uniform layer of powdered stainless steel; a counter rotating roller ensures uniform layer thickness. The print head then deposits liquid binder on the corresponding cross section of the part in the powder, as shown in Fig. 5-1(a). The binder used in this work has a proprietary formulation by ExOne, which is not disclosed. This process of binder printing and powder recoating is repeated until all the layers have been printed. The part is then placed in an oven for 4 h at 185°C to finish curing the binder. The part is then de-powdered and removed from the printing box as seen in Fig. 5-1(b). The part is considered in its green state as it is only held together by dried binder. Next, the parts are placed into a graphite crucible and arranged to contact a sacrificial connector called a runner. This makes a physical connection forming a sacrificial bridge between the infiltrant metal and the green component to be infiltrated. The other end of the runner is embedded in the infiltrant metal powder. The entire crucible is then filled with alumina powder, surrounding and supporting the component as shown in Fig. 5-1(c). The crucible containing the parts is placed in a sintering oven that reaches 1200°C during a 24 h cycle. During this infiltration cycle, all of the binder is burned off and the high temperatures cause the metal powder particles to fuse together but do

not completely melt. However, the infiltrant metal has a lower melting temperature and transitions to a liquid at this temperature. The liquid infiltrant metal is absorbed into the pores of the green part creating a composite material with 100% density. Finally, the parts are removed from the crucible (Fig. 5-1(d)) and the sacrificial runner which was eroded by the copper entering the surface is removed and discarded. In this work, 316 SS powder is utilized for the binder jetting process and either bronze or copper is used as a second metal for the infiltration process.

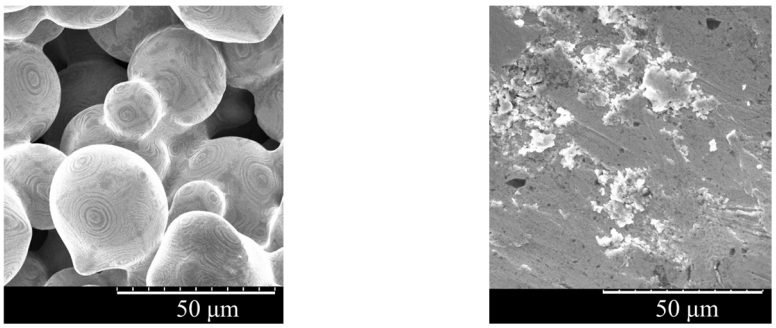

(a) (b)

Figure 5-2: SEM micrographs of 3D-printed metal samples: (a) Non-infiltrated and (b) Copper infiltrated.

5.2.2. Material Characterization

Stainless steel (SS) is the typical material used in BJ, although its electrical conductivity is relatively low compared to materials such as silver, gold and copper that are more commonly used for good RF performance. An SEM image of a sintered BJ-printed SS part without infiltration is shown in Fig. 5-2(a). Due to the relatively coarse powder size (30 µm mean diameter), the powder does not densify significantly during sintering alone, leaving a large void space that further decreases the effective RF conductivity. This is one of the main reasons a second metal is used for infiltration, to create a composite that is 100% dense. Fig. 5-2(b) shows the surface finish of a sample after it is infiltrated with copper.

Energy dispersive spectroscopy (EDS) was conducted on BJ-printed parts to determine the composition of the composite structure. EDS allows for viewing of specific elements and their location on the viewing surface. A sample part was infiltrated and then cut in half and polished to get a clear view of the cross section. Iron (Fe) and Chromium (Cr) are components of SS and can be seen in particle-like

shapes surrounded by copper (Cu) in Fig. 5-3. The weight composition percentage are 10.73, 56.2, and 33.07, for Cu, Fe, and Cr, respectively. SEM images of waveguides fabricated with different AM technologies can be found in [96].

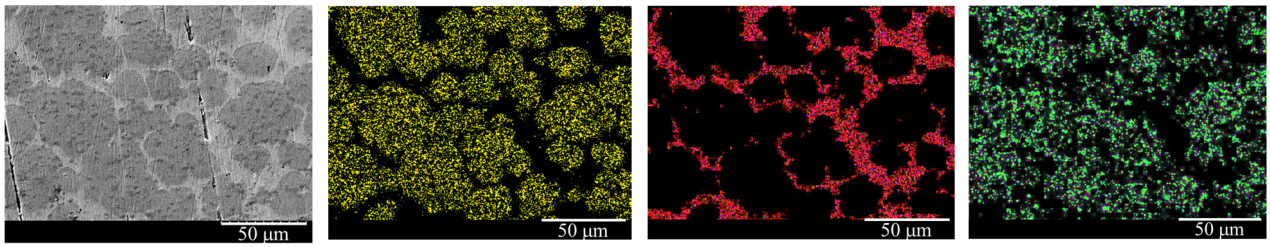

(a) (b) (c) (d)

Figure 5-3: EDS map of polished 316SS+Cu printed sample. (a) SEM image of the composite microstructure. (b), (c), and (d) EDS maps corresponding to Fe, Cu, and Cr, respectively, where lighter areas correspond to the element.

5.3. Circuit Performance

The DC electrical conductivity σ_{DC} of the stainless steel-copper composite used in this work was previously reported in [58, 95]. The values are measured using the Van der Pauw method with printed samples of dimensions 10 mm x 10 mm x 0.25 mm. SS shows a σ_{DC} of 0.57 MS/m, after the sintering process. The values for 316 SS+Bronze and 316 SS+Cu infiltrated composites are 1.96 MS/m and 3.73 MS/m, respectively.

In what follows, the RF circuit performance is characterized using cavity resonators, a straight waveguide section, and a filter. An effective electrical conductivity is used as a parameter to compare the performance of the structures. The S-parameters are measured using an Agilent N5227A PNA. For the resonators, the PNA was calibrated using a Keysight 85056A kit. The Thru-Reflect-Line (TRL) method is used for calibration. For the WR-28 devices, a Space Machines & Engineering rectangular waveguide calibration kit is used.

5.3.1. Rectangular Cavity Resonators

The RF performance of the printed composites is benchmarked using 3D-printed rectangular cavity resonators (Fig 5-4(a)) designed to resonate at 30 GHz. A cross-section of one of these resonators is

shown in Fig 5-4(b), where the cavity dimensions are 7 mm x 7.11 mm x 5 mm, in the x, y, and z-direction, respectively. This cavity is surrounded by a structure designed to attach k-type coaxial connectors, and in the z-direction is enclosed by a layer of metal that is 0.5 mm thick on the bottom and top faces. The cavity is coupled to the connectors by round windows with a diameter of 2 mm. These two windows are placed in opposite corners in of the xy plane, one at z=0 mm and the second at z=5 mm, to minimize coupling between the ports. The quality factor is extracted from the measured transmission coefficient (S_{21}), using the expressions described in [97].The loaded quality factor (Q_l) is computed with the equation:

$$Q_l = \frac{f_{res}}{\Delta f_{3dB}} \tag{5.1}$$

where f_{res} is the resonance frequency, and $\Delta f_{3dB}$is the 3 dB bandwidth of S_{21}. The external quality factor (Q_e) is computed with:

$$S_{21}(dB) = 20log_{10}\left(\frac{Q_l}{Q_e}\right) \tag{5.2}$$

using the S_{21} value at the resonance frequency. Finally, the unloaded quality factor is computed with the well-known expression:

$$\frac{1}{Q_l} = \frac{1}{Q_u} + \frac{1}{Q_e}. \tag{5.3}$$

Table 5-1 summarizes the extracted Q_u values and the corresponding extracted effective electrical conductivities. This effective conductivity is obtained by matching the measured response to simulations using Ansys HFSS 2016.2. Based on the measured Q values, the 316 stainless steel and copper composite is selected to fabricate the rest of the devices in this work, since it offers better effective electric conductivity than the 316 SS and bronze composite.

Table 5-1: Measured resonance frequency, transmission coefficient (S_{21}), unloaded Q, and extracted conductivity for resonators made with stainless steel (SS) and copper composite, and SS and bronze composite.

Composite	Resonance Frequency (GHz)	S_{21} (dB)	Unloaded Q (Q_u)	Effective Cond. (MS/m)
316 SS + Copper	29.70	-31.81	616	0.78
316 SS + Bronze	30.05	-35.04	466	0.40

(a) (b)

Figure 5-4: 30 GHz cavity resonator. (a) Resonator with connectors. (b) Cross-section of resonator.

5.3.2. WR-28 Straight Section and Filter

Fig. 5-5(a) shows a picture of a 3D-printed straight section of Ka-band rectangular waveguide, with a standard WR-28 flange (a = 7.11 mm, b = 3.57 mm, length = 11.67 mm). A defect on the lower part of one of the flanges of the waveguide can be observed; it was created during post-processing of the part. The flanges are mechanically polished to ensure proper connection. A wet tabletop polisher is used, going from 120 to 800 grit in 4 steps. This structure shows an average loss of 4.3 dB/m across the band (Fig. 5-5(b)), which corresponds to an effective electric conductivity of 1 MS/m. To further test the performance of the 3D printed composite, a four pole Chebyshev cavity filter is designed for a center frequency of 32 GHz, and a bandwidth of 2 GHz. It is implemented as an H-plane iris filter. The design process is described in [98]. A cross-section of the printed filter is shown in Fig. 5-6(a); where the dimensions are depicted. The design values of the dimensions are w1 = 4.06 mm, w2 = 2.99 mm, w3 = 2.74 mm, L1 = 4.6 mm, L2= 5.56 mm, and t= 1 mm. Fig. 5-6(b) shows the measured response of the filter, which exhibits an average loss of 1 dB across the band. The average deviation between the dimensions of the cavities and coupling windows in the 3D CAD model and the printed part is 90 μm, resulting in larger apertures that generated a frequency shift in the filter response. Simulation results using the as-fabricated filter dimensions are included in Fig. 5-6(b) (Adjusted Simulation).

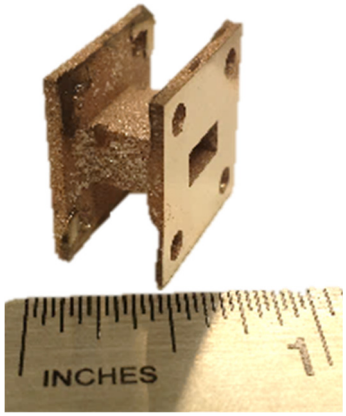

(a)

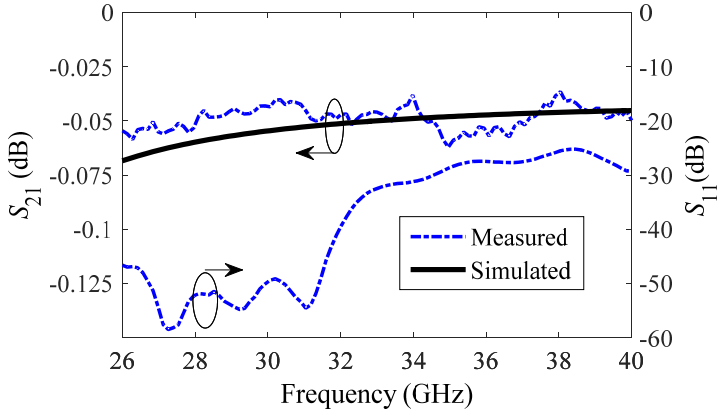

(b)

Figure 5-5: WR-28 rectangular waveguide: (a) Picture of the fabricated waveguide. (b) Measured and simulated response.

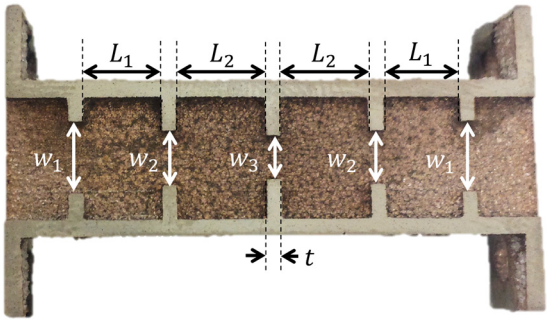

(a)

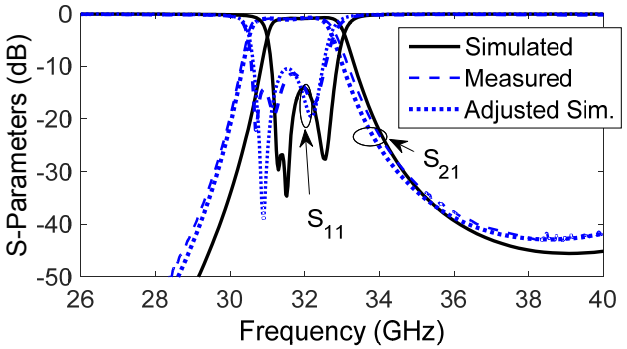

(b)

Figure 5-6: 3D-printed filter: (a) Cross-Section. (b) Measured S-parameters.

When the mismatch losses are extracted, the measured average in-band dissipative loss of the filter is 0.71 dB, which corresponds to an effective electric conductivity of 1.3 MS/m. The simulated values of the filter dissipative loss and resonator Qu are presented in Fig. 5-7 to illustrate the sensitivity of these parameters to the effective conductivity.

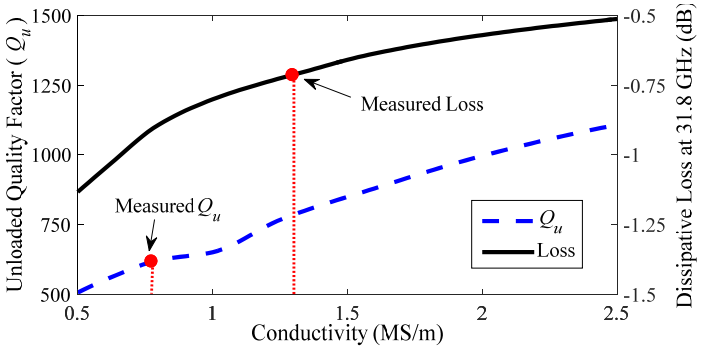

Figure 5-7: Simulated behavior of unloaded quality factor (Qu) of the resonator in Fig. 5-4, and filter dissipative loss as a function of electric conductivity.

Table 5-2: Comparison of bj printed waveguides with other additively manufactured rectangular waveguides.

Waveguide standard	Frequency (GHz)	Technology	Material	Split block	Surface Roughness Ra (μm)	Attenuation (dB/m)	Attenuation (dB/λ_g)	Reference
WR-90	10	FDM	Copper plated ABS	No	4.99	0.33	0.013	[43]
WR-42	18-26.5	FDM and ink dispensing	Silver ink coated ABS	No		27	0.478 at 22.25 GHz	[99]
WR-42	18-26.5	BJ	420 SS + Cu composite	No	6.26	1.9	0.033 at 22.25 GHz	[95]
WR-28	26.5-40	BJ	420 SS + Cu composite	No	6.26	4.3	0.050 at 33.5 GHz	This work
WR-12	60-90	SLM	Cu_15Sn	No	6	7.51	0.039 at 75 GHz	[53]
WR-10	110	SLA	Copper plated photopolymer	Yes	1.16	11	0.036	[43]
WR-06	110-170	SLM	Cu_15Sn	No	6	18.96	0.052 at 140 GHz	[53]
WR-04	170-260	CAM	Copper	No – stacked slices		30	0.054 at 215 GHz	[61]
WR-03	260-325	SLA	Copper plated photopolymer	No		12	0.016	[100]
WR-2.2	325-500	Polyjet	Copper and gold sputtered polymer	Yes		440	0.42 at 412.5 GHz	[96]

Table 5-2 compares the reported performance of several additively manufactured rectangular waveguides and their manufacturing method. The different technologies offer complementary advantages and disadvantages. Metal plating of polymers printed using stereolithography (SLA) or Polyjet [43, 96, 100] generally offer low surface roughness and high quality of metal in the outer layers, but often requires the geometries to be split in order to ensure even plating of the interior of the components. The power handling of these devices is also limited due to the low thermal conductivity and low glass transition temperature of the polymers. On the other hand, micro-dispensing of silver pastes results in high losses when used for rectangular waveguides [99] mainly due to the limited electrical conductivity of the silver pastes, and the inhomogeneity of the conductor layer [27]. Micro-dispensing is shown to be a more successful technique for planar circuits [83]. High-quality solid metal components can be fabricated using CAM [61], but the part need to be fabricated by separate slices, that are then held together using an external fixture. Technologies such as BJ [84, 85, 95] and SLM [53] are capable of

printing solid metal parts, without the need of splitting the components, but with reduced effective conductivity and surface quality. An overview of several AM technologies for microwave components is presented in [51].

Note that all-metal waveguides, such as the ones in this work, are an order of magnitude better in thermal conductivity when compared to ones made with plated plastic. As a result, they are able to handle higher power. Nevertheless, there are methods to improve power handling of plated plastic circuits, such as embedding cooling channels.

5.4. Antenna Performance

BJ is used to fabricate the horn antenna shown in Figure 5-8, which includes a standard WR-28 flange on one side, with inner dimensions of a = 7.11 mm and b = 3.57 mm as reported in [58].The length of the horn is L = 13.65 mm, and its aperture dimensions are a_1 = 8.19 mm and b_1 = 6.37 mm. As in the previously shown structures, the flange is mechanically polished. The horn antenna performance is presented in Figure 5-9, where the measured return loss and the radiation pattern show good agreement with the simulated behavior. The measured antenna gain is 8.3 dBi at 26.5 GHz.

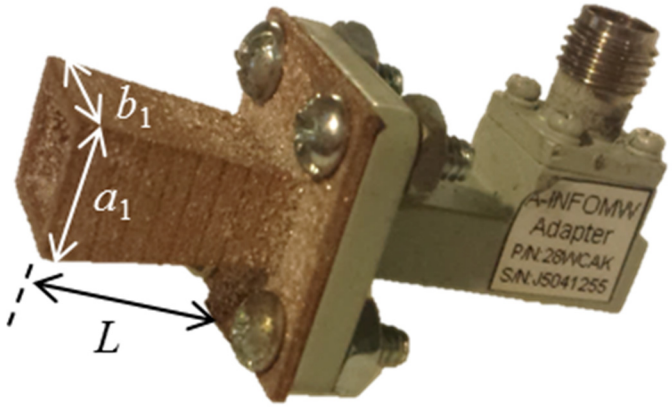

Figure 5-8: 3D-printed horn antenna connected to a WR-28 adapter.

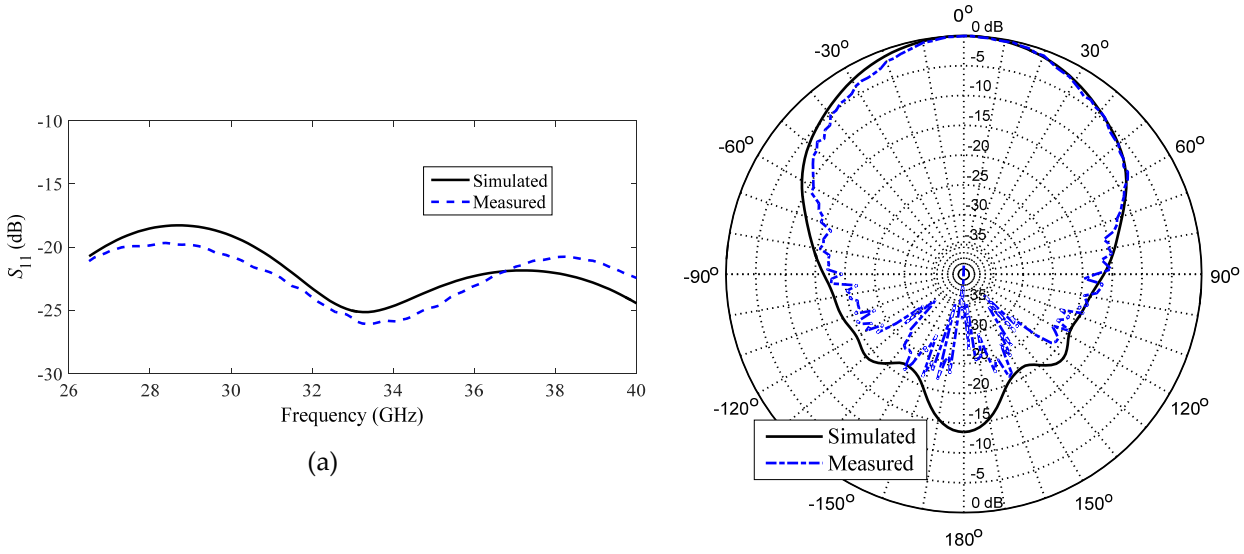

(a) (b)

Figure 5-9: Measured horn antenna parameters: (a) Magnitude of S11. (b) Radiation pattern at 26.5 GHz.

A more complicated structure, a parabolic reflector antenna, is designed using the described horn antenna, with the aim of showcasing the capabilities of BJ printing. This structure consists of a meshed parabolic reflector, a waveguide feed section with an embedded filter, and the illuminating horn antenna (Figure 5-10(a)). The goal is to print these different components as one piece, therefore, eliminating the need for joints. However, in this work, the reflector was printed separately due to printing volume limitations.

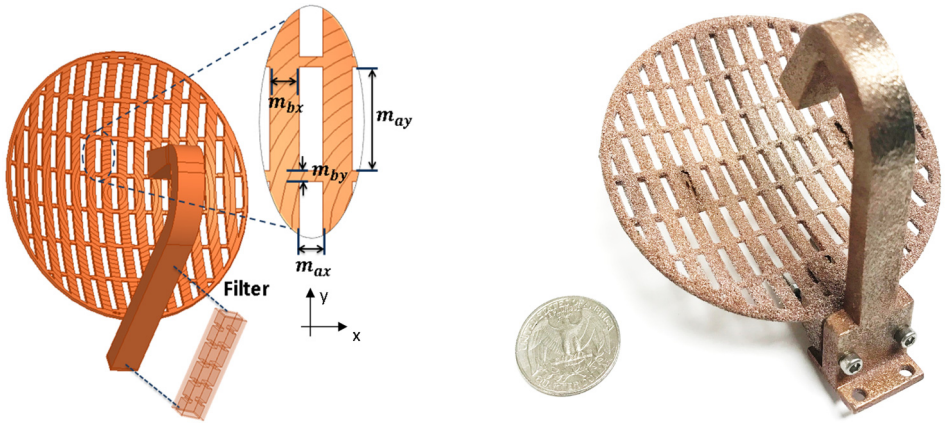

(a) (b)

Figure 5-10: Parabolic dish reflector antenna: (a) Designed structure, that includes illuminating horn, waveguide feed, filter, and meshed reflector. (b) Fabricated reflector antenna.

In the design process, the described horn antenna is used as the starting point, and the focal distance (F) is set to 38.75 mm. The radius of the parabolic reflector is optimized for maximum aperture efficiency. The maximum simulated aperture efficiency of 71.1% is obtained with a diameter (D) of 80 mm, resulting in an F/D ratio of 0.48 and a subtended angle of 56°. This angle is very close to the 10 dB beamwidth of the horn antenna. With the purpose of reducing the antenna weight, and thus the amount of required material, the reflector is meshed using a pattern depicted in Figure 5-10(a). This pattern consists of an aperture of size m_{ax} x m_{ay}, that is separated by m_{bx} in the x-direction, and by m_{by} in the y-direction. With this simple meshing, it is possible to favor the y-polarized induced currents by setting $m_{ay} > m_{ax}$ and $m_{bx} > m_{by}$. Simulations were used to optimize the structure for maximum gain and minimum cross polarization component. It was found that for the combination of m_{ax} = 2.5 mm, m_{ay} = 10 mm, m_{bx} = 3 mm, and m_{by}= 1 mm, it is possible to achieve a cross-polarization component gain of around -50 dBi, which is 20 dB less than the -30 dBi obtained with a solid reflector (at 32 GHz). The described meshed reflector also reduces the weight by around 40% when compared to the solid version. The printed reflector antenna is shown in Fig. 5-10(b). Its return loss was measured using the same setup described in Sec. 5.3 and the results are presented in Figure 5-11.

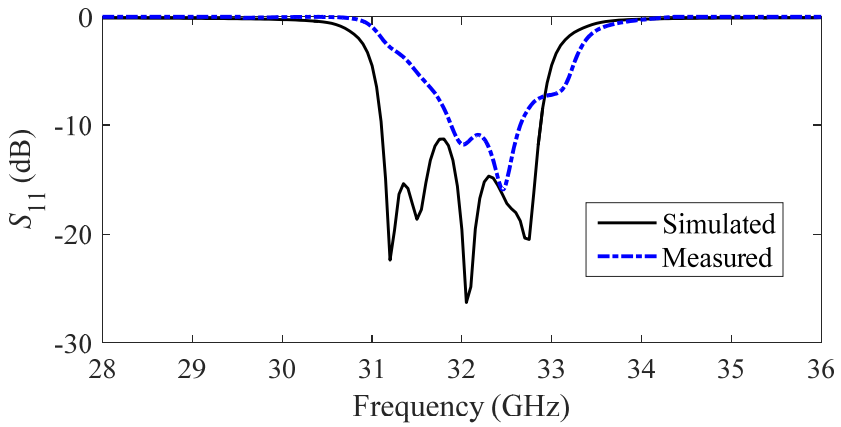

Figure 5-11: Measured and simulated S11 of the meshed parabolic reflector antenna.

The gain of the reflector antenna was measured in an anechoic chamber of dimensions 7.32 m x 3.67 m x 3.67 m, (length, width, and height, respectively) using an Orbit FR positioner system and an

8510C VNA (Fig. 5-13). Two PMI PEC-42-500M40G-20-12-292MM low noise amplifiers are also used in the setup. The behavior of the measured reflector antenna gain is shown in Fig. 5-14(a), showing a peak gain of 24.77 dBi, which is close to the values obtained from the simulations. In Fig. 5-14(b) the measured radiation pattern is depicted with the pattern obtained from simulation at 32 GHz; and the antenna parameters are listed in Table 5-3. It can be observed in Fig. 5-6, Fig. 5-11 and Fig. 5-14 that the measured response of the filter and the antenna show a frequency shift. In the case of the filter shown in Fig. 5-6, the center frequency of the pass-band shifted down by 350 MHz. The overall weight of the system shown in Fig. 5-10(b) is 112.6 g. The weight reduction due to the reflector meshing is estimated as 30 g.

Table 5-3: Reflector antenna simulated and measured parameters

	Center Freq. (GHz)	**Bandwidth (GHz)**	**Peak gain (dBi)**	**Half Power Beamwidth**
Simulated	32	1.8 (S_{11}<-10 dB)	25.25	7°
Measured	32.26	0.79 (S_{11}<-10 dB)	24.77	8.5°

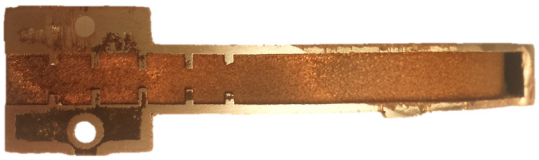

Figure 5-12: Cross-section of the filter and waveguide section of the reflector antenna.

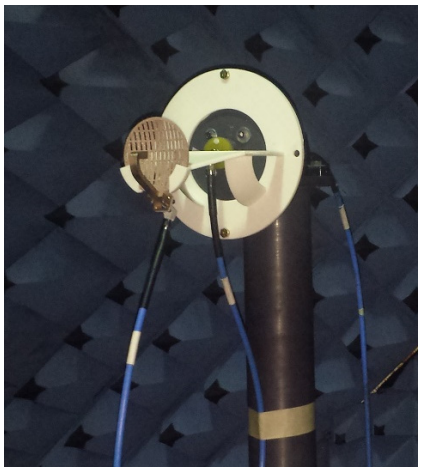

Figure 5-13: Picture of the parabolic reflector antenna inside the anechoic chamber.

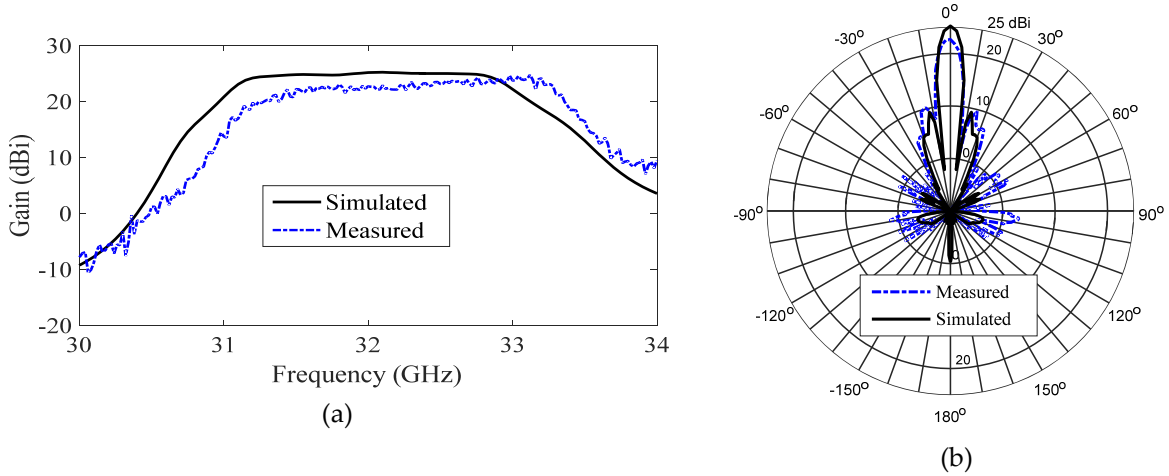

Figure 5-14: Measured and simulated parameters of the meshed parabolic reflector: (a) Gain versus frequency. (b) Radiation pattern.

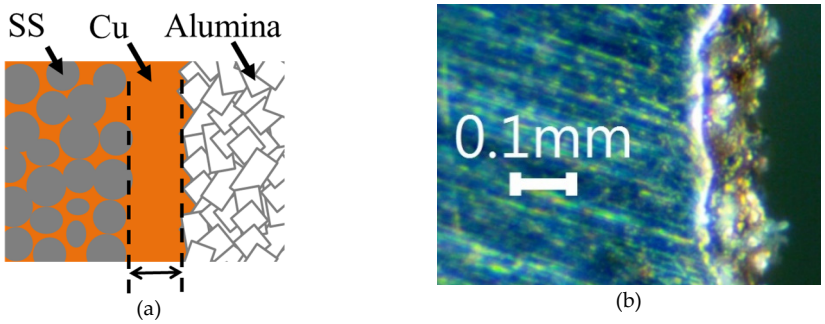

Figure 5-15: (a) Illustration of cross section of an edge of a BJ part during the infiltration process. (b) Picture of printed part where a thin layer of solid copper can be seen as a lighter region on the edge

5.5. Roughness and Tolerance Analysis

5.5.1. Effect of Roughness

The dissipative loss of metallic waveguide components is mainly driven by the DC conductivity of the metal, and its roughness. The infiltrated parts in this work show an average measured surface roughness of 6.26 μm (Ra). This roughness is generated by the nature of the infiltration process, since the infiltrant metal (Cu) wets the surface of the part and takes the profile of the green part which is encased by the supporting alumina powder. Fig. 5-15(a) illustrates this phenomenon, when the copper is in its liquid state, it is drawn into the porous green part through capillary forces, similarly to how a sponge soaks up water. The alumina support material at the outer surface creates a rough boundary to prevent

the copper from bleeding out of the green part. The resultant edge of the printed part is presented in Fig. 5-15(b), where the outer layer of copper is observed as a lighter region on the edge.

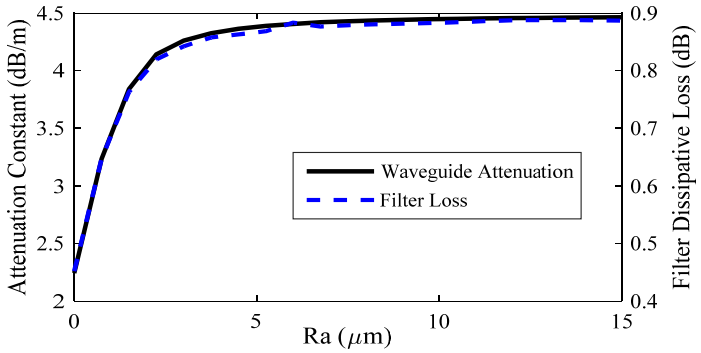

Figure 5-16: Loss prediction using the Groiss model for the waveguide and filter presented in this work, as function of the roughness (Ra) of the metal surface.

The effect of roughness in microwave components has been studied and modeled in previous works [101-106]. The typical input parameters to these models are the skin depth, the profile roughness parameters (Rq or Ra), and the type of profile. To illustrate the effect of roughness for the components in this work, the losses of the rectangular waveguide and filter are predicted using the Groiss model [103] and the results are shown in Fig. 5-16. This model accurately predicts a loss of around 4.4 dB/m, at 32 GHz, for the rectangular waveguide. It can be seen in Fig. 5-16 that the predicted loss by the Groiss model is almost independent of Ra, for values greater than 10 μm, given the frequency and electric conductivity.

The effect of roughness on the components of this work can be estimated by comparing the simulated loss of the geometries assuming smooth surfaces and finite conductivity (3.73 MS/m) with the measured performance. Table 5-4 summarizes the computed parameters for the straight waveguide section, filter, and of the entire system including the reflector.

Table 5-4: Estimation of loss generated by surface roughness.

Component	Simulated Performance - Smooth Surfaces	Measured Performance	Estimated Loss Due to Roughness
WR-28 Waveguide	2.24 dB/m	4.3 dB/m	2.06 dB/m
Passband Filter	0.45 dB at 32 GHz (Dissipative Loss)	0.71 dB at 32 GHz (Dissipative Loss)	0.26 dB
Reflector Antenna with Embedded Filter	25.79 dBi Gain at 32 GHz	22.66 dBi Gain at 32 GHz	3.13 dB

5.5.2. Dimensional Tolerances of BJ Printed Parts

The dimensional accuracy is one of the main limitations of AM which is an aspect that is continuously improving as the technology develops. Achieving low tolerance values is key for high-performance microwave circuits and antennas. The tolerances of BJ parts are dictated by four main factors: (a) resolution of the binder jetting head, (b) interaction of the binder with the metal powder once it is printed, (c) deformation of the SS matrix during sintering, and (d) wetting of the surface of the part by the infiltrant metal during the infiltration process.

There are many parameters to control during the infiltration cycle, which includes the cycle peak temperature, time at the peak temperature, heating and cooling rate, component geometry, component location, angle in the crucible, runner geometry, atmosphere type (vacuum, nitrogen, forming gas), air flow of atmospheric gas, mass of infiltrant metal, and support material properties. Fig. 5-17 shows the deviation of the measured aperture dimensions (a, b, w1, w2, w3, L1, and L2) to the 3D digital model. Fig. 5-17(a) are the results obtained for the batch where the filter was fabricated, using a peak temperature of 1200ºC for 90 min, a weight ratio of 1.15 between the weight of Cu infiltrant and the one of the part in green state. The measured average dimensional deviation of the apertures is 90 μm with a standard deviation of 43 ◎m. Fig. 5-17(b) shows the same measurement obtained from a cycle where the peak temperature was set to 1150ºC, and the weight ratio to 1.3. This part showed an average dimensional deviation of -175 ◎m with a standard deviation of 110 μm . In this case, defects inside the waveguide were observed. The parameters were modified accordingly, to avoid defects, to a peak temperature of 1150ºC and weight ratio of 1.15. Results of this process are depicted in Fig. 5-17(c), obtaining an average dimensional deviation of 4 ◎m, and a standard deviation of 46.5 μm. This correspond to the dimensions of the reflector antenna that is described in Sec. 5.4. The main contribution to these variations in tolerances are changes in the amount of copper that is covering the outer surface of the part, which is

shown in Fig. 5-15, and that is dependent on the infiltration conditions. The Cu can bleed out of the green part, over-infiltrate and generate smaller apertures, or, under-infiltrate and produce larger apertures.

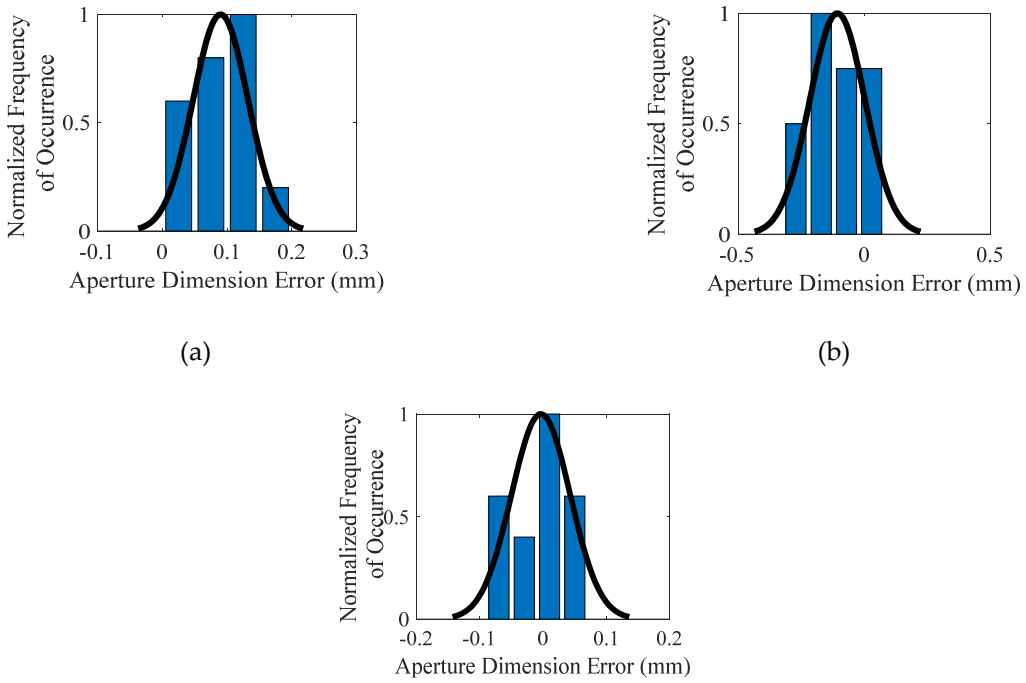

Figure 5-17: Distribution of measured dimensional error of the printed parts in three different batches. (a) Dimensional error of the filter (Fig.5- 6). (b) Dimensional error of a failed print of a reflector antenna. (c) Dimensional error of the reflector antenna.

To illustrate the effect of tolerances on performance of the components, the resonance frequency of the cavity resonator described in Sec. 5.2 are used as a figure of merit. In Fig. 5-18, the dimensions of the resonator are scaled accordingly to cover a frequency range of 17 GHz -37.5 GHz (horizontal axis). A deviation is then applied to all dimensions of the cavity, and the change in resonance frequency is computed for a tolerance range of 25 μm - 100 μm. For instance, the resonance frequency of a cavity that is smaller by 100 ◎m in each dimension would change by 1.5%, which is close to the 350 MHz frequency shift observed in the fabricated filter (Fig. 5-6). It is generally feasible to adjust the geometries for process errors in order to obtain near zero average dimensional error as seen in this iteration. Dimensional uncertainty at these sizes is driven primarily by the printing resolution discussed below.

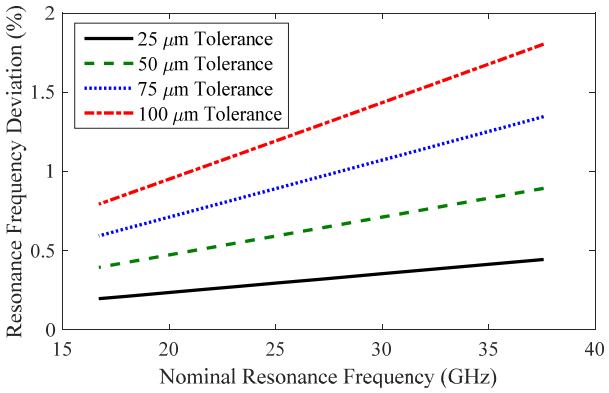

Figure 5-18: Computed frequency deviation of a rectangular cavity resonator, when all its dimensions are reduced by a given tolerance value.

5.5.3. Process Resolution

The process resolution is a function of the droplet size and powder size. Generally, smaller values improve resolution, but wetting of the droplet into the powder becomes more challenging at smaller sizes and the process may become less reliable. However, the ultimate practical limit is the ability to remove the green part from the unbound powder without damaging its features. The leading manufacturer of Binder-Jetting systems specifies a 60 μm resolution from the print head. Somewhat higher resolution is possible with finer powders and alternative printheads.

5.6. Conclusions

The 316 SS and Cu composite printed with BJ represents an option to manufacture low-loss waveguides. A resonator with an unloaded Q of 616 (at 30 GHz) and a WR-28 waveguide with attenuation of 4.3 dB/m are achieved. This technology enables the fabrication of monolithic structures, such as the antenna feed presented in this work that includes the illuminating horn, waveguide section, and filter. Such a structure is not possible to manufacture as one piece using traditional manufacturing methods.

One of the opportunities for improvement is to control and optimize the infiltration process with the aim to improve the dimensional accuracy of the parts. An alternative approach would be to perform

electroplating instead of using the infiltration process, although other challenges such as plating uniformity can arise. The surface roughness of the components could be also improved by using a finer alumina powder for the infiltration process (Fig. 5-15(a)).

It is demonstrated that this technology can be used to fabricate complex geometries, such as the meshed reflector antenna with an embedded filter. This antenna offers a lower profile option, when compared to a horn antenna with similar gain. For instance, such dish antenna could be used for satellite communications, mounted on a ground vehicle, where lower profile and durability is important.

CHAPTER 6: MESHED RECTANGULAR WAVEGUIDE

6.1. Introduction

In this chapter, a meshed rectangular waveguide is presented (Figure 6-1). With this structure, it is possible to obtain the low loss characteristic of the metallic waveguide parts, but also reduce the weight and material usage. A set of Ku-Band waveguides with different mesh dimensions are fabricated and measured, showing for instance, that it is possible to achieve a reduction of 22% in weight and material, with only 5% percent increase in the attenuation constant. In this case, the average attenuation constant across the band is 0.019 dB/cm and 0.020 dB/ cm for the solid and meshed structures, respectively. To further demonstrate the concept, a 4 pole Chebyshev bandpass filter is designed and fabricated in non-meshed and meshed waveguide versions. Results show that the meshing of the walls affects the phase constant of the waveguides, and should be accounted for in the design phase to avoid unwanted frequency shifts.

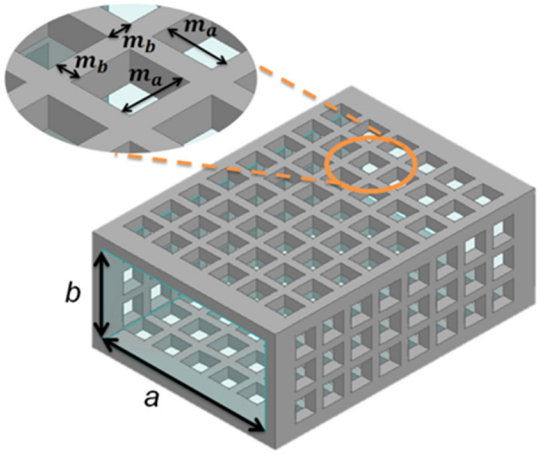

Figure 6-1: Meshed waveguide geometry.

The content of this chapter has been published [95] and it is included in this dissertation with permission from the IEEE. A copy of the permission is included in the Appendix A.

6.2. Design

Simulations of the structure shown in Figure 6-1 are performed using Ansys Electronic Desktop 2016.2, to understand the effect of the meshing of the walls, and are shown in Figure 6-2. The marked data points are the simulated combinations of the dimensions m_a and m_b, which are a swept in the range of 0.5-2 mm. Note that both the attenuation constant and phase constant are affected by the meshing of the walls. In Figure 6-2(a) it is possible to appreciate that the attenuation constant has very low dependence on the dimension of m_b for aperture sizes (m_a) that are below 1 mm, which is around 4% of the guided wavelength.

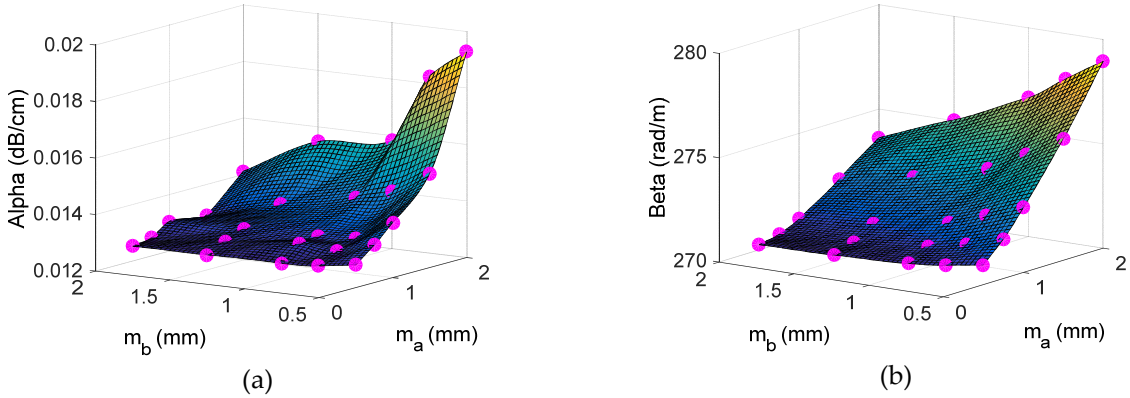

Figure 6-2: Simulated propagation constant of the WR-62 waveguide as a function of the mesh dimensions. (a) Attenuation constant. (b) Phase constant.

In order to explore the measured the effect that the meshing of the walls has on the performance of the rectangular waveguide, a set of Ku-band (WR-62) rectangular waveguides are fabricated. Since the mesh is a bivariate structure, a reference meshed waveguide (M1) of m_a= 1.44 mm, and m_b= 1.56 mm is 3D modeled. Two variations, one keeping the gap size relatively constant, but decreasing m_b (M2), and the second one keeping m_b constant but increasing m_a (M3) are also designed. As a reference parameter, the density of the waveguides represents the ratio between the volume of the meshed structure (and therefore, the weight) and the solid version (excluding the flanges), and can be approximated using (6.1). The dimensions of these waveguides are detailed in Table 6-1. In this case, M2 and M3 have similar densities. The lengths of the waveguides is 25.26 mm.

$$D = \frac{(m_a + m_b)^2 - {m_a}^2}{(m_a + m_b)^2} \tag{6.1}$$

To further demonstrate the effect of the meshed structure, a 4 pole Chebyshev cavity filter is designed at a center frequency of 16.5 GHz, and a bandwidth of 700 MHz. The walls of this filter were meshed using the dimensions of m_a= 2.1 mm and m_b= 0.6 mm, for a final density of ~60%. These filters have irises that are 2 mm thick, and a total length of 63.7 mm.

6.3. Fabrication

The fabrication process is similar to the one described in Sec. 6.2.1. The waveguides and filters are fabricated with an Exone Innovent printer. This machine uses a metal binder jetting additive manufacturing process. An inkjet-like print head is used to deposit binder onto a bed covered with 4-20 stainless steel powder with particles 30 μm in diameter on average. Once the desired 2D cross section of the part is printed, the binder is partially dried with an infrared heat lamp. A new layer of metal powder is then deposited on top of the first, and the process repeats until the part is recreated. The entire powder bed is placed in a convection oven for 4 h at 185 ºC to finish curing the binder.

The resulting green part is then infiltrated to reduce the porosity. For infiltration, the part is removed from the powder bed and packed into a crucible along with the copper powder. The part is placed in a high-temperature oven, and the internal temperature is brought to 1120 ºC during a 24 h cycle. This causes all of the binder to burn off while sintering together the stainless steel powder and melting the copper. The molten copper powder, which is in contact with the part infiltrates into the matrix by capillary forces. This creates an interconnected stainless steel structure in a copper matrix. The part is then cooled and removed from the crucible. Typically, the roughness of a binder jetted 3D part is greater than that of a part created by conventional machining. Figure 6-3 shows the pictures of the meshed walls of the fabricated waveguides. It is possible to observe some residues of the alumina powder used to surround the parts to ensure proper heat distribution during the infiltration cycle.

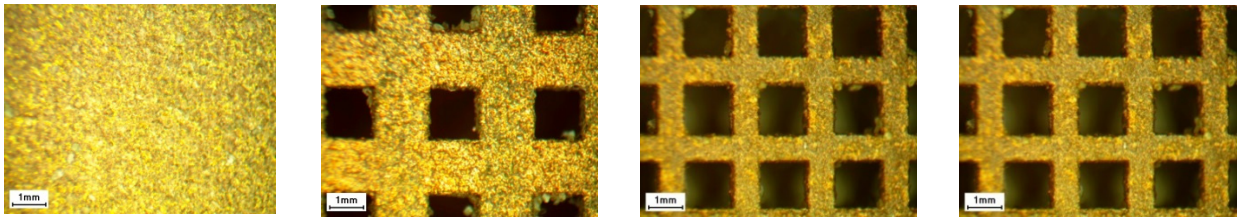

(a) (b) (c) (d)

Figure 6-3: Pictures of walls of fabricated waveguides. (a) Solid. (b) M1. (c) M2. (d) M3.

6.4. Results

The conductivity of the 3D printed metals was measured using the Van der Pauw method, obtaining values of 0.57 MS/m for the sintered stainless steel parts and 3.73 MS/m for the Cu infiltrated stainless steel. Also, the roughness of the printed Cu + stainless steel alloy was measured using a Dektak 150 surface profiler, obtaining a *Ra* value of 6.26 μm. Subsequently, the S-parameters of the printed waveguides were measured using a Keysight PNA N5227A, calibrated with a Maury P7005E calibration kit. The responses are shown Figure 6-4. The simulated S11 of the solid waveguide is ~70 dB across the band and is not included in Figure 6-4a). The average attenuation constant over the frequency band (α), and the phase constant at 15 GHz (β) are summarize in Table 6-1. For a reduction of 22% in density for M1, the loss increases by 5%. In the case of M2, which is 39% lighter than the solid counterpart, the loss increases by 32%. The measurements also suggest that the phase constant increases as the value of the opening m_a increases.

Table 6-1: Propagation characteristics

Line	α (dB/cm)	β (rad/m) @ 15 GHz	Density (Vol_{mesh}/Vol_{solid})
Solid – Simulation	0.0134	243.63	1
Solid – Measured	0.019	245.56	1
M1 m_a= 1.44 mm m_b= 1.56 mm	0.020	247.96	0.78
M2 m_a= 1.46 mm m_b= 0.73 mm	0.025	249.50	0.61
M3 m_a= 2.67 mm m_b= 1.47 mm	0.029	253.63	0.65

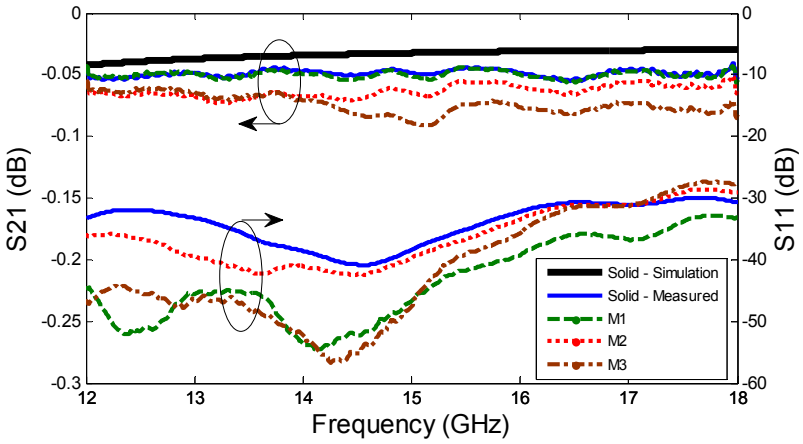

(a)

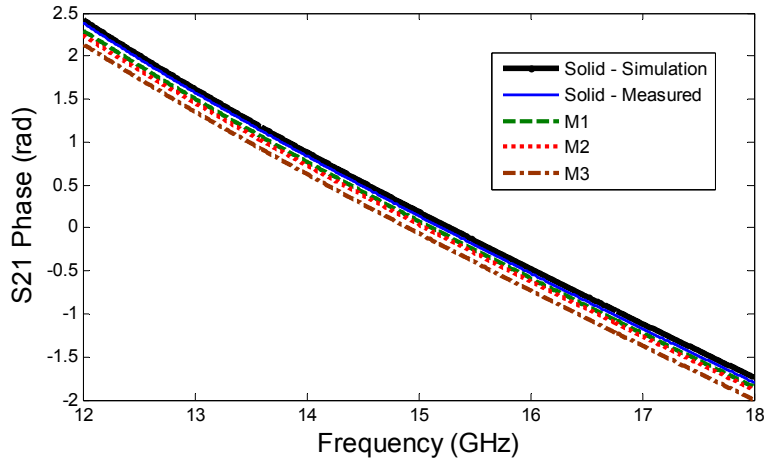

(b)

Figure 6-4: Simulated and measured S-parameters of non-meshed (solid) and meshed (M1, M2, and M3) waveguides. (a) Transmission and reflection coefficients. (b) Phase of transmission coefficient.

Figure 6-5 shows the propagation constant of the fabricated samples, and compares it to the expected values from simulation, as a function of density (D). Note that the behavior of the propagation constant is not monotonic, and that the line with larger losses is also the one that has the largest mesh opening (m_a= 2.67 mm). To track the source of this loss, the radiation loss of the three designs (M1, M2, and M3) are extracted from simulations, by substracting the loss of the structure when setting the corresponding surface roughness and DC conductivity, and the loss when setting the walls to be a perfect electric conductor. No evidence of radiation loss was found for M1 and M2, whereas M3 showed a value of 0.009 dB/cm (at 15 GHz) due to radiation.

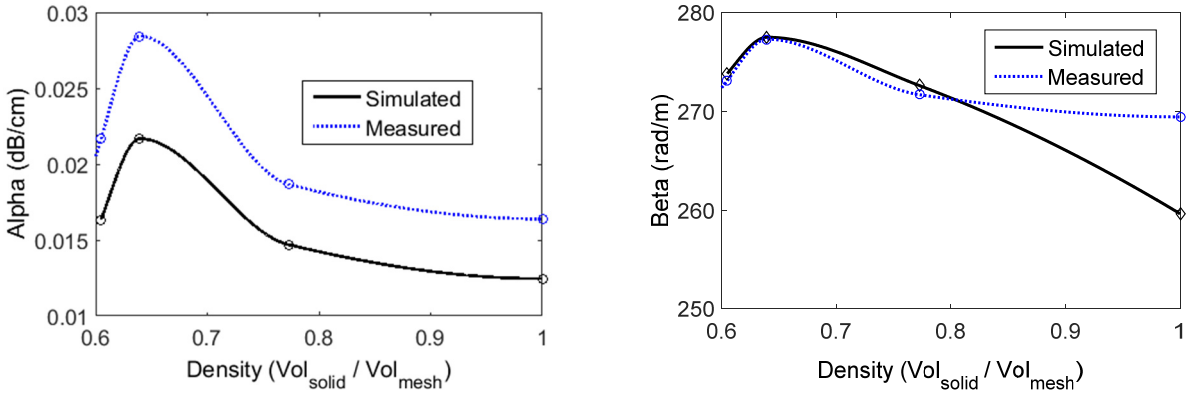

(a) (b)

Figure 6-5: Extracted attenuation and phase constants for the manufactured waveguides.

For the manufactured filters, the measured responses are shown in Figure 6-6(b) and the performance parameters summarized in Table 6-2. The center frequency and bandwidth deviate from the design values mainly due to tolerances in the 3D printing process that in this case are ~50 um. On the other hand, the center frequency of the meshed design shifted down by ~160 MHz due to the fact that the meshed walls increase the phase constant of the structure, therefore, lowering the resonance frequency of the cavities. Due to this shifting, both the return loss and the insertion loss are degraded, since the coupling iris were designed for the ideal center frequency. In order to make a fair comparison, the maximum available gain of the filter is calculated, and the resulting values are -0.981 dB for the solid wall filter, and -0.858 dB for the meshed version. This means that the mesh itself has little impact on the loss in the structure.

Table 6-2: Filter performance.

	Filter	f_0 (GHz)	3 dB BW (GHz)	Min. IL (dB)	Max. RL (dB)
Simulated	Solid	16.52	0.69	0.84	35
	Meshed m_a= 1.8 mm m_b= 1 mm	16.35	0.67	1.23	27
Measured	Solid	16.13	0.59	1.15	14.2
	Meshed m_a= 2.17 mm m_b= 0.63 mm Density= 0.59	15.91	0.62	1.59	8.11

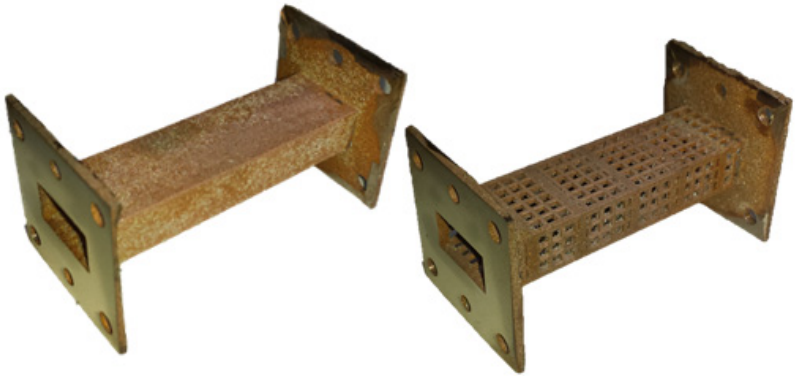

(a)

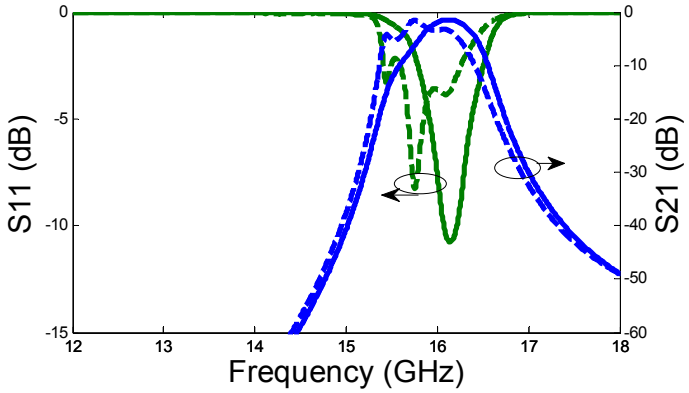

(b)

Figure 6-6: (a) Fabricated filters (solid and meshed). (b) Measured response of the filters.

6.5. Conclusions

In this chapter, the meshed rectangular waveguide is presented, and it is shown that compared to a standard, non-meshed design it is possible to reduce weight with minimal effect on the high-frequency performance. For instance, the average attenuation constant increases from 0.019 dB/cm to only 0.020 dB/cm when using a mesh that reduces the weight by ~20%. However, meshing the waveguide does produce an increase in the phase constant, and this is important in designing components such as filters and couplers. The response of the filters confirmed that the change in the phase constant of the structure needs to be accounted for in the design stage. The computed maximum available gain reveals that the mesh has minimal effect on the loss in the cavities.

CHAPTER 7: SUMMARY AND RECOMMENDATIONS

7.1. Summary

This work is focused on two aspects of AM: (a) The development and characterization of techniques to digitally manufacture microwave and millimeter-wave circuits and antennas, and (b) proposing and studying meshed geometries to achieve a reduction in material usage on planar circuits or weight for metallic waveguides. For the planar circuits, direct print additive manufacturing (DPAM), also known as micro-dispensing, is extensively used to print silver paste (CB028) on dielectrics. The major limitations of this technology are discussed, which include high dissipative losses and minimum feature sizes of around ~100 μm. It was discovered that by using picosecond laser machining, both major limitations are addressed. By using the laser, 16 μm wide slots are achieved over a 25 μm thick CB028, which effectively takes the practical upper-frequency limit of the CPW transmission lines in this work to 40 GHz. It was found that the laser solidifies the walls of the slots in an area that is ~2 μm wide (for the conditions used in this work), which reduces the loss of the structure by around 50%, when compared with the ones obtained using only micro-dispensing. This improvement translates to an increase of 100x in effective conductivity of the silver paste layer, and the losses of the 3D printed CPW lines are comparable to the ones obtained from state of the art traditional techniques, such as photolithography of copper-clad liquid crystal polymer (LCP). The laser machining effects are further verified by performing FEM simulations, and by developing an analytical method based on conformal mapping.

The other AM technology that is characterized in this work is binder jetting (BJ), which is used to 3D print solid metal parts, that result in a composite of stainless steel and copper. Its Ka-Band performance is benchmarked using a cavity resonator, straight waveguide sections, a cavity filter, and a

horn antenna. It is found that this technology is an option for high power applications, since it is made out of solid metal, and the average dissipative loss in the range of 26-40 GHz is 4.3 dB/m. The capabilities of this technology are demonstrated by fabricating a monolithic meshed parabolic reflector antenna that integrates a filter, waveguide sections, illumination horn, and the reflector in two pieces. Among the limitations of this technology are the surface roughness and the dimensional accuracy of the printed parts.

The second main focus of this dissertation is on meshed geometries. For planar microwave circuits, the use of meshed ground coplanar waveguide (MGCPW) is characterized. The study includes both, CPW lines fabricated using 3D printing, and using traditional photolithography. The 3D printed lines are fabricated using micro-dispensing of silver paste (CB028). Results show that for reduction of silver paste usage, meshing the ground conductor is a better method, when compared to reducing its size using the finite ground approach. The results also suggest that a mesh density of ~50% is the best condition for reduction of silver ink usage, while having minimal effect on the dissipative losses. A physical-mathematical model, based on conformal mapping, is developed as a tool to estimate the capacitance per unit length, and the characteristic impedance of the line, of a given MGCPW geometry, without the need to perform FEM simulations of the entire structure.

Finally, it is shown that meshing the walls of rectangular waveguides represents an alternative to reduce the weight, while maintaining the performance and high-power capability of the structure. This premise is tested by measuring the performance of 3D printed meshed Ku-Band waveguides. BJ is used to fabricate the parts, and the characterization is based on S-parameters. It was found, for instance, that if the mesh opening size is less than 4% of the guided wavelength, the loss of the structure is minimally affected, while achieving weight reductions of around 50%.

7.2. Recommendations

The degrees of freedom that digital manufacturing enables are generating countless opportunities in the field of microwave and mm-wave circuits and antennas. In this section, some of this opportunities are listed as motivation for future work.

a) It has been shown that picosecond laser machining is a valuable technique to improve the performance of 3D printed CPW. Considerable room for improvement can be found in this technique, including the optimization of the optics within the laser to achieve spots sizes of the order of 3 μm, which is around the theoretical limit given the characteristics of the laser used in this work. This level of resolution would enable the 3D printing of CPW well into the sub-THz frequency range.

b) The AM techniques presented in this dissertation are capable of fabricating 3D structures with embedded conformal circuits in ways that are not possible when using traditional manufacturing. Further research efforts need to be directed towards effectively fabricating functional structures with integrated microwave and millimeter wave circuits and antennas, as a single piece.

c) Considerable advances in material development have been recently reported, achieving materials with losses that are better than state of the art commercial laminates. Different models predict that there is room for further improvement, showing that it is theoretically possible to achieve low-loss substrates with relative permittivity values greater than 20. Different challenges need to be addressed to make such materials 3D printable. Magnetic 3D printable material is also an area where development is still in the early stages.

d) In this work it is shown that meshing represents a great technique for not only reduction of material usage and weight; but it can also provide advantages in functionality such as in the reflector antenna. The meshes presented in this dissertation have rectangular shape. Works

needs to be done to explore the optimal meshing approach to achieve a performance improvement.

REFERENCES

[1] M. Ruffo, C. Tuck, and R. Hague, "Cost estimation for rapid manufacturing - laser sintering production for low to medium volumes," *Proceedings of the Institution of Mechanical Engineers, Part B: Journal of Engineering Manufacture,* vol. 220, pp. 1417-1427, 2006.

[2] M. K. Thompson, G. Moroni, T. Vaneker, G. Fadel, R. I. Campbell, I. Gibson, *et al.*, "Design for Additive Manufacturing: Trends, opportunities, considerations, and constraints," *CIRP Annals - Manufacturing Technology,* vol. 65, pp. 737-760, // 2016.

[3] N. Hopkinson and P. Dicknes, "Analysis of rapid manufacturing—using layer manufacturing processes for production," *Proceedings of the Institution of Mechanical Engineers, Part C: Journal of Mechanical Engineering Science,* vol. 217, pp. 31-39, 2003.

[4] "Fit to Print: New Plant Will Assemble World's First Passenger Jet Engine With 3D Printed Fuel Nozzles, Next-Gen Materials," in *GE Report*, ed. http://www.gereports.com/post/91763815095/worlds-first-plant-to-print-jet-engine-nozzles-in/ General Electric, 2014.

[5] W. T., "Wohlers Report 2015: Global Reports.," Wohlers Associates, Belgium 2015.

[6] S. Zistl, "3D Printing: Facts & Forecasts," Siemens, 2014.

[7] J. Castro, E. Rojas, T. Weller, and J. Wang, "High-k and low-loss polymer composites with co-fired Nd and Mg-Ca titanates for 3D RF and microwave printed devices: Fabrication and characterization," in *2015 IEEE 16th Annual Wireless and Microwave Technology Conference (WAMICON)*, 2015, pp. 1-5.

[8] J. Castro, E. Rojas, A. Ross, T. Weller, and J. Wang, "High-k and low-loss thermoplastic composites for Fused Deposition Modeling and their application to 3D-printed Ku-band antennas," in *2016 IEEE MTT-S International Microwave Symposium (IMS)*, 2016, pp. 1-4.

[9] M. M. Abdin, J. Castro, J. Wang, and T. Weller, "Miniaturized 3D printed balun using high-k composites," in *2015 IEEE 16th Annual Wireless and Microwave Technology Conference (WAMICON)*, 2015, pp. 1-3.

[10] J. Castro, E. Rojas, T. Weller, and J. Wang, "Engineered Nanocomposites for Additive Manufacturing of Microwave Electronics," *International Symposium on Microelectronics,* vol. 2015, pp. 000189-000196, 2015.

[11] J. Castro, E. A. Rojas-Nastrucci, A. Ross, T. M. Weller, and J. Wang, "Fabrication, Modeling, and Application of Ceramic-Thermoplastic Composites for Fused Deposition Modeling of Microwave Components," *IEEE Transactions on Microwave Theory and Techniques,* vol. PP, pp. 1-12, 2017.

[12] J. Castro, E. Rojas, T. Weller, and J. Wang, "High-Permittivity and Low-Loss Electromagnetic Composites Based on Co-fired Ba0.55Sr0.45TiO3 or MgCaTiO2 Microfillers for Additive Manufacturing and Their Application to 3-D Printed K-Band Antennas," *Journal of Microelectronics and Electronic Packaging,* vol. 13, pp. 102-112, 2016.

[13] B. K. Tehrani, B. S. Cook, and M. M. Tentzeris, "Inkjet-printed 3D interconnects for millimeter-wave system-on-package solutions," in *2016 IEEE MTT-S International Microwave Symposium (IMS)*, 2016, pp. 1-4.

[14] W. Su, B. S. Cook, and M. M. Tentzeris, "Additively Manufactured Microfluidics-Based "Peel-and-Replace" RF Sensors for Wearable Applications," *IEEE Transactions on Microwave Theory and Techniques*, vol. 64, pp. 1928-1936, 2016.

[15] C. Mariotti, F. Alimenti, L. Roselli, and M. M. Tentzeris, "High-Performance RF Devices and Components on Flexible Cellulose Substrate by Vertically Integrated Additive Manufacturing Technologies," *IEEE Trans. Microw. Theory Techn.*, vol. 65 No. 1, pp. 1-10, Jan. 2017.

[16] S. Kim, A. Shamim, A. Georgiadis, H. Aubert, and M. M. Tentzeris, "Fabrication of Fully Inkjet-Printed Vias and SIW Structures on Thick Polymer Substrates," *IEEE Transactions on Components, Packaging and Manufacturing Technology*, vol. 6, pp. 486-496, 2016.

[17] F. Cai, Y. H. Chang, K. Wang, C. Zhang, B. Wang, and J. Papapolymerou, "Low-Loss 3-D Multilayer Transmission Lines and Interconnects Fabricated by Additive Manufacturing Technologies," *IEEE Trans. Microw. Theory Techn.*, vol. 64, No. 10, pp. 3208-3216, Oct. 2016.

[18] C. Fan, S. Pavlidis, J. Papapolymerou, C. Yung Hang, W. Kan, C. Zhang, *et al.*, "Aerosol jet printing for 3-D multilayer passive microwave circuitry," in *Microwave Conference (EuMC), 2014 44th European*, 2014, pp. 512-515.

[19] C. Fan, C. Yung-Hang, W. Kan, W. T. Khan, S. Pavlidis, and J. Papapolymerou, "High resolution aerosol jet printing of D- band printed transmission lines on flexible LCP substrate," in *2014 IEEE MTT-S International Microwave Symposium (IMS)*, 2014, pp. 1-3.

[20] M. Liang, Y. Xiaoju, C. Shemelya, E. MacDonald, and H. Xin, "3D printed multilayer microstrip line structure with vertical transition toward integrated systems," in *2015 IEEE MTT-S Int. Microw. Symp.*, Phoenix, AZ, 2015, pp. 1-4.

[21] M. Liang, C. Shemelya, E. MacDonald, R. Wicker, and H. Xin, "3-D Printed Microwave Patch Antenna via Fused Deposition Method and Ultrasonic Wire Mesh Embedding Technique," *Antennas and Wireless Propagation Letters, IEEE*, vol. 14, pp. 1346-1349, 2015.

[22] I. T. Nassar, T. M. Weller, and H. Tsang, "3-D printed antenna arrays for harmonic radar applications," in *WAMICON 2014*, 2014, pp. 1-4.

[23] I. T. Nassar and T. M. Weller, "An electrically-small, 3-D cube antenna fabricated with additive manufacturing," in *2013 IEEE Topical Conference on Biomedical Wireless Technologies, Networks, and Sensing Systems*, 2013, pp. 85-87.

[24] I. T. Nassar, T. M. Weller, and H. Tsang, "A 3-D printed miniaturized log-periodic dipole antenna," in *Antennas and Propagation Society International Symposium (APSURSI), 2014 IEEE*, 2014, pp. 11-12.

[25] D. Hawatmeh, E. Rojas-Nastrucci, and T. Weller, "A multi-material 3D printing approach for conformal microwave antennas," in *2016 International Workshop on Antenna Technology (iWAT)*, 2016, pp. 7-10.

[26] J. O. Brien, M. F. Córdoba-Erazo, E. Rojas, J. Castro, M. Abdin, G. Mumcu, *et al.*, "Miniaturization of microwave components and antennas using 3D manufacturing," in *2015 9th European Conference on Antennas and Propagation (EuCAP)*, 2015, pp. 1-4.

[27] T. P. Ketterl, "A 2.45 GHz Phased Array Antenna Unit Cell Fabricated Using 3-D Multi-Layer Direct Digital Manufacturing," *IEEE Trans. Microw. Theory Techn.*, vol. 63, No. 12, pp. 4382-4394, Dec. 2015.

[28] P. I. Deffenbaugh, T. M. Weller, and K. H. Church, "Fabrication and Microwave Characterization of 3-D Printed Transmission Lines," *IEEE Microw. Wireless Compon. Lett.*, vol. 25, No. 12, pp. 823-825, Dec. 2015.

[29] M. S. Mirotznik, Z. Larimore, P. Pa, P. Parsons, and M. Mills, "Multi-material additive manufacturing of antennas," in *2016 International Workshop on Antenna Technology (iWAT)*, 2016, pp. 123-126.

[30] R. Ramirez, E. Rojas-Nastrucci, and T. Weller, "UHF RFID Tags for On/Off-Metal Applications Fabricated using Additive Manufacturing," *IEEE Antennas and Wireless Propagation Letters,* vol. PP, pp. 1-1, 2017.

[31] E. A. Rojas-Nastrucci, T. Weller, V. Lopez Aida, C. Fan, and J. Papapolymerou, "A study on 3D-printed coplanar waveguide with meshed and finite ground planes," in *Wireless and Microwave Technology Conference (WAMICON), 2014 IEEE 15th Annual*, 2014, pp. 1-3.

[32] R. A. Ramirez, E. A. Rojas-Nastrucci, and T. M. Weller, "3D tag with improved read range for UHF RFID applications using Additive Manufacturing," in *Wireless and Microwave Technology Conference (WAMICON), 2015 IEEE 16th Annual*, 2015, pp. 1-4.

[33] Jonathan M. O'Brien, E. Rojas, and Thomas M. Weller, "A Switched-Line Phase Shifter Fabricated with Additive Manufacturing," *International Symposium on Microelectronics,* vol. 2013, pp. 000909-000913, 2013.

[34] T. Merkle, R. Gotzen, C. Joo-Young, and S. Koch, "Polymer Multichip Module Process Using 3-D Printing Technologies for D-Band Applications," *IEEE Trans. Microw. Theory Techn.*, vol. 63, No. 2, pp. 481-493, Feb. 2015.

[35] E. A. Rojas-Nastrucci, A. D. Snider, and T. M. Weller, "Propagation Characteristics and Modeling of Meshed Ground Coplanar Waveguide," *IEEE Transactions on Microwave Theory and Techniques,* vol. 64, No. 11, pp. 3460-3468, Nov. 2016.

[36] P. I. Deffenbaugh, "3D Printed Electromagnetic Transmission and Electronic Structures Fabricated on a Single Platform using Advanced Process Integration Techniques," The University of Texas at El Paso, 2014.

[37] G. van den Broek, "On the reflection properties of periodically supported metallic wire gratings with rectangular mesh showing small sag," *Antennas and Propagation, IEEE Transactions on,* vol. 19, pp. 109-113, 1971.

[38] A. Miura and Y. Rahmat-Samii, "Spaceborne Mesh Reflector Antennas With Complex Weaves: Extended PO/Periodic-MoM Analysis," *Antennas and Propagation, IEEE Transactions on,* vol. 55, pp. 1022-1029, 2007.

[39] B. J. Rubin, "The Propagation Characteristics of Signal Lines in a Mesh-Plane Environment," *Microwave Theory and Techniques, IEEE Transactions on,* vol. 32, pp. 522-531, 1984.

[40] C. Chung-Ping, A. F. Burnett, J. M. Cech, and M. H. Tanielian, "The signal transmission characteristics of embedded microstrip transmission lines over a meshed ground plane in copper/polyimide multichip module," *Components, Packaging, and Manufacturing Technology, Part B: Advanced Packaging, IEEE Transactions on,* vol. 17, pp. 578-583, 1994.

[41] W. Muh-Dey and R. Negra, "Low-loss mesh-type coplanar waveguides for high-current, high-frequency CMOS circuits," in *Microwave Conference (GeMiC), 2015 German*, 2015, pp. 319-322.

[42] K. Jun-Goo, L. Eun-Tae, K. Dong-Hoon, L. Jong-Hun, L. Sun-Young, K. Hyeong-Seok, *et al.*, "Analysis of coupling characteristics between transmission lines with a buried meshed-ground in LTCC-MCMs," in *Microwave Symposium Digest, 2002 IEEE MTT-S International*, 2002, pp. 825-828 vol.2.

[43] M. D'Auria, W. J. Otter, J. Hazell, B. T. W. Gillatt, C. Long-Collins, N. M. Ridler, *et al.*, "3-D Printed Metal-Pipe Rectangular Waveguides," *IEEE Trans. Compon., Hybrids, Manuf. Technol.*, vol. 5 No. 9, pp. 1339-1349, Sept. 2015.

[44] O. S. Kim, "Rapid Prototyping of Electrically Small Spherical Wire Antennas," *IEEE Transactions on Antennas and Propagation,* vol. 62, pp. 3839-3842, 2014.

[45] O. S. Kim, "3D printing electrically small spherical antennas," in *2013 IEEE Antennas and Propagation Society International Symposium (APSURSI)*, 2013, pp. 776-777.

[46] P. T. Timbie, J. Grade, D. v. d. Weide, B. Maffei, and G. Pisano, "Stereolithographed MM-wave corrugated horn antennas," in *Infrared, Millimeter and Terahertz Waves (IRMMW-THz), 2011 36th International Conference on*, 2011, pp. 1-3.

[47] E. G. Geterud, P. Bergmark, and Y. Jian, "Lightweight waveguide and antenna components using plating on plastics," in *Antennas and Propagation (EuCAP), 2013 7th European Conference on*, 2013, pp. 1812-1815.

[48] L. Schulwitz and A. Mortazawi, "A compact millimeter-wave horn antenna array fabricated through layer-by-layer stereolithography," in *2008 IEEE Antennas and Propagation Society International Symposium*, 2008, pp. 1-4.

[49] C. Fan, W. T. Khan, and J. Papapolymerou, "A low loss X-band filter using 3-D Polyjet technology," in *Microwave Symposium (IMS), 2015 IEEE MTT-S International*, 2015, pp. 1-4.

[50] L. Bosui, G. Xun, and W. J. Chappell, "Applications of layer-by-layer polymer stereolithography for three-dimensional high-frequency components," *IEEE Transactions on Microwave Theory and Techniques*, vol. 52, pp. 2567-2575, 2004.

[51] R. Sorrentino and O. A. Peverini, "Additive manufacturing: a key enabling technology for next-generation microwave and millimeter-wave systems [point of view]," *Proc. IEEE*, vol. 104, pp. 1362-1366, 2016.

[52] O. A. Peverini, M. Lumia, F. Calignano, G. Addamo, M. Lorusso, E. P. Ambrosio, *et al.*, "Selective Laser Melting Manufacturing of Microwave Waveguide Devices," *Proc. IEEE*, vol. 105, pp. 620-631, Apr. 2017.

[53] B. Zhang and H. Zirath, "Metallic 3-D Printed Rectangular Waveguides for Millimeter-Wave Applications," *IEEE Trans. Compon. Packag. Manuf. Technol.*, vol. 6 No. 5, pp. 796-804, May 2016.

[54] B. Zhang and H. Zirath, "A Metallic 3-D Printed E-Band Radio Front End," *IEEE Microw. Wireless Compon. Lett.*, vol. 26 No. 5, pp. 331-333, May 2016.

[55] B. Zhang and e. al., "Metallic 3-D Printed Antennas for Millimeter- and Submillimeter Wave Applications," *IEEE Trans. THz Sci. Technol.*, vol. 6 No. 4, pp. 592-600, Jul. 2016.

[56] J. A. Lorente, M. M. Mendoza, A. Z. Petersson, L. Pambaguian, A. A. Melcon, and C. Ernst, "Single part microwave filters made from selective laser melting," in *2009 European Microwave Conference (EuMC)*, Rome, 2009, pp. 1421-1424.

[57] G. L. Huang, S. G. Zhou, and T. H. Chio, "A compact wideband 16-way power combiner implemented via 3-D metal printing," in *2016 IEEE 5th Asia-Pacific Conference on Antennas and Propagation (APCAP)*, 2016, pp. 51-52.

[58] E. A. Rojas-Nastrucci, J. Nussbaum, T. M. Weller, and N. B. Crane, "Metallic 3D Printed Ka-Band Pyramidal Horn using Binder Jetting," presented at the IEEE Latin America Microwave Conference 2016, Pto. Vallarta, MEX, 2016.

[59] C. R. Garcia, R. C. Rumpf, H. H. Tsang, and J. H. Barton, "Effects of extreme surface roughness on 3D printed horn antenna," *Electronics Letters*, vol. 49, pp. 734-736, 2013.

[60] H. Kazemi, D. Miller, A. Mohan, Z. Griffith, Y. Jin, J. Kwiatkowski, *et al.*, "350mW G-band medium power amplifier fabricated through a new method of 3D-copper additive manufacturing," in *2015 IEEE MTT-S International Microwave Symposium*, 2015, pp. 1-3.

[61] H. Kazemi, D. Miller, A. Mohan, Y. Jin, M. Crawford, M. Wagenseil, *et al.*, "Ultra-compact G-band 16way power splitter/combiner module fabricated through a new method of 3D-copper additive manufacturing," in *2015 IEEE MTT-S Int. Microw. Symp.*, Phoenix, AZ, 2015, pp. 1-3.

[62] C. Guo, X. Shang, J. Li, F. Zhang, M. J. Lancaster, and J. Xu, "A Lightweight 3-D Printed X-Band Bandpass Filter Based on Spherical Dual-Mode Resonators," *IEEE Microw. Compon. Lett.*, vol. 26, pp. 568-570, 2016.

[63] L. Aida Garcia, E. E. L. C, R. Chandra, and A. J. Johansson, "Optimization and fabrication by 3D printing of a volcano smoke antenna for UWB applications," in *2013 7th European Conference on Antennas and Propagation (EuCAP)*, 2013, pp. 1471-1473.

[64] K. F. Brakora, J. Halloran, and K. Sarabandi, "Design of 3-D Monolithic MMW Antennas Using Ceramic Stereolithography," *IEEE Transactions on Antennas and Propagation,* vol. 55, pp. 790-797, 2007.

[65] M. F. Shafique and I. D. Robertson, "Rapid prototyping of LTCC microwave circuits using laser machining," in *2009 IEEE MTT-S International Microwave Symposium Digest*, 2009, pp. 469-472.

[66] D. M. Nair, W. E. McKinzie, B. A. Thrasher, M. A. Smith, E. D. Hughes, and J. M. Parisi, "A 10 MHz to 100 GHz LTCC CPW-to-stripline vertical transition," in *2013 IEEE MTT-S International Microwave Symposium Digest (IMS)*, 2013, pp. 1-4.

[67] L. Zhaolong and W. Ke, "24-GHz Frequency-Modulation Continuous-Wave Radar Front-End System-on-Substrate," *IEEE Transactions on Microwave Theory and Techniques,* vol. 56, No. 2, pp. 278-285, 2008.

[68] R. C. Y. Auyeung, M. W. Nurnberger, D. J. Wendland, A. Pique, C. B. Arnold, A. R. Abbott, *et al.*, "Laser fabrication of GPS conformal antennas," in *Photon Processing in Microelectronics and Photonics III*, 2004, pp. 292-297.

[69] D.-Y. Shin, S.-S. Yoo, H.-e. Song, H. Tak, and D. Byun, "Electrostatic-Force-Assisted Dispensing Printing to Construct High-Aspect-Ratio of 0.79 Electrodes on a Textured Surface with Improved Adhesion and Contact Resistivity," *Scientific Reports,* vol. 5, p. 16704, 11/18/online 2015.

[70] J. C. Ion, *Laser Processing of Engineering Materials: Principles, Procedure and Industrial Application*. Amsterdam: Elsevier Butterworth Heinneman 2005.

[71] W. R. Eisenstadt and Y. Eo, "S-parameter-based IC interconnect transmission line characterization," *IEEE Transactions on Components, Hybrids, and Manufacturing Technology,* vol. 15, No. 4, pp. 483-490, Aug. 1992.

[72] G. E. Ponchak, J. Papapolymerou, and M. M. Tentzeris, "Excitation of coupled slotline mode in finite-ground CPW with unequal ground-plane widths," *IEEE Transactions on Microwave Theory and Techniques,* vol. 53, pp. 713-717, 2005.

[73] N. Dib, T. Weller, M. Scardelletti, and M. Imparato, "Analysis of cylindrical transmission lines with the finite-difference time-domain method," *IEEE Transactions on Microwave Theory and Techniques,* vol. 47, pp. 509-512, 1999.

[74] K. C. Gupta, R. Garg, I. Bahl, and P. Bhartia, *Microstrip Lines and Slotlines*, Second Edition ed., 1996.

[75] M. S. Islam, E. Tuncer, and D. P. Neikirk, "Accurate quasi-static model for conductor loss in coplanar waveguide," in *1993 IEEE MTT-S International Microwave Symposium Digest*, 1993, pp. 959-962 vol.2.

[76] C. Veyres and V. Fouad Hanna, "Extension of the application of conformal mapping techniques to coplanar lines with finite dimensions," *International Journal of Electronics,* vol. 48, pp. 47-56, 1980.

[77] M. Abramowitz and I. A. Stegun, *Handbook of mathematical functions with formulas, graphs, and mathematical tables*: Washington, U.S. Govt. Print. Off., 1972, c1964., 1972.

[78] A. Vera López, E. A. Rojas-Nastrucci, M. Córdoba-Erazo, T. Weller, and J. Papapolymerou, "Ka-Band Characterization and RF Design of Acrylonitrile Butadiene Styrene (ABS)," presented at the 2015 IEEE MTT-S International Microwave Symposium (IMS), 2015.

[79] T. A. Driscoll, "Schwarz–Christoffel Toolbox," 2.3 ed. http://www.math.udel.edu/~driscoll/SC/guide.pdf.

[80] G. M. Rebeiz, *RF Mems Theory, Design, and Technology*, 2003.

[81] B. J. Rubin and H. L. Bertoni, "Waves Guided by Conductive Strips Above a Periodically Perforated Ground Plane," *Microwave Theory and Techniques, IEEE Transactions on,* vol. 31, pp. 541-549, 1983.

[82] W. Heinrich, F. Schnieder, and T. Tischler, "Dispersion and radiation characteristics of conductor-backed CPW with finite ground width," in *Microwave Symposium Digest. 2000 IEEE MTT-S International*, 2000, pp. 1663-1666 vol.3.

[83] E. A. Rojas-Nastrucci, H. Tsang, P. I. Deffenbaugh, R. A. Ramirez, D. Hawatmeh, A. Ross, *et al.*, "Characterization and Modeling of K-Band Coplanar Waveguides Digitally Manufactured Using Pulsed Picosecond Laser Machining of Thick-Film Conductive Paste," *IEEE Transactions on Microwave Theory and Techniques,* 2017.

[84] B. Zhang, P. Linnér, C. Karnfelt, P. L. Tarn, U. Södervall, and H. Zirath, "Attempt of the metallic 3D printing technology for millimeter-wave antenna implementations," in *2015 Asia-Pacific Microwave Conference (APMC)*, 2015, pp. 1-3.

[85] G. L. Huang, S. G. Zhou, and T. Yuan, "Development of a Wideband and High-Efficiency Waveguide-Based Compact Antenna Radiator With Binder-Jetting Technique," *IEEE Trans. Compon. Packag. Manuf. Technol.,* vol. 7, pp. 254-260, 2017.

[86] E. A. Rojas-Nastrucci, J. Nussbaum, T. M. Weller, and N. B. Crane, "Metallic 3D printed Ka-band pyramidal horn using binder jetting," in *2016 IEEE MTT-S Latin America Microwave Conference (LAMC)*, 2016, pp. 1-3.

[87] I. Gibson, D. Rosen, and B. Stucker, *Additive manufacturing technologies : 3D printing, rapid prototyping, and direct digital manufacturing*: New York, NY : Springer, 2015. Second edition., 2015.

[88] E. Sachs, M. Cima, J. Bredt, A. Curodeau, T. Fan, and D. Brancazio, "CAD-casting: direct fabrication of ceramic shells and cores by three dimensional printing," *Manufacturing Review,* vol. 5, pp. 117-26, 1992.

[89] E. Sachs, P. Williams, D. Brancazio, M. Cima, and K. Kremmin, "Three dimensional printing: rapid tooling and prototypes directly from a CAD model," in *Proceedings of Manufacturing International '90*, ed. New York, NY, 1990, pp. 131-6.

[90] V. T. d. Crestvolant, P. M. Iglesias, and M. J. Lancaster, "Advanced Butler Matrices With Integrated Bandpass Filter Functions," *IEEE Trans. Microw. Theory Techn.,* vol. 63, pp. 3433-3444, 2015.

[91] B. Zhang and H. Zirath, "3D printed iris bandpass filters for millimetre-wave applications," *Electronics Letters,* vol. 51, pp. 1791-1793, 2015.

[92] G. Cheng, S. Xiaobang, M. J. Lancaster, and X. Jun, "A 3-D Printed Lightweight X-Band Waveguide Filter Based on Spherical Resonators," *IEEE Microw. Compon. Lett.,* vol. 25, pp. 442-444, 2015.

[93] O. A. Peverini, G. Addamo, R. Tascone, G. Virone, P. Cecchini, R. Mizzoni, *et al.*, "Enhanced Topology of E-Plane Resonators for High-Power Satellite Applications," *IEEE Trans. Microw. Theory Techn.,* vol. 63, pp. 3361-3373, 2015.

[94] C. Vicente, D. Wolk, H. L. Hartnagel, B. Gimeno, V. E. Boria, and D. Raboso, "Experimental Analysis of Passive Intermodulation at Waveguide Flange Bolted Connections," *IEEE Trans. Microw. Theory Techn.,* vol. 55 No. 5, pp. 1018-1028, May 2007.

[95] E. A. Rojas-Nastrucci, J. Nussbaum, T. M. Weller, and N. B. Crane, "Meshed Rectangular Waveguide for High Power, Low Loss and Reduced Weight Applications," in *2016 IEEE MTT-S Int. Microw. Symp.*, Phoenix, AZ, 2016.

[96] W. J. Otter and S. Lucyszyn, "Hybrid 3-D-Printing Technology for Tunable THz Applications," *Proc. IEEE,* vol. 105, pp. 756-767, 2017.

[97] M. J. Hill, J. Papapolymerou, and R. W. Ziolkowski, "High-Q micromachined resonant cavities in a K-band diplexer configuration," *IEE Proceedings - Microw. Antennas Propag.*, vol. 148 No. 5, pp. 307-312, Oct. 2001.

[98] S. Cogollos, "Filter Design for Chebyshev Filters using Rhodes' Formulas," *Technical Report University of Waterloo*, 2005.

[99] S. Khan, N. Vahabisani, and M. Daneshmand, "A Fully 3-D Printed Waveguide and Its Application as Microfluidically Controlled Waveguide Switch," *IEEE Trans. Compon. Packag. Manuf. Technol.*, vol. 7 No. 1, pp. 70-80, Jan. 2017.

[100] A. v. Bieren, E. d. Rijk, J. P. Ansermet, and A. Macor, "Monolithic metal-coated plastic components for mm-wave applications," in *2014 39th International Conference on Infrared, Millimeter, and Terahertz waves (IRMMW-THz)*, Tucson, AZ, 2014, pp. 1-2.

[101] F. J. Tischer, "Experimental Attenuation of Rectangular Waveguides at Millimeter Wavelengths," *IEEE Trans. Microw. Theory Techn.*, vol. 27, pp. 31-37, 1979.

[102] B. Huang, J. Chen, and W. Jiang, "Effects of Surface Roughness on TE Modes in Rectangular Waveguide," *Journal of Infrared, Millimeter, and Terahertz Waves*, vol. 30, pp. 717-726, 2009.

[103] S. Groiss, I. Bardi, O. Biro, K. Preis, and K. R. Richter, "Parameters of lossy cavity resonators calculated by the finite element method," *IEEE Trans. Magn.*, vol. 32, pp. 894-897, 1996.

[104] M. V. Lukic and D. S. Filipovic, "Modeling of 3-D Surface Roughness Effects With Application to μ-Coaxial Lines," *IEEE Trans. Microw. Theory Techn.*, vol. 55, pp. 518-525, 2007.

[105] S. Hall, S. G. Pytel, P. G. Huray, D. Hua, A. Moonshiram, G. A. Brist, *et al.*, "Multigigahertz Causal Transmission Line Modeling Methodology Using a 3-D Hemispherical Surface Roughness Approach," *IEEE Trans. Microw. Theory Techn.*, vol. 55, pp. 2614-2624, 2007.

[106] G. Gold and K. Helmreich, "Surface impedance concept for modeling conductor roughness," in *2015 IEEE MTT-S Int. Microw. Symp.*, 2015, pp. 1-4.

APPENDIX A: COPYRIGHT PERMISSIONS

A.1. Permissions for Chapter 2

3/11/2017 Rightslink® by Copyright Clearance Center

Copyright Clearance Center RightsLink®

Home | Create Account | Help

IEEE Requesting permission to reuse content from an IEEE publication

Title: High-Performance RF Devices and Components on Flexible Cellulose Substrate by Vertically Integrated Additive Manufacturing Technologies
Author: Chiara Mariotti
Publication: Microwave Theory and Techniques, IEEE Transactions on
Publisher: IEEE
Date: Jan. 2017
Copyright © 2017, IEEE

LOGIN
If you're a copyright.com user, you can login to RightsLink using your copyright.com credentials. Already a RightsLink user or want to learn more?

Thesis / Dissertation Reuse

The IEEE does not require individuals working on a thesis to obtain a formal reuse license, however, you may print out this statement to be used as a permission grant:

Requirements to be followed when using any portion (e.g., figure, graph, table, or textual material) of an IEEE copyrighted paper in a thesis:

1) In the case of textual material (e.g., using short quotes or referring to the work within these papers) users must give full credit to the original source (author, paper, publication) followed by the IEEE copyright line © 2011 IEEE.
2) In the case of illustrations or tabular material, we require that the copyright line © [Year of original publication] IEEE appear prominently with each reprinted figure and/or table.
3) If a substantial portion of the original paper is to be used, and if you are not the senior author, also obtain the senior author's approval.

Requirements to be followed when using an entire IEEE copyrighted paper in a thesis:

1) The following IEEE copyright/ credit notice should be placed prominently in the references: © [year of original publication] IEEE. Reprinted, with permission, from [author names, paper title, IEEE publication title, and month/year of publication]
2) Only the accepted version of an IEEE copyrighted paper can be used when posting the paper or your thesis on-line.
3) In placing the thesis on the author's university website, please display the following message in a prominent place on the website: In reference to IEEE copyrighted material which is used with permission in this thesis, the IEEE does not endorse any of [university/educational entity's name goes here]'s products or services. Internal or personal use of this material is permitted. If interested in reprinting/republishing IEEE copyrighted material for advertising or promotional purposes or for creating new collective works for resale or redistribution, please go to http://www.ieee.org/publications_standards/publications/rights/rights_link.html to learn how to obtain a License from RightsLink.

If applicable, University Microfilms and/or ProQuest Library, or the Archives of Canada may supply single copies of the dissertation.

BACK CLOSE WINDOW

Thesis / Dissertation Reuse

The IEEE does not require individuals working on a thesis to obtain a formal reuse license, however, you may print out this statement to be used as a permission grant:

Requirements to be followed when using any portion (e.g., figure, graph, table, or textual material) of an IEEE copyrighted paper in a thesis:

1) In the case of textual material (e.g., using short quotes or referring to the work within these papers) users must give full credit to the original source (author, paper, publication) followed by the IEEE copyright line © 2011 IEEE.
2) In the case of illustrations or tabular material, we require that the copyright line © [Year of original publication] IEEE appear prominently with each reprinted figure and/or table.
3) If a substantial portion of the original paper is to be used, and if you are not the senior author, also obtain the senior author's approval.

Requirements to be followed when using an entire IEEE copyrighted paper in a thesis:

1) The following IEEE copyright/ credit notice should be placed prominently in the references: © [year of original publication] IEEE. Reprinted, with permission, from [author names, paper title, IEEE publication title, and month/year of publication]
2) Only the accepted version of an IEEE copyrighted paper can be used when posting the paper or your thesis on-line.
3) In placing the thesis on the author's university website, please display the following message in a prominent place on the website: In reference to IEEE copyrighted material which is used with permission in this thesis, the IEEE does not endorse any of [university/educational entity's name goes here]'s products or services. Internal or personal use of this material is permitted. If interested in reprinting/republishing IEEE copyrighted material for advertising or promotional purposes or for creating new collective works for resale or redistribution, please go to http://www.ieee.org/publications_standards/publications/rights/rights_link.html to learn how to obtain a License from RightsLink.

If applicable, University Microfilms and/or ProQuest Library, or the Archives of Canada may supply single copies of the dissertation.

Thesis / Dissertation Reuse

The IEEE does not require individuals working on a thesis to obtain a formal reuse license, however, you may print out this statement to be used as a permission grant:

Requirements to be followed when using any portion (e.g., figure, graph, table, or textual material) of an IEEE copyrighted paper in a thesis:

1) In the case of textual material (e.g., using short quotes or referring to the work within these papers) users must give full credit to the original source (author, paper, publication) followed by the IEEE copyright line © 2011 IEEE.
2) In the case of illustrations or tabular material, we require that the copyright line © [Year of original publication] IEEE appear prominently with each reprinted figure and/or table.
3) If a substantial portion of the original paper is to be used, and if you are not the senior author, also obtain the senior author's approval.

Requirements to be followed when using an entire IEEE copyrighted paper in a thesis:

1) The following IEEE copyright/ credit notice should be placed prominently in the references: © [year of original publication] IEEE. Reprinted, with permission, from [author names, paper title, IEEE publication title, and month/year of publication]
2) Only the accepted version of an IEEE copyrighted paper can be used when posting the paper or your thesis on-line.
3) In placing the thesis on the author's university website, please display the following message in a prominent place on the website: In reference to IEEE copyrighted material which is used with permission in this thesis, the IEEE does not endorse any of [university/educational entity's name goes here]'s products or services. Internal or personal use of this material is permitted. If interested in reprinting/republishing IEEE copyrighted material for advertising or promotional purposes or for creating new collective works for resale or redistribution, please go to http://www.ieee.org/publications_standards/publications/rights/rights_link.html to learn how to obtain a License from RightsLink.

If applicable, University Microfilms and/or ProQuest Library, or the Archives of Canada may supply single copies of the dissertation.

Thesis / Dissertation Reuse

The IEEE does not require individuals working on a thesis to obtain a formal reuse license, however, you may print out this statement to be used as a permission grant:

Requirements to be followed when using any portion (e.g., figure, graph, table, or textual material) of an IEEE copyrighted paper in a thesis:

1) In the case of textual material (e.g., using short quotes or referring to the work within these papers) users must give full credit to the original source (author, paper, publication) followed by the IEEE copyright line © 2011 IEEE.
2) In the case of illustrations or tabular material, we require that the copyright line © [Year of original publication] IEEE appear prominently with each reprinted figure and/or table.
3) If a substantial portion of the original paper is to be used, and if you are not the senior author, also obtain the senior author's approval.

Requirements to be followed when using an entire IEEE copyrighted paper in a thesis:

1) The following IEEE copyright/ credit notice should be placed prominently in the references: © [year of original publication] IEEE. Reprinted, with permission, from [author names, paper title, IEEE publication title, and month/year of publication]
2) Only the accepted version of an IEEE copyrighted paper can be used when posting the paper or your thesis on-line.
3) In placing the thesis on the author's university website, please display the following message in a prominent place on the website: In reference to IEEE copyrighted material which is used with permission in this thesis, the IEEE does not endorse any of [university/educational entity's name goes here]'s products or services. Internal or personal use of this material is permitted. If interested in reprinting/republishing IEEE copyrighted material for advertising or promotional purposes or for creating new collective works for resale or redistribution, please go to http://www.ieee.org/publications_standards/publications/rights/rights_link.html to learn how to obtain a License from RightsLink.

If applicable, University Microfilms and/or ProQuest Library, or the Archives of Canada may supply single copies of the dissertation.

Thesis / Dissertation Reuse

The IEEE does not require individuals working on a thesis to obtain a formal reuse license, however, you may print out this statement to be used as a permission grant:

Requirements to be followed when using any portion (e.g., figure, graph, table, or textual material) of an IEEE copyrighted paper in a thesis:

1) In the case of textual material (e.g., using short quotes or referring to the work within these papers) users must give full credit to the original source (author, paper, publication) followed by the IEEE copyright line © 2011 IEEE.
2) In the case of illustrations or tabular material, we require that the copyright line © [Year of original publication] IEEE appear prominently with each reprinted figure and/or table.
3) If a substantial portion of the original paper is to be used, and if you are not the senior author, also obtain the senior author's approval.

Requirements to be followed when using an entire IEEE copyrighted paper in a thesis:

1) The following IEEE copyright/ credit notice should be placed prominently in the references: © [year of original publication] IEEE. Reprinted, with permission, from [author names, paper title, IEEE publication title, and month/year of publication]
2) Only the accepted version of an IEEE copyrighted paper can be used when posting the paper or your thesis on-line.
3) In placing the thesis on the author's university website, please display the following message in a prominent place on the website: In reference to IEEE copyrighted material which is used with permission in this thesis, the IEEE does not endorse any of [university/educational entity's name goes here]'s products or services. Internal or personal use of this material is permitted. If interested in reprinting/republishing IEEE copyrighted material for advertising or promotional purposes or for creating new collective works for resale or redistribution, please go to http://www.ieee.org/publications_standards/publications/rights/rights_link.html to learn how to obtain a License from RightsLink.

If applicable, University Microfilms and/or ProQuest Library, or the Archives of Canada may supply single copies of the dissertation.

Thesis / Dissertation Reuse

The IEEE does not require individuals working on a thesis to obtain a formal reuse license, however, you may print out this statement to be used as a permission grant:

Requirements to be followed when using any portion (e.g., figure, graph, table, or textual material) of an IEEE copyrighted paper in a thesis:

1) In the case of textual material (e.g., using short quotes or referring to the work within these papers) users must give full credit to the original source (author, paper, publication) followed by the IEEE copyright line © 2011 IEEE.
2) In the case of illustrations or tabular material, we require that the copyright line © [Year of original publication] IEEE appear prominently with each reprinted figure and/or table.
3) If a substantial portion of the original paper is to be used, and if you are not the senior author, also obtain the senior author's approval.

Requirements to be followed when using an entire IEEE copyrighted paper in a thesis:

1) The following IEEE copyright/ credit notice should be placed prominently in the references: © [year of original publication] IEEE. Reprinted, with permission, from [author names, paper title, IEEE publication title, and month/year of publication]
2) Only the accepted version of an IEEE copyrighted paper can be used when posting the paper or your thesis on-line.
3) In placing the thesis on the author's university website, please display the following message in a prominent place on the website: In reference to IEEE copyrighted material which is used with permission in this thesis, the IEEE does not endorse any of [university/educational entity's name goes here]'s products or services. Internal or personal use of this material is permitted. If interested in reprinting/republishing IEEE copyrighted material for advertising or promotional purposes or for creating new collective works for resale or redistribution, please go to http://www.ieee.org/publications_standards/publications/rights/rights_link.html to learn how to obtain a License from RightsLink.

If applicable, University Microfilms and/or ProQuest Library, or the Archives of Canada may supply single copies of the dissertation.

A.2. Permissions for Chapter 3

6/20/2017 Rightslink® by Copyright Clearance Center

Copyright Clearance Center RightsLink®

Home | Create Account | Help

IEEE Requesting permission to reuse content from an IEEE publication

Title: Characterization and Modeling of K-Band Coplanar Waveguides Digitally Manufactured Using Pulsed Picosecond Laser Machining of Thick-Film Conductive Paste

Author: Eduardo A. Rojas-Nastrucci

Publication: Microwave Theory and Techniques, IEEE Transactions on

Publisher: IEEE

Date: Dec 31, 1969

Copyright © 1969, IEEE

LOGIN

If you're a copyright.com user, you can login to RightsLink using your copyright.com credentials. Already a RightsLink user or want to learn more?

Thesis / Dissertation Reuse

The IEEE does not require individuals working on a thesis to obtain a formal reuse license, however, you may print out this statement to be used as a permission grant:

Requirements to be followed when using any portion (e.g., figure, graph, table, or textual material) of an IEEE copyrighted paper in a thesis:

1) In the case of textual material (e.g., using short quotes or referring to the work within these papers) users must give full credit to the original source (author, paper, publication) followed by the IEEE copyright line © 2011 IEEE.
2) In the case of illustrations or tabular material, we require that the copyright line © [Year of original publication] IEEE appear prominently with each reprinted figure and/or table.
3) If a substantial portion of the original paper is to be used, and if you are not the senior author, also obtain the senior author's approval.

Requirements to be followed when using an entire IEEE copyrighted paper in a thesis:

1) The following IEEE copyright/ credit notice should be placed prominently in the references: © [year of original publication] IEEE. Reprinted, with permission, from [author names, paper title, IEEE publication title, and month/year of publication]
2) Only the accepted version of an IEEE copyrighted paper can be used when posting the paper or your thesis on-line.
3) In placing the thesis on the author's university website, please display the following message in a prominent place on the website: In reference to IEEE copyrighted material which is used with permission in this thesis, the IEEE does not endorse any of [university/educational entity's name goes here]'s products or services. Internal or personal use of this material is permitted. If interested in reprinting/republishing IEEE copyrighted material for advertising or promotional purposes or for creating new collective works for resale or redistribution, please go to http://www.ieee.org/publications_standards/publications/rights/rights_link.html to learn how to obtain a License from RightsLink.

If applicable, University Microfilms and/or ProQuest Library, or the Archives of Canada may supply single copies of the dissertation.

BACK | CLOSE WINDOW

Copyright © 2017 Copyright Clearance Center, Inc. All Rights Reserved. Privacy statement. Terms and Conditions.
Comments? We would like to hear from you. E-mail us at customercare@copyright.com

A.3. Permissions for Chapter 4

A.4. Permissions for Chapter 5

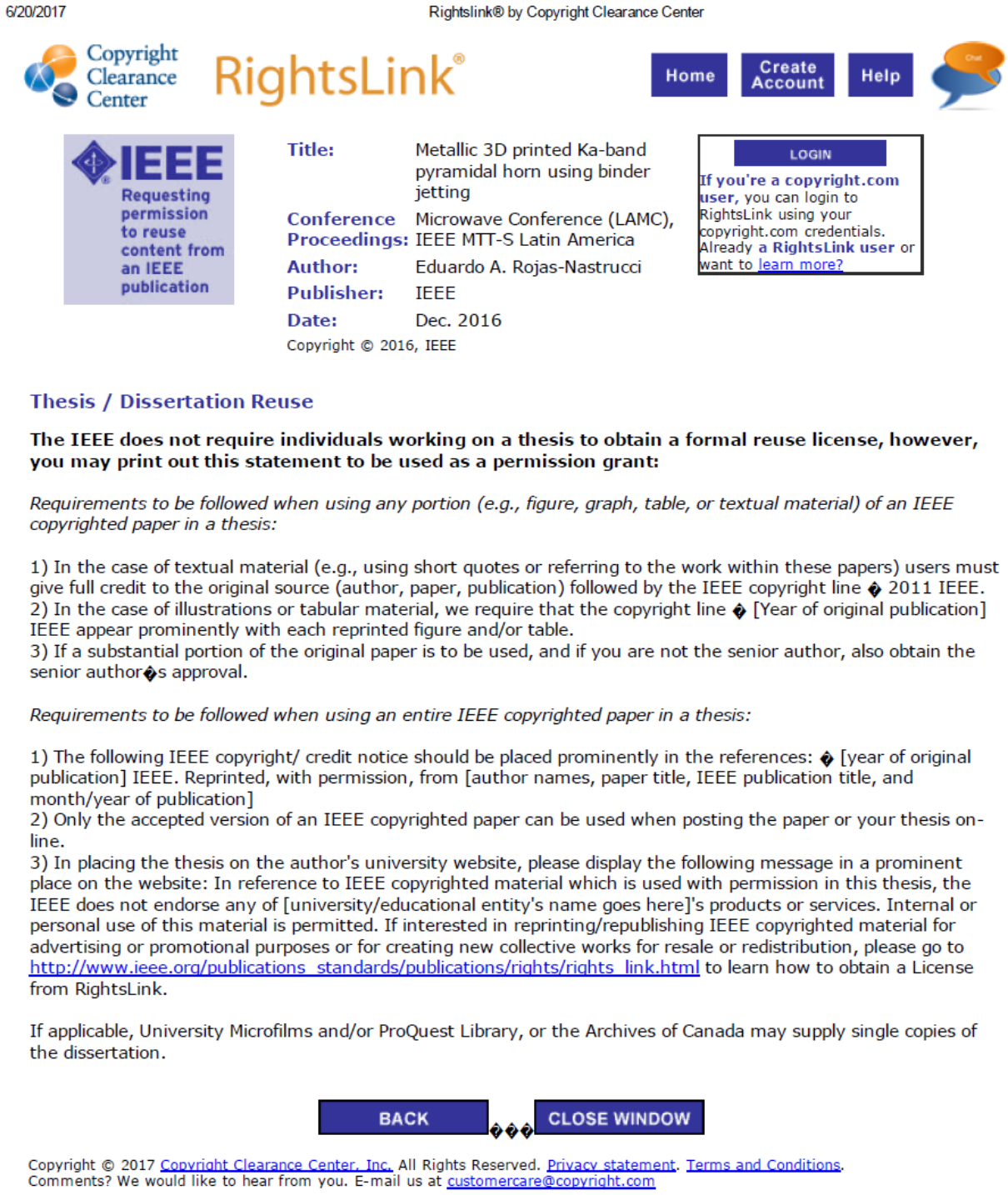

6/20/2017 Rightslink® by Copyright Clearance Center

Copyright Clearance Center RightsLink®

Home | Create Account | Help

IEEE Requesting permission to reuse content from an IEEE publication

Title: Metallic 3D printed Ka-band pyramidal horn using binder jetting

Conference Proceedings: Microwave Conference (LAMC), IEEE MTT-S Latin America

Author: Eduardo A. Rojas-Nastrucci

Publisher: IEEE

Date: Dec. 2016

Copyright © 2016, IEEE

LOGIN

If you're a copyright.com user, you can login to RightsLink using your copyright.com credentials. Already a RightsLink user or want to learn more?

Thesis / Dissertation Reuse

The IEEE does not require individuals working on a thesis to obtain a formal reuse license, however, you may print out this statement to be used as a permission grant:

Requirements to be followed when using any portion (e.g., figure, graph, table, or textual material) of an IEEE copyrighted paper in a thesis:

1) In the case of textual material (e.g., using short quotes or referring to the work within these papers) users must give full credit to the original source (author, paper, publication) followed by the IEEE copyright line © 2011 IEEE.
2) In the case of illustrations or tabular material, we require that the copyright line © [Year of original publication] IEEE appear prominently with each reprinted figure and/or table.
3) If a substantial portion of the original paper is to be used, and if you are not the senior author, also obtain the senior author's approval.

Requirements to be followed when using an entire IEEE copyrighted paper in a thesis:

1) The following IEEE copyright/ credit notice should be placed prominently in the references: © [year of original publication] IEEE. Reprinted, with permission, from [author names, paper title, IEEE publication title, and month/year of publication]
2) Only the accepted version of an IEEE copyrighted paper can be used when posting the paper or your thesis on-line.
3) In placing the thesis on the author's university website, please display the following message in a prominent place on the website: In reference to IEEE copyrighted material which is used with permission in this thesis, the IEEE does not endorse any of [university/educational entity's name goes here]'s products or services. Internal or personal use of this material is permitted. If interested in reprinting/republishing IEEE copyrighted material for advertising or promotional purposes or for creating new collective works for resale or redistribution, please go to http://www.ieee.org/publications_standards/publications/rights/rights_link.html to learn how to obtain a License from RightsLink.

If applicable, University Microfilms and/or ProQuest Library, or the Archives of Canada may supply single copies of the dissertation.

BACK CLOSE WINDOW

A.5. Permissions for Chapter 6

ABOUT THE AUTHOR

Eduardo A. Rojas-Nastrucci earned his B.S. in Electrical Engineering from the Universidad de Carabobo, Valencia, Venezuela, in 2009; and M.S.E.E. from the University of South Florida in 2014.

He worked as Assistant Professor from 2010 to 2012, for the school of Electrical Engineering, at Universidad de Carabobo, Venezuela.

He became a Ph.D. student and a member of the WAMI group at the University of South Florida in 2012. His doctoral research focused on additively manufactured Microwave Circuits and Antennas. Specifically, his work was oriented in developing new structures, materials, and techniques with the objective of creating 3D printed devices with improved performance. He has more than 20 peer-reviewed publications. He will be Assistant Professor of the Department of Electrical, Computer, Software and Systems Engineering, at Embry-Riddle Aeronautical University, Daytona Beach.